Heat Transfer in Solar Absorber Plates with Micro-Channels

By

Muyiwa Adeyinka Oyinlola

A thesis submitted to The University of Warwick
For the degree of Doctor of Philosophy in Engineering

University of Warwick, Department of Engineering
July 2015

Table of contents

Table of contents ii

List of Tables ix

List of Figures x

Acknowledgements xvi

Declaration xvii

Contributions to Knowledge xviii

Abstract xx

Nomenclature xxi

Glossary xxvi

1. Introduction 1

1.1 Background 1

1.1.1 Flat Plate Collectors 1

1.1.1.1 Geometry 2

1.1.1.2 Working Fluid 3

1.1.1.3 Minimising losses 4

1.1.1.4 Building Integration 5

1.1.2 Compact Flat Plate Collectors – The game changer 6

1.2 Aim and Objectives 8

1.3 Summary of the Thesis 8

2. Literature Review 11

2.1 Background 11

2.2 Overview 13

2.3 Scaling Effects 26

2.3.1 Geometry 26

2.3.2 Entrance/Exit Conditions 27

2.3.3 Surface Boundary 28

2.3.4 Surface Roughness 29

2.3.5 Axial Wall Conduction/Conjugate Heat Transfer 29

2.3.6 Viscous dissipation/Fluid properties 31

2.3.7 Measurement uncertainties 32

2.4 Literature Review Summary and Research Justification 32

3. Analytical Investigation 34

3.1 Background 34

3.1.1 Convention 34

3.2 Thermal analysis between channels (*y* direction) 35

3.2.1 Fin efficiency (*F*) 36

3.2.2 Collector Efficiency Factor (*F'*) 38

3.3 Thermal analysis in the flow (*x*) direction 40

3.3.1 Effects of design/operating parameters 47

3.3.1.1 Flow rate 47

3.3.1.2 Heat Transfer coefficient 48

3.3.1.3 Axial Thermal conduction 49

3.3.2 The Heat Removal Factor (F_R) 52

3.3.3 The Flow Factor (F'') 54

3.4 Summary 55

4. Experimental Setup and Data Acquisition 57

4.1 Background 57

4.2 Heated Sandwich 58

4.2.1 Description 58

4.2.2 Design considerations 64

4.2.2.1 Clamping Force to withstand pressure of liquid 64

4.2.2.2 Deflection and thermal expansion of Slabs and Plates 66

4.2.2.3 Thermal Resistance at Plate – Top slab interface 67

4.2.2.4 Heat loss 70

4.2.2.5 Temperature differences 73

4.2.3 Data Reduction 74

4.2.3.1 Mean plate temperature 75

4.2.3.2 Mean fluid temperature 75

4.2.3.3 Heat flux 75

4.2.3.4 Surface Area 76

4.2.3.5 Heat transfer coefficient 76

4.2.3.6 Pumping power per collector area 76

4.2.3.7 Friction Factor 76

4.3 Counter Flow Heat Exchanger 77
4.3.1 Description 77
4.3.2 Data Reduction 81
4.3.2.1 Mean Slab temperature 81
4.3.2.2 Mean fluid temperature 82
4.3.2.3 Log mean Temperature difference 82
4.3.2.4 Heat flux 82
4.3.2.5 Surface Area 83
4.3.2.6 Heat transfer coefficient 83
4.3.2.7 Pumping power per collector area 83
4.4 Measuring Instruments and Equipment 84
4.4.1 Thermocouples 84
4.4.1.1 Calibration 84
4.4.2 Resistance Temperature Detectors (RTDs) 86
4.4.3 Coriolis Mass Flowmeter 87
4.4.4 Differential pressure transducer 89
4.4.5 National Instrument data acquisition system 89
4.4.6 Circulating Bath 90
4.4.7 Statistical Analysis 91
4.4.8 Uncertainty 93
4.5 Summary 94

5. Numerical Analysis....95
5.1 Background....95
5.2 ANSYS CFX - Overview and Validation....96
5.2.1 Heated Sandwich Validation....98
5.2.1.1 Geometry Creation....98
5.2.1.2 Mesh....99
5.2.1.3 Domain and boundary conditions....102
5.2.1.4 Solution....106
5.2.1.5 Comparing numerical and experimental results....108
5.3 Summary....109
6. Results....110
6.1 Experimental results....110
6.1.1 Heated Sandwich....110
6.1.1.1 Aluminium Base....110
6.1.1.2 PTFE and Perspex slabs....113
6.1.2 Counter Flow heat exchanger....115
6.2 Numerical Results....118
6.2.1 Heated Sandwich Simulation....118
6.2.2 Simplified Model....121
6.3 Comparing Results....122
6.3.1 Analytical and experimental results....122

6.3.2 Simulation and experimental results 124
6.3.3 Analytical and simulated results 125
6.4 Summary 126
7. Investigating Geometrical Parameters 127
7.1 Background 127
7.2 Aspect Ratio 127
7.2.1 Theory 128
7.2.2 Thermal Performance 130
7.2.3 Hydraulic Performance 134
7.2.4 Thermo-Hydraulic Performance 137
7.3 Surface Roughness 138
7.4 Manifold 142
7.5 Summary 146
8. Investigating Scaling Effects 147
8.1 Background 147
8.2 Entrance effects 147
8.3 Viscous dissipation 151
8.4 Conjugate Heat Transfer 153
8.5 Measurement uncertainties 161
8.6 Heat Transfer Correlation 164
8.7 Summary 166

9. Conclusion and Recommendations 168

9.1 Conclusion 168

9.2 Recommendations 172

References 173

List of Tables

Table 2.1: Summary of previous studies 16

Table 4.1: Geometric parameters of the channels 62

Table 4.2: Deflection and expansion of slabs 66

Table 4.3: Thermal Resistance Details of Test rig Segments 69

Table 4.4: Statistical Analysis on thermocouple readings $\times 10^{-3}, ^{\circ}C$ 86

Table 4.5: Details of RTD signal converter module 87

Table 4.6: Details of circulating Bath 91

Table 4.7: Properties of Tyfocor 91

Table 4.8: Statistical parameters of measured instrument 92

Table 4.9: Uncertainties in measurement 94

Table 5.1: Details of the mesh used 101

Table 7.1: Geometric parameters of the channels 130

Table 7.2: Roughness parameters. 140

List of Figures

Figure 1.1: Schematic of micro-channel plate 7

Figure 3.1: Description of micro-channel plate directions 34

Figure 3.2: Micro-channel plate dimensions 35

Figure 3.3: Dimensions on a single micro-channel 36

Figure 3.4: Fin efficiency versus fin length 38

Figure 3.5: Collector efficiency factor versus heat transfer coefficient 39

Figure 3.6: (a) Elemental volume of plate 40

Figure 3.7: Temperature profile of fluid and metal plate at various flow rates 48

Figure 3.8: Temperature profile of fluid and metal plate at various heat transfer coefficients 49

Figure 3.9: Temperature profile of fluid and metal plate at various rates of axial thermal conductivity 50

Figure 3.10: Temperature profile of fluid and metal plate for the upper extreme case 50

Figure 3.11: Temperature profile of fluid and metal plate for the lower extreme case 51

Figure 3.12: Temperature difference between plate and fluid (U) for the two extreme cases 52

Figure 3.13: Heat removal factor versus mass flow rate at different U_L 53

Figure 3.14: Heat removal factor versus mass flow rate at different F' 54

Figure 3.15: Collector flow factor versus collector capacitance rate 55

Figure 4.1: Cross section of test rig through outlet port 58

Figure 4.2: Longitudinal 3D section of test rig 59

Figure 4.3: Transverse 3D section of test rig 59

Figure 4.4: (a) Inner face of Test Rig (b) Thermocouple arrangement on plate 61
Figure 4.5: Schematic showing thermocouple positions.....62
Figure 4.6 : Picture showing some of the plates 63
Figure 4.7: schematic of experimental setup.....63
Figure 4.8: Actual experimental setup 64
Figure 4.9: Isometric view of test rig showing fasteners 65
Figure 4.10: Engineering Drawing of the Test Rig.....67
Figure 4.11: Schematic of thermal resistances in the test rig.....68
Figure 4.12: (a) Distortion of grease layer (b) Procedure for measuring the sandwich 70
Figure 4.13: Heat loss at different (a) temperatures (b) input power.....72
Figure 4.14: Temperature gradient across test rig.....74
Figure 4.15: Cross section of counter flow heat exchanger 78
Figure 4.16: Inner faces of slabs 78
Figure 4.17: Thermocouple arrangement on slab 79
Figure 4.18: Schematic showing position of thermocouples 79
Figure 4.19: schematic of counter flow heat exchanger 80
Figure 4.20: The counter flow heat exchanger test rig (a) side view (b) end view....80
Figure 4.21: Micro – channel plate for counter – flow heat exchanger 81
Figure 4.22: (a) Thermocouples in bath (b) Calibration Kit 85
Figure 4.23: Thermocouple reading (a) before and (b) after calibration 86
Figure 4.24: RTD signal converter module 87
Figure 4.25: verifying accuracy of Coriolis mass flow meter.....88
Figure 4.26: Mass flowmeter readings after calibration 88

Figure 4.27: (a) Differential Pressure transducer (b) Pressure drop readings after calibration.....89
Figure 4.28: (a) SCXI-1102 Voltage input module (b) SCXI-1303 Terminal Block 90
Figure 5.1: (a) Heated sandwich geometry (b) Fluid domain 99
Figure 5.2: Temperature in flow direction at different number of nodes (a) Plate (b) Fluid 101
Figure 5.3: A magnified view of the mesh.....101
Figure 5.4: The bottom slab domain 103
Figure 5.5: The fluid domain 105
Figure 5.6: The fluid-solid interface 106
Figure 5.7: Plate temperature at the plate fluid interface 108
Figure 5.8: Comparing experimental and numerical results 109
Figure 6.1: Measured temperature distribution in metal plate 110
Figure 6.2: Heat transfer coefficient versus fluid velocity.....111
Figure 6.3: Nusselt number versus Peclet number.....111
Figure 6.4: Pressure drop versus fluid velocity.....112
Figure 6.5: Friction factor versus Reynolds number.....113
Figure 6.6: Nusselt number versus Peclet number.....113
Figure 6.7: Pressure drop versus fluid velocity.....114
Figure 6.8: Friction factor versus Reynolds number.....114
Figure 6.9: Temperature profile on slabs (a) T_{hin} = 80°C (b) T_{hin} =60°C.....116
Figure 6.10: Heat transfer coefficient versus fluid velocity (a) Tyfocor (b) Water.116
Figure 6.11: Nusselt number versus Reynolds number (a) Tyfocor (b) Water.....116
Figure 6.12: Pressure drop versus fluid velocity (a) Tyfocor (b) Water.....117
Figure 6.13: Friction factor versus Reynolds number (a) Tyfocor (b) Water.....117

Figure 6.14: Plate temperature at the plate-fluid interface.....118
Figure 6.15: Longitudinal fluid temperature profile for 3 channels.....119
Figure 6.16: Transverse fluid temperature profile at different lengths 119
Figure 6.17: Longitudinal velocity profile for 3 channels 120
Figure 6.18: Velocity contours at (a) Inlet manifold (b) Middle of channels (c) Outlet manifold 121
Figure 6.19: CFD geometry 122
Figure 6.20: Comparing analytic and experimental results (*Re*=10, T_{in}=20.5 °C) ..123
Figure 6.21: Comparing analytic and experimental results (*Re*=54, T_{in}=59 °C) 123
Figure 6.22: Comparing analytic and experimental results (Re=100, T_{in}=40 °C)...124
Figure 6.23: Comparing experimental and simulated results.....125
Figure 6.24: Comparing analytical and simulated results.....126
Figure 7.1: (a) H1 and H2 Nusselt numbers versus Aspect ratio (Shah and London, 1978, Dharaiya and Kandlikar, 2011) (b) Predicted heat transfer coefficient 130
Figure 7.2: (a) Heat transfer coefficient versus fluid velocity (b) Nusselt number versus Reynolds number 131
Figure 7.3: Comparing experimental results with theory (a) T_{in} = 5°C (b) T_{in} =20°C 133
Figure 7.4: Comparing results with correlations (a) T_{in} = 5°C (b) T_{in} = 20°C.....134
Figure 7.5: (a) Pressure drop versus fluid velocity (b) Poiseuille number versus Reynolds number 135
Figure 7.6: (a) Friction factor versus Reynolds number (b) Pumping power versus fluid velocity 137
Figure 7.7 (a) Pump power vs Heat transfer coefficient 138
Figure 7.8: Etched and Machined channel plates.....139

Figure 7.9: Surface finish on channel walls (a) Etched (b) Machined.....139

Figure 7.10: Comparing machined and etched channels 141

Figure 7.11: Pressure drop and friction factor 141

Figure 7.12: Plate temperature at the plate fluid interface.....143

Figure 7.13: Temperature profile transversely.....143

Figure 7.14: Pressure distribution in the channels 144

Figure 7.15: Velocity distribution in channels.....144

Figure 7.16: Mass flow rate in 3 channels 145

Figure 7.17: Temperature in manifold (a) inlet (b) outlet.....145

Figure 8.1: Profile of ΔT_{pf} along the plate (a)T_{in} = 5°C (b) T_{in} = 20°C.....149

Figure 8.2: Local Nusselt number along the plate (a)T_{in} = 5°C (b) T_{in} = 20°C 149

Figure 8.3: Nusselt number vs Graetz number at various fluid temperatures.....150

Figure 8.4: Transverse velocity profile at (a) entry (b) exit.....151

Figure 8.5: Horizontal velocity profile at different locations 151

Figure 8.6: Brinkman number vs Nusselt number at various fluid temperatures 153

Figure 8.7: Nusselt number vs axial conduction number.....155

Figure 8.8: Profile of ΔT_{pf} at two extreme cases 156

Figure 8.9: Nusselt number vs axial conduction number in Counter flow heat exchanger 157

Figure 8.10: Simulated fluid and plate temperature profile 158

Figure 8.11: Temperature profile at channel walls 159

Figure 8.12: Heat flux profile at channel walls.....160

Figure 8.13: Comparing analytical and simulated results.....161

Figure 8.14: Corrected Nusselt numbers versus Peclet numbers.....162

Figure 8.15: Corrected local Nusselt numbers.....163

Figure 8.16: Corrected Nusselt number vs axial conduction number 163

Figure 8.17: Friction factor versus Reynolds number 164

Figure 8.18: Heat transfer Coefficient versus Peclet number 164

Figure 8.19: Heat transfer correlation 165

Acknowledgements

I would like to express my sincere gratitude to my supervisor, Dr Stan Shire, for his continuous support, inspiration and the immense knowledge imparted throughout my PhD study - I could not have asked for anyone better. My deep appreciation also goes to Dr Roger Moss for his help, advice and critique. Also, to all members of staff of the Sustainable Thermal Energy Technology Research Group for the invaluable insight and help in designing and troubleshooting experiments; Prof Bob Critoph, Dr Zacharie Tamainot-Telto, Dr Roger Thorpe and Dr Steve Metcalf. Special thanks to Dr Layi Alatise for his advice and motivation. A big thank you to the technicians, for fabricating various test rigs.

I am greatly indebted to my family; my Parents for the huge financial sacrifice/investment made towards this degree, words cannot express my gratitude. Dr Arinola Adefila, for her immense contribution – it is very much appreciated. Other family members and friends, too numerous to mention, I am deeply grateful.

To my darling wife, Dami - Adeemama, thank you for your understanding, patience, support and inspiration. You are simply the best. Above all, I am grateful to God almighty for the grace, strength, wisdom and good health to complete this degree.

Declaration

I declare that the work in this thesis has been composed by me and no portion of the work has been submitted in support of an application for another degree or qualification of this or any other university or other institute of learning. The work has been my own except where indicated and all quotations have been distinguished by quotations marks and the sources of information have been acknowledged.

Parts of this thesis have been published by the author. These publications are listed in the next section.

Contributions to Knowledge

Peer Reviewed Journal Papers

1. Oyinlola, M.A., Shire, G.S.F. and Moss, R. W. (2015) "Thermal analysis of a solar collector absorber plate with microchannels," *Experimental Thermal and Fluid Science,* 67**,** 102-109.
2. Oyinlola, M.A., Shire, G.S.F. and Moss, R. W. (2015) "Investigating the Effects of Geometry in Solar Thermal Absorber Plates with Micro-Channels" *International journal of heat and mass transfer,* 90**,** 552-560.
3. Oyinlola, M.A., Shire, G.S.F. and Moss, R. W. (2015) "The Significance of Scaling Effects in a Solar Absorber Plate with Micro-Channels" *Applied Thermal Engineering,* 90, 499-508

Peer Reviewed conference proceedings.

1. Oyinlola, M.A. and Shire, G.S.F. (2013) Investigating Heat transfer in Absorber plates with mini channels, The 13th UK Heat Transfer Conference (UKHTC), London, UK.
2. Oyinlola, M.A., Shire, G.S.F. and Moss, R. W. (2014) Analysis of temperature distribution in absorber plates with microchannels. The 5th international conference on Heat Transfer and Fluid Flow in Microscale (HTFFM V) , Marseille, France.
3. Oyinlola , M.A., Shire, G.S.F. , Moss, R. W. and Khaliji Oskouei, M (2014) Investigating the effects of channel aspect ratio on fluid flow and heat transfer in absorber plates with minichannels The 10th International Conference on Heat Transfer, Fluid Mechanics and Thermodynamics (HEFAT2014), Orlando, USA.

Accepted conference papers and posters(unpublished)

1. Oyinlola , M.A. and Shire, G.S.F. (2013) Optimising heat transfer and fluid flow in compact solar collectors, UK Energy Research Centre (UKERC) PhD summer school, Coventry, UK [Poster presentation]
2. Oyinlola, M.A., Shire, G.S.F. and Moss, R. W. (2014) Investigating heat transfer in compact absorber plates manufactured by different techniques. The 15th International Heat Transfer Conference (IHTC15), Kyoto, Japan. [Full paper accepted for presentation (Peer Reviewed)].

Abstract

Analytical, computational and experimental studies were carried out to investigate heat transfer and fluid flow in micro-channel absorber plates for compact (thin and light-weight) solar thermal collectors. The main objective of the work was to study different design and/or operating scenarios as well as study the significance of various micro-scaling effects.

Analytical investigation showed that, under similar conditions, the proposed design yields a much higher fin efficiency, *F* and collector efficiency factor, *F'* compared with the conventional solar collector design. An analytical model combining convective heat transfer in the collector fluid with axial conduction in the metal plate was developed. The predicted plate temperature profiles from the analytical model were in close agreement with the measured profiles. The model further showed that axial thermal conduction can significantly alter the plate temperature profile.

Experiments were designed to represent real life operation of the proposed system. A CFD study, using the same design and operating parameters, produced results comparable with experiments. This numerical simulation also gave further insight into the heat transfer and fluid flow patterns in the micro-channel plate.

The effect of channel cross section geometry was studied. The Nusselt number was observed to increase as the aspect ratio approached unity. Measured friction factors were similar in trend to the predictions for rectangular channels, although the overall rise in fluid temperature resulted in slightly lower friction factors. Thermal performance reduced slightly with increase in hydraulic diameter.

The significance of various scaling effects was also investigated experimentally and numerically. Most of the typical scaling effects such as viscous dissipation and entrance effects were found to be insignificant however, conjugate heat transfer, surface boundary condition, surface finish and measurement uncertainties could be significant. The results showed a Reynolds number dependent Nusselt number which has been attributed to axial thermal conduction.

It was also observed that only three walls were transferring heat; the walls of heat transfer had a uniform peripheral temperature while the heat flux varied peripherally. The closest simplified thermal boundary condition to represent heat transfer in these channels is the H1 with three (3) walls transferring heat. Increased surface roughness (obtained by using an etching technique to create the channels) was found to have a detrimental effect on heat transfer.

The results showed that thermal improvement can be achieved by increasing the fluid velocity; however, pumping the thermal fluid above a pump power per plate area of 0.3 W/m^2 resulted in marginal improvement. In practice, optimum micro-channel geometry in plates should be sized based on fluid properties and operating conditions. The micro-channels should also have thin walls to minimise the effects of conjugate heat transfer. A Photovoltaic pump should be installed alongside the collector in order to provide pumping power required and minimise the overall fluid temperature rise. The results are beneficial for the design of micro-channel absorber plates for low heat flux operation up to $1000W/m^2$.

Nomenclature

a	Channel depth		(m)
A	Longitudinal cross sectional area		(m^2)
A_C	Collector Area		(m^2)
A_p	Plate area		(m^2)
A_L	Longitudinal cross sectional area of plate		(m^2)
b	Channel width		(m)
Br	Brinkman number	$Br = \frac{\mu v_m^{\ 2}}{q_L}$	(-)
CCR	Collector capacitance rate		(-)
C_i	constant		(-)
c_p	Specific heat capacity		(J/kg °C)
D_h	Hydraulic diameter		(m)
E	Young's modulus of elasticity		(Pa)
e	electron charge		(C)
F	Fin Efficiency		(-)
f	Friction factor		(-)
F'	Collector Efficiency Factor		(-)
F''	F_R/F'		(-)
F_f	Force exerted by fluid		(N)
F_R	Heat Removal Factor		(-)
g	Acceleration due to Earth's gravity		(m/s^2)
Gz	Graetz Number	$Gz = \frac{RePrD_h}{L}$	(-)
h_E	Enthalpy		(J/kg)

h	Heat transfer coefficient		(W/m^2 °C)
H	Overall heat transfer coefficient		(W/m^2 °C)
i	Subscript number		(-)
Ƙ	Debye-Huckel parameter		(1/m)
k	Thermal conductivity		(W/m °C)
k_b	Boltzman constant		(1/m)
k_f	Thermal conductivity of fluid		(W/m °C)
k_p	Thermal conductivity of metal		(W/m °C)
L	Length of channel		(m)
L_{hyd}	hydrodynamic entry length		(m)
L_t	Thermal entry length		(m)
L_y	Plate width		(m)
M	Axial conduction number		(-)
$\dot{m}$	Mass flow rate		(kg/s)
n	number of observations		(-)
n_0	Ionic number concentration		(1/m^3)
N_c	Number of channels in plate		(-)
Nu	Nusselt number	$Nu = \frac{hD_h}{k_f}$	(-)
p	Channel pitch		(m)
P	Width of plate		(m)
Pe	Peclet number	$Pe = RePr$	(-)
P_f	Pressure exerted by fluid		(Pa)
Po	Poiseuille number	$Po = fRe$	(-)
Pr	Prandtl number	$Pr = \frac{c_p \mu}{k_f}$	(-)

q	Heat flux density	(W/m^2)
q_c	Heat flux density from channel walls	(W/m^2)
Q	Rate of Heat Transfer	(W)
q_L	Heat flux per unit Length	(W/m)
q_t	Heat flux on top of plate	(W/m^2)
R	Thermal Resistance	(W/m °C)
Ra	Mean deviation for surface roughness	(µm)
Rp	Maximum peak height	(µm)
Rq	Root mean squared	(µm)
Rt	Maximum height of profile	(µm)
Re	Reynolds number $Re = \frac{\rho v D_h}{\mu}$	(-)
s	Surface area per unit length of channel	(m)
S	Surface area per unit length of plate	(m)
S_c	Total surface area of channels	(m^2)
S_E	Viscous work	(J)
S_M	External momentum sources	(J)
SF	Shape factor	(m)
t	Students t's parameter	(-)
T	Temperature	(°C)
T_a	Ambient Temperature	(°C)
T_b	Base Temperature	(°C)
T_f	Average fluid temperature	(°C)
T_{in}	Fluid temperature at inlet	(°C)
T_{out}	Fluid temperature at outlet	(°C)
T_p	Average plate temperature	(°C)

U	Plate-Fluid Temperature difference (Local)	(°C)
U_L	Overall Plate heat loss coefficient	(W/m^2 °C)
U_E	Internal Energy	(J)
V	Voltage drop	(V)
v_m	Mean fluid velocity	(m/s)
$\dot{W}$	Pumping power	(W/m^2)
x	Position in flow direction	(m)
x_i	Observation i	(-)
y	Position in transverse direction	(m)
z	valence of the positive/negative ions	(-)
α	Aspect ratio	(-)
α_{TE}	Coefficient of Thermal linear expansion	(1/°C)
β	volumetric thermal expansion coefficient	(1/°C)
δ	Plate thickness	(m)
Δ_{95}	95% confidence level	(-)
Δp	Pressure drop	(Pa)
ΔT_{pf}	Plate-fluid temperature difference (average)	(°C)
ε	Relative permittivity of the medium	(-)
ε_0	Permittivity of vacuum	(F/m)
$\theta(x)$	local fluid Temperature	(°C)
ν	Kinematic viscosity	(m^2/s)
ρ	Density	(kg/m^3)
σ	Standard deviation	(-)
σ^2	Variance	(-)
τ	Stress tensor	(-)

μ	Dynamic Viscosity	(Pa.s)
ώ	uncertainty	(-)
$\bar{x}$	Mean of observation	(-)

Glossary

A	Analytical
BIPV	Building Integrated Photovoltaic
C	Circular
CEL	CFX Expression Language
CFD	Computational Fluid Dynamics
CFPC	Compact Flat Plate Collector
CFPC	Compact Flat Plate Collector
cs	Cold Slab
CWH	Constant Wall Heat Flux
CWT	Constant Wall Temperature
DAQ	Data Aquisistion
EDL	Electric double layer
EFPC	Evacuated Flat Plate Solar Collector
Ex	Experimental
FPC	Flat Plate Collector
GHG	Greenhouse Gas Emissions
H1	Axially CWH and circumferentially CWT.
H2	Uniform wall heat flux, axially, and circumferentially
hf	Hot fluid
hfin	Hot fluid at inlet
hfout	Hot fluid at outlet
HTC	Heat Transfer Coefficient
L	Laminar
LM	Log mean

MEPCM	microencapsulated phase change material
N	Numerical
PV	Photovoltaic
R	Rectangle
RTD	Resistance temperature detector
Sh	hot slab
T	Turbulent
Th	Theoretical
Tra	Trapezium
Tri	Triangle
UNEP	United Nations Environment Programme

1. Introduction

1.1 Background

Energy is a vital element in any society; it improves opportunities for access to basic amenities and life's necessities such as water, food and clothing. Sadly, it is common knowledge that more than two billion of the world's population (the majority of whom live in rural areas) have no access to efficient energy supply. Technological and economic advancement have also resulted in additional drains on current energy supplies. On the other hand, environmental concerns, rising energy prices as well as government incentives are creating opportunities for renewable sources to meet the growing energy demand.

Buildings account for the bulk of the energy demand (Eicker, 2003); according to the United Nations Environment Programme (UNEP) *"Buildings use about 40% of global energy ... Yet, buildings also offer the greatest potential for achieving significant GHG emission reductions, at least cost, in developed and developing countries"* (UNEP, 2014). These highlight the need for more research and development on technologies that promote the uptake of renewable energy in buildings. Current renewable systems used in buildings include conventional photovoltaic (PV) arrays, building integrated PV (BIPV), biomass systems, evacuated tube collectors and flat plate solar collectors (FPC). This research focuses on the absorber plate of a novel FPC design which presents opportunities for building integration.

1.1.1 Flat Plate Collectors

FPCs are the most used solar collecting devices (Kalogirou, 2003). In their standard form, they consist of a metal absorber plate in an enclosure with a transparent top

and well insulated sides and bottom; a working fluid flows below or on top of the absorber. Solar radiation passes through the transparent cover to the absorber plate which absorbs and transfers the bulk of the energy to the working fluid. Standard FPCs are cost-efficient, robust and effective even with diffuse solar irradiation. FPCs are typically permanently fixed in position and require no tracking of the sun, they are usually oriented directly towards the equator, facing south in the northern hemisphere and north in the southern. In the last century, the use of these systems has evolved from primitive uses such as drying agricultural products, to more advanced uses such as producing steam and process heat. These improvements are results of the numerous studies done to improve energy gain and reduce thermal losses. A summary of the various approaches undertaken are grouped and discussed below.

1.1.1.1 Geometry

Performance enhancements have been achieved by innovatively manipulating the geometry; a detailed energy and exergy analysis was done by Farahat et al. (2009) who varied different geometrical parameters while a review of different artificial roughness elements used to enhance the heat transfer coefficient was presented by Kumar et al. (2012). Kundu (2002) did a detailed comparative study on absorber plates of different geometry and the effect of plate aspect ratio was theoretically studied by Yeh et al. (2003). Badescu (2006) and Tiris et al. (1995) are some who have investigated optimising fin geometry. Also, the effect of spacing between riser tubes has been studied by many including Bello and Sambo (1992) and Ghamari and Worth (1992).

Innovative ways of improving the heat transferred to the working fluid have been proposed; Matrawy and Farkas (1997) compared parallel and serpentine tube arrangements in conventional sheet and tube absorber plates, Rommel and Moock (1997) analytically studied absorber plates with rectangular fluid ducts and Alvarez et al. (2010) investigated absorber plates having surface contact with the working fluid. Dović and Andrassy (2012) proposed two designs of collector without tubes, parallel flat and corrugated absorber plates of chevron type, as a method of improving performance. Del Col et al. (2013) found FPCs with roll-bond absorber plates (channels for the liquid are integrated in the absorber plates) to provide higher performance compared with conventional FPCs. Shariah et al. (1999) numerically investigated the effect of thermal conductivity of the absorber plate on the overall performance.

1.1.1.2 Working Fluid

The working fluid plays an important role in the performance of FPCs. various approaches have been adopted in maximising performance with emphasis on the working fluid. Chun et al. (2009) studied the effect of the working fluid on the performance of solar energy systems in buildings while Rayegan and Tao (2011) did a comprehensive study on working fluids and proposed a procedure for the selection of working fluids for solar organic Rankine cycles (ORC). They suggested 11 fluids for use in solar ORCs based on the category of solar collectors. Similar to this, is the work of Tchanche et al. (2009), who performed a study on fluid selection for a low temperature Solar ORC. The use of nano – fluids in FPCs has been proposed by many including Yousefi et al. (2012) and Said et al. (2014).

Phase change in flows has also been used to improve performance, for example Ordaz-Flores et al. (2012) used acetone and methanol as working fluids for a two phase flat plate solar system. Comparisons with the conventional systems showed that the phase change systems exhibits slightly lower performance, however, they offer advantages of no freezing, corrosion, scaling, fouling, nor blocking of the tubing, that improve the lifetime of the system.

Similar to this is the integration of heat pipes where the absorber is the evaporator. Azad (2012) performed a comparative study on 3 different types of heat pipe solar collectors and concluded that they all performed satisfactorily. Other researchers who have studied heat pipe solar collectors include Mathioulakis and Belessiotis (2002), Tanak et al. (2005), Hussein et al. (2006) and Zhao et al. (2010).

1.1.1.3 Minimising losses

Evacuated solar collectors utilise the technology of vacuum insulation in eliminating convection losses and also have the potential of supressing gas conduction (depending on the pressure). This is the crux of evacuated tube solar collectors, and application of vacuum glazing to FPCs is increasingly becoming popular. Eaton and Blum (1975) studied the effect of evacuating FPCs, they found that at a pressure of 1–25 torr (100-3000 Pa), natural convection heat loss from the absorber was eliminated for absorber-to-cover spacing's up to 15 cm. They noted that absorbers with selective surfaces had a more reduced heat loss, however, upward losses from collector were as a result of gas conduction. Beikircher et al. (1995) studied the gas heat conduction in an evacuated flat plate collector (EFPC) for a pressure range of 10^{-3} to 10^{4} Pa. They reported that at 0.1Pa, heat conduction in air was completely suppressed. Benz and Beikircher (1999) developed an EFPC for steam production,

their study, investigated the effects of filling the envelope with other gasses on thermal losses. They noted that the reduction of the gas heat conduction with comparison to air is 32% for argon, 40% for SF6, 62% for krypton and even 77% for xenon. However, based on an economic and technical analysis, they suggested that Krypton was the best suited gas for filling. Vestlund et al. (2012) and Vestlund et al. (2009) studied the thermal and mechanical performance of filling the collector with an inert gas at normal pressures. Their results show that this could reduce overall heat losses by up to 20%.

Absorber plates with selective surfaces, commonly called selective absorbers, have been researched and developed to further improve collector performance. Selective surfaces have high absorptance for the solar spectrum range (0.2-2.5 μm) thereby maximising the absorbed solar energy. They also have a low emittance for higher spectrum range (>2.0 μm) therefore losses are minimised. Some of the studies on selective surfaces include Correa et al. (2014), Davoine et al. (2013) and Tharamani and Mayanna (2007). The use of anti-reflective coatings is another method that has been adopted to minimise losses. Some scholars who have studied this approach include Chen et al. (2011), Nielsen et al. (2014) and Barshilia et al. (2012).

Aerogels have been used as a transparent insulation to minimise heat loss. Researchers who have studied these include Dowson et al. (2012), Svendsen (1992) and Nordgaard and Beckman (1992) .

1.1.1.4 Building Integration

Developers have for long been working towards the integration of FPCs into building components. In a bid to make FPCs aesthetically acceptable with respect to

architectural designs, Tripanagnostopoulos et al. (2000) investigated FPCs with coloured (black, blue and red brown) absorbers; they recorded high thermal losses in the unglazed collectors but used flat booster reflectors to increase the radiation falling on the collectors. Juanicó (2008) presented a new design of a roof-integrated water solar collector. Matuska and Sourek (2006) compared the thermal behaviour of façade collectors with standard roof mounted collectors and concluded that façade collectors should have approximately 30% greater area than similar standard FPC in order to have comparable performance. They noted that façade collectors also affect the indoor comfort of buildings by limiting the increase in temperature to no more than 1 °C in all their investigated configurations. A low cost solar water heating system using cement concrete was studied by Chaurasia (2000); the system produced water which varied from 36 °C to 58 °C. A comprehensive review of various approaches to building integration of solar systems is presented by Hestnes (1999).

1.1.2 Compact Flat Plate Collectors – The game changer

At present, The University of Warwick, together with Loughborough University and University of Ulster are developing a compact (thin and light-weight) evacuated flat plate collector (CFPC) which combines the benefits of evacuated tube collectors with that of flat plate collectors. This collector design will be an architecturally attractive option for incorporation in buildings as an alternative to conventional flat panel or evacuated tube collectors. It will also be a landmark achievement in building integrated FPCs.

This thesis presents research focused on investigating the thermal and hydraulic performance of the absorber plates for this collector design. The proposed absorber plates will have metal sheets with micro-channels (hydraulic diameter less than 3

mm) replace the conventional FPC arrangement of tubes bonded to a metal sheet. A schematic of the micro-channel plate is shown in Figure 1.1. In addition to achieving the compact size, plates of this design offer the added advantage of enhanced convective heat transfer (based on the premise that the heat transfer coefficient is inversely proportional to the channel's hydraulic diameter), uniform temperature distribution in the transverse direction and eliminates the bond resistance between the tubes and sheet in conventional FPC design.

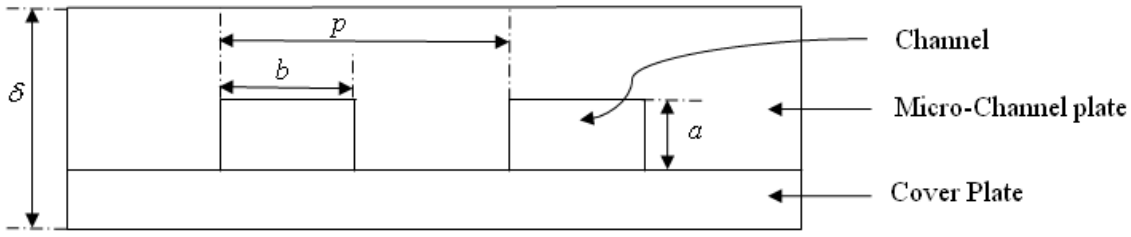

Figure 1.1: Schematic of micro-channel plate

As can be observed from the brief overview of studies focused on FPCs presented, the majority of the studies on FPC absorber plates have focused on conventional collector design with tubes bonded to a sheet. Currently, there is limited published work on the micro-channel absorber plate design. Some of the few researchers who have published work on application of micro-channels in solar collectors include Khamis Mansour (2013); who looked at flat plate rectangular channelled absorber plate, Sharma and Diaz (2011) who investigated mini-channel application in evacuated tubes and Deng et al. (2013) who studied a novel FPC with micro-channel heat pipe array.

Though heat transfer and fluid flow in micro-channels has been extensively studied over the past 3 decades, this was largely in the context of micro-electronic

components. Also, a wide dispersion in the results obtained in this field can be observed from the literature, which has been attributed to scaling effects. An additional peculiarity of this design is the thermal boundary condition that will exist on the channel walls. Therefore, a detailed study is required to understand the thermal and hydraulic behaviour of these channels.

1.2 Aim and Objectives

The aim of the current research is to investigate and optimise the performance of the absorber plates for the proposed compact flat plate collector. Accurately understanding the thermal and hydraulic behaviour has implications for the design and operation of the proposed system. The main objectives of the current research can be summarised as follows

- To compare performance of this design to predictions of conventional theory.
- To study the significance of the various scaling effects on the absorber plate performance.
- To study the effects of channel design on performance.
- To propose optimal channel design and corresponding operating condition for this system.
- To propose accurate methods of predicting collector performance.

To achieve these, analytical, experimental, and numerical analyses were carried out to investigate the heat transfer and fluid flow in plates of this design.

1.3 Summary of the Thesis

Chapter 1 presents a background to the research as well as highlights the evolution and state of art of flat plate collectors.

Chapter 2 presents a review of literature on heat transfer and fluid flow in micro-channels. It reviews previous experimental and numerical studies on heat transfer and fluid flow in micro-channels. This chapter compares and contrasts the different methods and results obtained by several researchers.

Chapter 3 is an analytical study into the thermal and hydraulic performance of the proposed plate design. Analytical models for predicting fluid and plate temperature are derived here as well as parameters typically used for characterising FPCs such as fin efficiency (F), collector efficiency factor (F'), heat removal factor (F_R) and flow factor (F''). The chapter further uses the analytical models to investigate the effects of varying design and operating parameters.

Chapter 4 describes how experiments were designed to measure the quantities needed for estimating performance. It gives a detailed explanation of the experimental facility used for all laboratory tests as well as discusses the various components of the experimental apparatus, how they were calibrated and the various design considerations. This chapter also presents details of data analysis including the dimensionless parameters.

Chapter 5 presents details of the numerical studies done using the commercial CFD package Ansys CFX. The governing equations, physics definition, geometry, mesh, boundary conditions etc. are discussed in this chapter. It also presents results on the validation of the software.

Chapter 6 presents and compares the results obtained from the analytical, experimental and numerical analyses.

Chapter 7 draws from the numerical and experimental studies to investigate the effect of the channel geometry on the thermal and hydraulic performance of the absorber plate. The design parameters varied in this study include the channels' aspect ratio, depth, width, pitch, length and surface finish of channel walls. The main operating parameter varied here is the mass flow rate. To study these effects over a range of thermo-physical properties, two (2) heat transfer fluids were used at temperatures ranging from 5°C – 60°C.

Chapter 8 uses the results from the experimental and numerical studies to investigate the micro-scaling effects on the thermal and hydraulic performance of the plates. These scaling effects include entrance effects, conjugate heat transfer and viscous dissipation.

Chapter 9 presents the main conclusions of this work. It also recommends further study into compact solar thermal collectors.

2. Literature Review

2.1 Background

Heat transfer and fluid flow in miniaturized (micro or mini) channels has been the focus of many researchers since Tuckerman and Pease (1981) pioneered the study of heat transfer in micro-channels over three decades ago. These studies were largely in the context of micro-electronic components. In recent times however, due to advantages of compact size and high heat sinking capabilities, the use of miniaturized channels as heat sinks/ heat exchangers has been extended to other fields such as automotive, chemical and food industries, environmental technology and the aviation and space industries (Schubert et al., 2001). The definition by Kandlikar and Grande (2003) which defines conventional channels as those having hydraulic diameters above 3 mm is adopted in this study.

The theory and correlations of heat transfer and fluid flow in conventional sized channels are well established; constant Nusselt number in the range 0.457 – 8.235, with the exact value depending on boundary conditions and geometry, are expected for fully developed laminar flow (Shah and London, 1978, Holman, 2010, Wibulswas, 1966). Similarly in terms of friction factor, constant Poiseuille numbers in the range 56.92 – 96.00 are expected. The results from the extensive studies on heat transfer in miniaturized channels are still inconsistent. Reviews on experimental and numerical studies of heat transfer in micro-channels published by Dixit and Ghosh (2015), Asadi et al. (2014), Rosa et al. (2009), Mokrani et al. (2009), Hetsroni et al. (2005b), and Sobhan and Garimella (2001) confirm the very large scatter in published results. These reviews unanimously attribute the dispersion to “scaling effects”, which result from neglecting phenomena that are insignificant in conventional sized channels but become significant in micro-channel flow. Examples

of these scaling effects include surface roughness (Qu et al., 2000), entrance and exit effects (Lee et al., 2005, Rahimi and Mehryar, 2012), conjugate heat transfer (Maranzana et al., 2004, Gamrat et al., 2005), thermal boundary conditions (Dharaiya and Kandlikar, 2011), viscous dissipation (Morini, 2005), electric double layer (Mala et al., 1997) and increased measurement uncertainties (Morini, 2004). It should be noted that the constant Nusselt and Poiseuille number solutions are obtained under some assumptions including

I. Steady fully developed flow.
II. The thermo-physical properties of the fluid do not vary with the temperature.
III. The fluid can be treated as a continuum medium.
IV. Incompressible flow.
V. Idealised boundary conditions (constant wall temperature or constant wall heat flux).
VI. The heating due to viscous dissipation can be neglected.
VII. Surface roughness has negligible effects in laminar flow.

Some of these assumptions are not valid at the micro scale level; this explains the need to better understand the scaling effects. The design and operating conditions of the flow channels can increase the influence of these scaling effects on overall performance. Therefore, in order to optimise design and operation, it is necessary to investigate the heat transfer and fluid flow in this design of absorber plates. This chapter reviews previous studies on heat transfer and fluid flow in miniaturised channels.

2.2 Overview

Table 2.1 presents a summary of the research conducted in this field from 1981 to 2014. The geometry of channels studied, nature of study and a summary of their results (relevant to this study) is presented. It can be observed that most of the studies conducted between 1981 and 1999 were experimental or analytical while more numerical simulations were conducted after 2000. It can also be observed that various geometries (circular, rectangular, triangular, and trapezoidal), materials (copper, aluminium, and silicon) and heat transfer fluids (water, refrigerants, air, nano-fluids) have been used. These have all been done to improve performance of micro-channel heat sinks. For example, different geometries have been used to increase the area available for heat transfer and high thermal conductivity materials have been used to improve heat sinking performance.

Table 2.1 shows that some studies have reported lower Nusselt numbers compared with predictions for conventional sized channels. These include Choi et al. (1991), Peng et al. (1994), Peng and Peterson (1996) and (Dixit and Ghosh, 2013). Most of these studies have found the low Nusselt numbers to be Reynolds number dependent unlike conventional channels where Nusselt number is constant for fully developed flow. In fact, Nusselt number correlations for micro-channels, which are Reynolds number dependent, have been proposed by Choi et al. (1991), Peng et al. (1994) and Peng and Peterson (1996). Qu et al. (2000) reported lower Nusselt numbers ($1<Nu<2$) from their experimental study, however, their Nusselt numbers were *Re*-independent. Gamrat et al. (2005) found a significant reduction in Nusselt number when the hydraulic diameter was less than 1 mm. Celata et al. (2006) observed lower Nusselt numbers than the theoretical value of 4.364 especially for flows at low Reynolds numbers. Recently, Dixit and Ghosh (2013) studied low Reynolds

numbers flow in mini-channels. They observed a linear variation of Nusselt number with the Reynolds number and found it to closely match the prediction of Choi et al. (1991). Others who have acknowledged low Nusselt numbers in their study include Nonino et al. (2009) and Rahimi and Mehryar (2012).

Some researchers have observed higher Nusselt numbers, both in the laminar and turbulent regime, compared with conventional theory. Wu and Little (1984) found their experimentally measured Nusselt number to be higher than those for conventional channels. A similar observation was made by Adams et al. (1998) who performed experiments on single phase turbulent flow. Yu et al. (1995), Celata et al. (2002) and Bucci et al. (2003) have also found the Nusselt number to exceed the theoretical predictions for conventional channels.

Lee et al. (2005) found that that their experimental results disagreed with all of the tested correlations but were well predicted by numerical simulations. This is because the boundary conditions did not fit the requirements of correlations. They recommended the use of numerical simulations with suitable boundary conditions, instead of correlations, to predict the performance of heat sinks using microchannels. Gamrat et al. (2005) observed experimental Nusselt numbers that were about 60% less than the conventional value, however, their numerical results agreed with theory. The friction coefficient was found to decrease drastically at low Reynolds number by Toh et al. (2002). This was attributed to high fluid temperature which yielded low viscosity.

Some studies have suggested that conventional predictions can accurately predict heat transfer and fluid flow in micro-channels. Weisberg et al. (1992) performed a two dimensional numerical analysis and found their results to agree (less than 20%

error) well with the experimental results of Tuckerman (1984). Harms et al. (1999) found the Nusselt number to be similar to conventional correlations. The slight deviation in Nusselt number at low Reynolds number observed in their experimental results was attributed to measurement errors. Qu and Mudawar (2002) numerically and experimentally studied laminar flow in micro-channels and found their results to agree well with theory. The experimental study by Owhaib and Palm (2004) found the heat transfer results to be accurately predicted by conventional correlations. Lee and Garimella (2006) numerically investigated heat transfer in thermally developing flow in rectangular micro-channels of different aspect ratios under H1 (axially constant wall heat flux and circumferentially constant wall temperature) thermal boundary condition. Their proposed correlation was in good agreement with conventional theory. Similarly, Dharaiya and Kandlikar (2011) numerically investigated heat transfer in rectangular micro-channels under H2 (uniform wall heat flux, axially and circumferentially) boundary condition. They proposed Nusselt number correlations which agreed with conventional theory. Toh et al. (2002) also compared the results of their 3D numerical simulation with the experimental results of Tuckerman (1984) and found good agreement. Qu and Mudawar (2002) , Lelea et al. (2004) and Tiselj et al. (2004) performed experimental and numerical studies, in each case both studies agreed with conventional theory.

From the brief overview presented above as well as the summary presented in Table 2.1, it is clear that existing correlations can not be used to adequately describe the heat transfer in miniaturised channels. The significance of the various scaling effects have to be quantified and taken into account.

Table 2.1: Summary of previous studies

Ref	Authors	Shape	D_h (μm)	Nature	Flow Type (Re)	HTF	Material	Heat flux (kW/m^2) Boundary	General Outcome	Correlation
1	Tuckerman and Pease (1981)	R	89-95	Ex	L (730)	Water	Silicon	7900 CWH	Pioneered study on heat transfer in micro-channel heat transfer	-
2	Wu and Little (1984)	R	150-160	Ex	L,T (0-12000)	Nitrogen	Glass Silicon	CWH	1.3<*Nu*<4	$Nu_T = 0.0022 Pr^{0.4} Re^{1.09}$ For turbulent flow
3	Missaggia et al. (1989)	R	160	Ex	L (1650-2350)	Water	Silicon	5000 CWH	Studied heat sink capable of dissipating 500kW/m^2	-
4	Choi et al. (1991)	C	3-81	Ex	L,T (20-25000)	Nitrogen	-	-	Higher *Nu* in turbulent regime *Nu* is *Re* dependent	$Nu_{\text{Choi}} = 0.000972 Re^{1.172} Pr^{0.333}$ For Laminar flow
5	Weisberg et al. (1992)	R	50	N	L (<100)	Water	Silicon	CWH	Agreed with (Shah and London, 1978) and (Tuckerman and Pease, 1981)	-
6	Peng et al. (1994)	R	300-650	Ex	L,T (50 -4000)	Water	Stainless steel	CWH	*Nu* lower in laminar regime but higher in turbulent	$Nu_{\text{Peng et al.}} = 0.038 Re^{0.62} Pr^{0.333}$
7	Harley et al. (1995)	R Tra	<35	Ex A	L	Nitrogen Helium Argon	Silicon	-	Lower *Po*	-
8	Peng and Peterson (1996)	R	133-367	Ex	L, T (90-9000)	Water	Stainless steel	CWH	Developed correlation for *Nu*	$Nu_{\text{p\&p}} = 0.1165 \alpha^{-0.79} Re^{0.62} Pr^{0.333} \left(\frac{D_h}{p}\right)^{0.81}$
9	Mala et al. (1997)	R	50-250	A	L (132-2259)	Water	–	CWH	EDL effects can reduce heat transfer and fluid flow	-
10	Adams et al. (1998)	C	760-1090	Ex	T	Water	Copper	3000 CWH	Higher *Nu*	$Nu_{\text{Adams}} = Nu_{\text{Gn}}(1+F)$ Where $F = CRe\left[1-(D/D_o)^2\right]$ $C = 7.6\times10^{-6}$ $f = \frac{1}{(1.82\log(Re)-1.64)^2}$

11	Tso and Mahulikar (1998)	R	-	A	L,T	Water	–	-	*Br* explains deviation	-
12	Harms et al. (1999)	R Tra	400-1900	Ex	L ,T (173-12900)	Deionized water	Silicon	-	slight *Nu* deviation at low *Re*, attributed to measurement errors	-
13	Peterson (1999)	C	0.2	N	L	Air	-		Conduction in micro-channel materials can reduce performance	-
14	Kim and Kim (1999)	R	0.1	A	L (730-836)	Water	Silicon	CWH	Identified aspect ratio and the effective thermal conductivity ratio as variables of engineering importance	-
15	Ravigururajan and Drost (1999)			Ex	L (220-1250)	R124		30-90 CWH	*h* is 2-8 times higher Pressure drop is 8-17 times higher	-
16	Mala and Li (1999)	R	50-250	A	L (132-2259)	Water	-	CWH	*Po* increases with *Re.*	-
17	Rahman (2000)	R	300-600	Ex	L,T	Water	Silicon	100 CWH	*Nu* is *Re* dependent	-
18	Fedorov and Viskanta (2000)	R	<100	N	L	Water	Silicon	1000 CWH	combined convection–conduction heat transfer produces very complex three-dimensional heat flow patterns	-
19	Qu et al. (2000)	Tra	62-169	Ex	L	Deionized Water	Silicon	CWH	Experimental *Nu* is 2- 3 times lower than CFD prediction' attributed to Surface roughness	$Nu_{Qu} = Nu_{theory}\left(\frac{\mu_{Rm}}{\mu_{Rmw}}\right)$
20	Tunc and Bayazitoglu (2001)	C	-	N	L	-	-	CWH CWT	*Nu* increases with *Pr* and reduces with *Kn*	-
21	Choi and Cho (2001)	R	6900-25000	Ex	L,T (3000-15000)	Paraffin Water	Copper Silicon	100-400 CWH	Enhancement factor ($h/\Delta P$) at low aspect ratio but begins to decrease above aspect ratio of 0.2	-
22	Tunc and Bayazitoglu (2002)	R	-	N	L,T	–	–	CWH (H2)	*Nu* increases as aspect ratio approaches unity	-

23	Qu and Mudawar (2002)	R	350	Ex N	L (139-1672)	Deionized water	Oxygen free copper	1000-2000 CWH	Agreed well with CFD prediction *Re* dependent Pressure drop attributed to temperature dependent fluid properties	-
24	Ryu et al. (2002)	R	<100	N	L (364)	Water	Silicon	1000 CWH	Channel geometry (width) crucial in dictating the performance of a micro-channel heat sink.	-
25	Zhao and Lu (2002)	R		A N	L	Water	Copper Silicon	CWH CWT	*Nu* increases as α is increased and decreases with increasing $\tilde{k}$	-
26	Gao et al. (2002)	R	200-2000	Ex	L,T (40-10000)	Demineralised water	Brass	500 CWH	*Nu* decreases more at lower depths *Nu* 60% less than conventional value Conventional laminar *Po* obtained	
27	Hegab et al. (2002)	R	100-200	Ex	T	R134a	Aluminium	CWH	*Nu* and *f* are lower	
28	Toh et al. (2002)	R	80-100	N	L (0-600)	Water	Silicon	350-7900 CWH	*f* decreases drastically at low *Re* Attributed to low viscosity due to high fluid temperature rise at low *Re*	-
29	Celata et al. (2002)	C	130	Ex	L T (100-8000)	R114	Stainless steel	CWT	*Nu* is dependent on *Re* *Nu* deviates from classical theory *f* deviates moderately at 100<*Re* <200 Attributed to increased DAQ error at low fluid velocity	-
30	Wu and Cheng (2003)	Tra	<150	Ex	L	Deionized water	Silicon	CWH	*Nu* increases almost linearly with *Re* at *Re*<100, but slowly at *Re*> 100 Geometric parameters have more significant effect than the surface roughness and hydrophilic property *Nu* and *f* increase with surface roughness	-
31	Bucci et al. (2003)	C	172-520	Ex	L,T (100-6000)	water	Stainless steel	CWT	*Nu* higher in laminar and turbulent regime. 22.25% uncertainty in *Nu*	-

32	Kroeker et al. (2004)	C	500-2500	N	L (500-1000)	Water	Copper Silicon	10-100 CWH	*Nu* agreed with previous experimental data Axial variation of *Nu* similar to classical solution for constant wall temperature. Sinks with rectangular geometry have lower thermal resistance, while sinks with circular channels dissipate more heat per unit pumping power	-
33	Tiselj et al. (2004)	Tri	160	Ex N	L (3.2-64)	Water	Silicon	36 CWH	Heat transfer agrees with conventional Navier–Stokes theory	-
34	Ng and Tan (2004)	R	72	N	L (26.58)	Water	-	CWH	$1<Nu<3$ The EDL effect will decrease the effectiveness of the micro-channel Added source term to include EDL	-
35	Kim (2004)	R	75	A N	L	–	–	-	Proposed methods for optimal channel size and fin thickness	-
36	Maranzana et al. (2004)	R	300	N	L (15.4)	Water	Silicon	30 CWH	one-dimensional model, for small flow rates, may lead to an underestimation of heat transfer coefficients	-
37	Owhaib and Palm (2004)	C	800-1700	Ex	L,T (100-17000)	R143A	Stainless Steel	CWH	*Nu* is *Re* dependent Agrees with correlation in turbulent regime. Similar *h* for 3 hydraulic diameters studied in laminar regime	-
38	Croce and D'Agaro (2004)	C	50-150	N	L (100-1700)	R114	-	CWH	Effect of roughness on heat transfer rate is smaller (within the limits experimental uncertainty) and highly dependent on shape. Significant increase in *Po* - Increase is a function of *Re*	-

39	Koo and Kleinstreuer (2004)	C R	<50	N	L (20-2000)	Water Methanol Iso-propanol		CWT CWH	*Nu* increases with the Darcy number *Nu* lower than the conventional value viscous dissipation increases fluid temperature even at low *Re* Ignoring viscous dissipation could affect accurate flow simulations and measurements	-
40	Lelea et al. (2004)	C	100-500	Ex N	L (<800)	Distilled water	Stainless steel	3.6-15 CWH	Conventional theories are applicable Entrance effects should be included	-
41	Gamrat et al. (2005)	R	200-2000	Ex N	L (200–3000)	Water	Bronze	-	*Nu* is 60% less than CFD predictions Uncertainty from position of thermocouple	-
42	Lee et al. (2005)	R	318-903	Ex N	L,T (300-3500)	Deionized water	Copper Silicon	450 CWH	Experiments agree with CFD having matching boundary conditions Entrance and boundary conditions imposed in experiment need to be carefully matched in predictions.	-
43	Croce and D'Agaro (2005)	C R Tri	50-150	N	L,T (100-1500)	R114	-	CWH	Significant increase in *Po* Roughness has small effects on heat transfer and is highly dependent on channel shape	-
44	Koo and Kleinstreuer (2005)	C R	<50	N	L (20-2000)	water, methanol Iso-Propanol	-	CWT CWH	*Nu* can be lower or higher than theory depending on type of surface roughness	-
45	Reynaud et al. (2005)	R	300-1120	Ex	L,T (600-72000)	Filtered tap water	Bronze	1000 CWH	*Nu* slightly *Re* dependent *Nu* slightly higher than theory Similar Laminar *Nu* for 3 different d_h. *Nu* measurements at low flowrates are altered by free convection effects. *Po* close to theory for the two thickest channels in laminar regime	-

46	Celata et al. (2006)	C	50 -528	Ex	L (50-2775)	Demineralised water	Chromium molybdenum or chromium–gold coated Glass	1370-2560 CWH	Lower *Nu* which was attributed to a heat loss term that has the same effects as axial wall conduction. *Nu* decrease is more marked for decreasing *Re*	-
47	Shen et al. (2006)	R	444	Ex	L (162–1257)	Deionized water	cooper	180-590 CWH	*Nu* deviate from theory attributed to surface roughness *Nu* is *Pe* dependent *f* deviates from theory	$Nu = 0.5046Pe^{0.2221}$
48	Muwanga and Hassan (2006)	C	1000	Ex	L (500-5000)	Deionized water	Stainless	CWH	Agrees with conventional theory Used Liquid crystal thermography for temperature measurements	-
49	Lee and Garimella (2006)	R	200-364	N	L (100-1500)	Water	-	500 CWH	H1 thermal boundary condition best represents micro-channel heat sinks	-
50	Li and Peterson (2007)	R	110	N	L	Water	Silicon	10000 CWH	Geometry significant in improving heat transfer performance	-
51	Chen (2007)	R	-	AN	L	–	–	CWH	*Nu* increases with aspect ratio. *Nu* decreases with increasing the effective thermal conductivity ratio.	-
52	Tsai and Chein (2007)	R	90	A	L	Cu–water CNT–water	Silicon	-	*Nu* is improved with nanoparticle compared with pure fluid. Improvement proportional to the particle volume fraction The degree of improvement also depends on α	-
53	Kou et al. (2008)	R	<1000	N	L	Water	Silicon	1000 CWH	Optimum channel size depends on flow power	-
54	Husain and Kim (2008)	R	80-100	N	L	Water	Silicon	340-7900 CWH	Micro-channel size and fin width have significant effect on the thermal performance of micro-channel heat sink	-

55	Naphon and Khonseur (2009)	R	300-400	Ex	L (200-1000)	Air	Acrylic	1.8-5.4 CWH	*Nu* is dependent on *Re* Micro-channel geometry has significant effect on the enhancement heat transfer and pressure drop.	-
56	Xie et al. (2009)	R	800-1400	N	L (100-2200)	Water	Copper	2560 CWH	Agrees well with correlations. A narrow and deep channel is better than that of a wide and shallow channel, in spite of the high pressure drop penalty.	-
57	Wang et al. (2009)	Tra	155	Ex N	L (33-565)	Water	Silicon Pyrex glass	300 CWH	*Nu* agrees well with theory	-
58	Mokrani et al. (2009)	R	100-1000	Ex	L,T (100-5000)	Tap water	Stainless	CWH	*Nu* agrees well with theory *f* agrees well with theory	-
59	Nonino et al. (2009)	C	-	N	L (50-200)	Water	Silicon Stainless steel	CWH	Deviations occur if conjugate heat transfer phenomenon are neglected	-
60	Koşar (2010)	R	200	N	L	Water	Cu, Al, Si Steel, glass Quartz, polyimide	CWH	Proposed correlation	$Nu_{Koşar} = 4.516 - 0.2551\frac{Bi^{0.04}}{k^{*0.24}}$
61	Cho et al. (2010)	R Tra	300	Ex	–	R-123	Silicon	CWH (uniform and non-uniform)	Straight micro-channels show less sensitivity of the temperature distributions to the variation of the header shape	-
62	McHale and Garimella (2010)	Tra	<100	N	L	–	Silicon	CWH	New correlations for local and average Nusselt numbers are given	$Nu_{McHale} = 3.265 + 5.075e^{-e^{\left[-0.9041\left(\ln(\alpha)-1.3496\right)\right]}}$
63	Betz and Attinger (2010)	R	50	Ex	L	Water	Polycarbonate–Al	CWH	Segmented flow can increase laminar *Nu* by more than 100%	-
64	Dogruoz et al. (2010)	R C	60-240	N	-	Water	Copper Aluminium	1000 CWH	*Nu* more dependent on geometrical features than the flow rate values.	-

65	Gunnasegaran et al. (2010)	R Tra Tri	150-400	N	L (100-1000)	Water	Aluminium	0.1-1 CWH	*Nu* increases with *Re* *Po* increases with *Re* heat transfer increased from triangular to trapezoidal and then to rectangular channels	-
66	Chiu et al. (2011)	R	200-1000	Ex N	L	Water	–	150 CWH	*Nu* decreases with increasing α *Nu* monotonically decreases along channel for high aspect ratio *Nu* is affected by entrance effects in channels with low aspect ratio.	-
67	Moharana et al. (2011)	R	900	Ex N	L (150-2500)	Deionized water	Copper	CWH	Lower *Nu* due to experimental uncertainties especially at low *Re*. *Nu* varies axially due to axial conduction - knowledge of the axial conduction number is vital for achieving correct data reduction. Most parallel channels connected to a common inlet header will have fully or partially developing flows.	-
68	Mohammed et al. (2011)	R	400	N	L (100-1000)	Water	Aluminium	0.1 CWH	wavy micro-channels can be proposed as next generation cooling devices for removing high heat flux instead of using conventional straight micro-channels	-
69	Escher et al. (2011)	R	80-200	Ex A	L (100-1800)	SiO2–water	Silicon	0.1 CWH	Agrees with standard correlations	-
70	Dharaiya and Kandlikar (2011)	R	-	N	L (100)	-	-	CWH H2	*Nu* for four wall H2 condition did not vary much with an increase in aspect ratio Other correlations proposed for different number of walls heated	$Nu_{H2D\&k} = 0.3816\alpha + 2.886$ Correlation is for 4 walls heated.

71	Lelea (2011)	R	50	N	L	Alumina –water	Copper	350 CWH	Heat transfer enhancement rises along the micro-channels. Heat transfer augmentation increases as the particle's concentration increases.	-
72	Xia et al. (2011)	R	<200	N	L (100-1000)	Water	Silicon	1000 CWH	Heat transfer enhancement mechanism of the micro-channel with triangular re-entrant cavities can be attributed to not only the vortices formed inside by the reentrant cavity but also to interrupted and redeveloped periodically thermal boundary layer along the constant cross-section surface	-
73	Saenen and Baelmans (2012)	R	-	N	L	Air	Silicon	CWH	Numerical solution agreed with experimental data	-
74	Ijam et al. (2012)	R	900	A	L	Al2O3–water TiO2–water	Copper	3500-5570 CWH	Nanofluid improved HTC	-
75	Rahimi and Mehryar (2012)	C	Do/Di= 1.5-3.5	N	L (100-500)	Pr=2-34	K_s/k_f=33-920	CWH	*Nu* is decreased at the entrance and ending regions due to axial heat conduction in the duct wall	-
76	Sharma et al. (2013)	R	150	N A	L (1200)	Hot water	Copper	CWH	moderately increased pumping power, while increasing viscous dissipation can reduce the entropy generation due to heat transfer and thus minimize the overall entropy generation	-
77	Zhuan and Wang (2013)	R	230	Ex	L	R134a Deionized water	Polyetheretherketone	2-22 CWH	*h* is independent of heat flux. Heat transfer deteriorated when intermittent dry out was encountered. *h* declined with the increase in vapour quality and moderately increased with mass flux	-

78	Chai et al. (2013)	R	133	N	L (200-700)	Water	Silicon	1.22 CWH	6< *Nu* <12	-
79	Dixit and Ghosh (2013)	R	500-1500	Ex	L (17-450)	Water	Aluminium Stainless Brass Copper	8.5-11.7 CWH	*Nu* is *Re* dependent Nearly identical *Nu* from heat sinks made of different materials *f* lower than conventional theory	-
80	Naphon and Nakharintr (2013)	R	1000-2000	Ex	L (60-200)	Nanofluid (TiO_2 – H_2O)	Copper	14-17 CWH	0.5<*Nu*<1.5 *Nu* of nanofluids are greater than of their base fluid (de-ionized water).	-
81	Ho and Chen (2013)	R	1200	Ex	L (133-1515)	Nano-fluid	Copper	CWH	Nano-fluid yields significant enhancements in the average heat transfer coefficients.	-
82	Ho et al. (2014)	R	1200	Ex	L (133-1515)	Nano fluid alumina MEPCM	copper	CWH	Proposed correlation	$Nu_{ho}=1.868\left(\frac{Pe}{L/D_h}\right)^{0.37}\left(1+1.72\omega_{np}-7.48\omega_{np}^2\right)$ ωnp=mass fraction
83	Balaj et al. (2014)	R	-	N		argon	-	250-750 CWH	*Nu* is a weak function of *Br* *Nu* increases as wall heat flux increases at constant *Kn* number *Nu* however decreases gradually as Knudsen number increases in the slip flow range and beyond	-
84	Dirker et al. (2014)	R	50-105	Ex	L (300-2800)	Water	copper	5-40 CWH	*Nu* agrees well with conventional macro-channel thermal entry correlations Swirl inlet type altered behaviour of *Nu* and *f* *f* decreases with an increase in heat input due to a reduction in the fluid viscosity at the wall	-

*R – Rectangle, C – Circular, Tra – Trapezium, Tri-Triangle, Ex – Experimental, N – Numerical, A – Analytical, L – laminar, T – Turbulent

2.3 Scaling Effects

Some of the scaling effects (relevant to this study) that have been cited for the dispersion of results are presented below.

2.3.1 Geometry

The Nusselt and Poiseuille numbers are highly dependent on the cross-sectional geometry. Experimental results must therefore be compared with correlations for similar cross sections. Dogruoz et al. (2010) suggested that the wall heat transfer coefficient shows more dependence upon micro-channel geometry than upon flow rate. similarly, Naphon and Khonseur (2009) concluded that the micro-channel geometry configuration has significant effect on the enhancement of heat transfer and pressure drop. Peng and Peterson (1996) found the heat transfer in laminar flow through rectangular channels to depend on the aspect ratio and the ratio of the hydraulic diameter to the pitch of the micro-channels. Rosa et al. (2009) noted that experiments with single channels are more accurate and in good agreement with predictions from published correlations. This is because experiments with multi (parallel) channels are subject to flow mal-distribution and varying conditions in each channel.

As can be observed from Table 2.1, the conditions for experimental and numerical studies have varied greatly, for example, channel profile, number of channels, channel spacing, inlet and outlet ports/manifolds. Therefore the deviations observed in the literature can be partly attributed to varying geometrical conditions.

2.3.2 Entrance/Exit Conditions

The heat transfer coefficient of fluid flow in internal ducts is higher in the entry region where the temperature and/or velocity profile is still developing. Therefore, higher local Nusselt numbers are observed in this entry region. This can affect the average Nusselt number significantly if the entry region constitutes a significant portion of the flow. Lee et al. (2005) numerically simulated micro-channels with inlet and exit manifolds and observed that micro-channel flow is generally thermally developing with considerable entrance effects. Guo and Li (2003) noted that entrance effects are likely to contribute to the observed deviations.

The entrance effects are likely to contribute to higher and *Re* dependent Nusselt numbers. Dogruoz et al. (2010) suggested disrupting the boundary layer to increase thermal performance. Bucci et al. (2003) observed Nusselt number increases with Reynolds number as in thermally developing flows, achieving up to 55% increase in the value predicted by conventional theory. Rosa et al. (2009) noted that when entrance effects are significant, average Nusselt number increases with the Reynolds number. Celata et al. (2006) took precautions to ensure other scaling effects were negligible and observed experimental Nusselt number to agree reasonably with correlations for thermally developing flows. Muwanga and Hassan (2006) measured local heat transfer coefficients using liquid crystal thermography and found that the Nusselt number was in good agreement with the analytical solution for thermally developing flows in the laminar regime.

The manifolds can play a significant role in the entry length. Rosa et al. (2009) noted that because micro-channels are usually characterised by short lengths, entrance header effects can be significant and need to be investigated. Others who have

highlighted the importance of the manifolds on the flow include Bajura (1971), Kim et al. (1995) and Tompkins et al. (2002)

2.3.3 Surface Boundary

A classification of different types of surface boundary conditions in internal flow is outlined in Shah and London (1978). Most established Nusselt number correlations are for idealised boundary conditions of constant wall temperature (CWT) and constant wall heat flux (CWH). In micro-channels, however, it is difficult to achieve idealised boundaries because wall conduction has a strong influence on the temperature profiles particularly at low Reynolds number (Rosa et al., 2009, Rahimi and Mehryar, 2012). Furthermore, the heat to be dissipated may be incident on the top face of the plate; this will result in a peripheral variation of the heat flux density. Some scholars who investigated micro-channels subjected to a constant wall heat flux have assumed either a H1 (axially constant wall heat flux and circumferentially constant wall temperature) or H2 (uniform wall heat flux, axially, and circumferentially). For example Tunc and Bayazitoglu (2002) used the H2 boundary condition while Lee and Garimella (2006) suggested that H1 thermal boundary condition represents micro-channel heat sinks best. Numerical H1 Nusselt numbers for rectangular micro-channels of varying aspect ratios is presented in Lee and Garimella (2006) while those for H2, including varying number of adiabatic walls, is presented in Dharaiya and Kandlikar (2011). Therefore, another possible contributor to the scatter in results can be attributed to the varying boundary conditions (Lee et al., 2005).

2.3.4 Surface Roughness

Achieving completely smooth surfaces in micro-channels is practically impossible; the surface finish can therefore affect the heat transfer and fluid flow. In conventional sized channels, the effects of surface roughness can be neglected if internal wall roughness is less than 5% of the channel diameter (Moody, 1944). Several researchers have attributed discrepancy in their results to surface roughness for example, Qu et al. (2000), Mala and Li (1999) & Shen et al. (2006) .

The effect of surface roughness in micro-channels has been studied by many, for example, Koo and Kleinstreuer (2005), Croce and D'Agaro (2004), Croce and D'Agaro (2005) and Wu and Cheng (2003). From these studies, it can be observed that surface roughness is responsible for an increase in Poiseuille number while it can increase or decrease the Nusselt number. Koo and Kleinstreuer (2005) and Rosa et al. (2009) concluded that the surface roughness has a weak effect on heat transfer in micro-channels, often within experimental uncertainties, therefore corrections to account for surface roughness on Nusselt number need not be made.

2.3.5 Axial Wall Conduction/Conjugate Heat Transfer

In a convective heat transfer problem, the heat transfer within the solid surface is often negligible. When this becomes significant, resulting in thermal conduction in the solid surface, the process is referred to as conjugate heat transfer. The effect of conjugate heat transfer in conventional sized channels is often neglected because the wall thickness is very small compared with the hydraulic diameter. However, the wall thickness can be significant in micro-channel applications, resulting in a conjugate heat transfer problem. Gao et al. (2002), Guo and Li (2003), Maranzana et

al. (2004), Gamrat et al. (2005), Nonino et al. (2009), Mohammed et al. (2011) and Rahimi and Mehryar (2012) are among many who have observed conjugate heat transfer to significantly influence heat transfer; it reduces the Nusselt number, particularly at low Reynolds numbers.

Conjugate heat transfer can also modify the surface boundary condition. Kroeker et al. (2004) and Maranzana et al. (2004) noted that axial conduction can give rise to a non-uniform axial wall heat flux density, with a larger heat transfer to the fluid at the entrance. This results in a high temperature gradient in the entrance region in both the fluid and solid regions, especially at low Reynolds numbers. Rahimi and Mehryar (2012) showed that axial wall conduction could also affect the outlet region. Rosa et al. (2009) observed that when using parallel channels as in commercial micro-heat sinks, significant 3D effects can arise which may only be predicted by appropriate numerical 3D simulations.

Conjugate heat transfer can also be responsible for the *Re* dependent Nusselt numbers observed in many studies. This is because the axial thermal conduction in the channel walls decays as the Reynolds number increases. Morini (2006) noted that the dependence of the mean Nusselt number on the Reynolds number in the laminar regime may be partly explained by conjugate heat transfer effects at low Reynolds numbers combined with viscous and entrance effects at higher Reynolds numbers.

Several studies such as Fedorov and Viskanta (2000) and Nonino et al. (2009) have focused on investigating the effect of various parameters on conjugate heat transfer. These parameters include wall thickness, wall thermal conductivity, entrance length and heat loss through the end section. It can be concluded that conjugate heat transfer is more relevant for short ducts, thick walls and/or at low Reynolds numbers.

The study of conjugate heat transfer is not limited to micro-channels, it has also been studied in conventional channels by Faghri and Sparrow (1980), Barozzi and Pagliarini (1984) and Barozzi and Pagliarini (1985).

2.3.6 Viscous dissipation/Fluid properties

In macroscopic flows through channels, internal generation of heat is usually neglected, however, at very small hydraulic diameters; viscous forces can generate significant internal heat, which can in turn influence the heat transfer (Rosa et al., 2009). Also, thermo-physical properties of the fluid can vary significantly between the inlet and the outlet due to temperature change in the fluid. This can influence the Nusselt and Poiseuille numbers remarkably. Koo and Kleinstreuer (2004) observed that viscous dissipation increased the fluid temperature in micro-channels, even at low Reynolds number. Other examples of those who attributed deviations to viscous dissipation/ variation of fluid properties include Tunc and Bayazitoglu (2001), Toh et al. (2002), Morini (2006), Herwig and Mahulikar (2006), Jeong and Jeong (2006) and Chen (2006). The effect of viscous heating on the Nusselt number can be influenced by the type of boundary condition. Viscous dissipation increases the Nusselt number under a constant wall temperature boundary condition and reduces it under a constant wall heat flux boundary condition. This is because viscous dissipation reduces the average temperature difference between wall and fluid in a constant wall temperature boundary and increases it in a constant wall heat flux. Rosa et al. (2009) concluded that viscous heating can markedly influence heat transfer in micro-channels and should always to be checked.

2.3.7 Measurement uncertainties

The reduced length scale in micro-channel studies poses challenges in taking accurate measurements. Furthermore, the introduction of measuring instruments within the flow can have significant effects on the results. Palm (2001), Hetsroni et al. (2005b) and Rosa et al. (2009), who reviewed studies on heat transfer in micro-channels, suggested that measurement uncertainties can have a strong influence on experimental results. Gamrat et al. (2005) observed that the position of the thermocouples away from the liquid/solid interface can yield as much as 40% uncertainty in the estimated Nusselt number. Bucci et al. (2003) observed 22.25% uncertainty in their Nusselt number. Others who have highlighted the significance of measurement uncertainties include Harms et al. (1999), Celata (2004), Morini (2004), Reynaud et al. (2005) and Celata et al. (2006). Obot (2002) reviewed many published experimental results for micro-channels and concluded that an uncertainty of up to 25% could be very well expected and should be considered satisfactory. Some of these uncertainties arise from channel diameter variation axially, difficulty in accurately measuring fluid and channel wall temperatures and assuming similar conditions in all channels. Therefore experimental results should account for the various measurement errors.

2.4 Literature Review Summary and Research Justification

From the literature review presented, it can be observed that despite extensive studies on miniaturised channels, there are still considerable discrepancies between results. This inconsistency has generally been attributed to scaling effects. In fact, quite recently, Dixit and Ghosh (2015) who presented the state of the art on heat transfer in micro and mini channels, noted that standard design and analysis

methodology for miniaturised channels, whether using theoretical or experimental techniques, are not yet available.

The geometry (aspect ratio) of the channels influences the thermal (depending on the boundary condition) and hydraulic performance. The flow regime influences the thermal performance. The type of thermal boundary influences thermal performance. Surface roughness can influence thermal and hydraulic performance. Conjugate heat transfer reduces thermal performance. Therefore, an experimental investigation to quantify the effects of these scaling effects is necessary

These scaling effects can be influenced by the design and operation, therefore the performance of the micro-channel heat sink has to be tested for the particular application. The extensive study of miniaturised channels has been largely in the context of cooling electronic components. Very few scholars have reported using micro-channels in solar systems, these include Khamis Mansour (2013); who looked at a flat plate rectangular channelled absorber plate, Sharma and Diaz (2011); who investigated its application in an evacuated tube collector and Deng et al. (2013) who studied a novel FPC with micro-channel heat pipe array. The peculiarities of the application of micro-channel heat transfer in solar collectors include the low Reynolds number as well as the low heat flux density. Most of the previous work done have been conducted for higher flow rates (typically Re>100) and higher heat fluxes (typically q>10,000 W/m^2). However, this study focuses on flows with Re<100 and q<1000 W/m^2. This thesis aims to fill the gap in knowledge of the heat transfer and fluid flow occurring in the proposed design of micro-channel plates.

3. Analytical Investigation

3.1 Background

This chapter presents an analytical study into the temperature distribution in the proposed absorber plate. This analysis is important for the optimization of design parameters, especially to minimize temperature gradient in the transverse and longitudinal directions. Minimizing temperature gradient on the absorber plate will improve collector's performance; collector's performance will be maximized if the whole absorber plate surface is at the same temperature as the inlet fluid (Duffie and Beckman, 2006). An analysis similar to that presented by Duffie and Beckman (2006), for conventional sheet and tube design, is adopted for the micro-channel absorber plate.

3.1.1 Convention

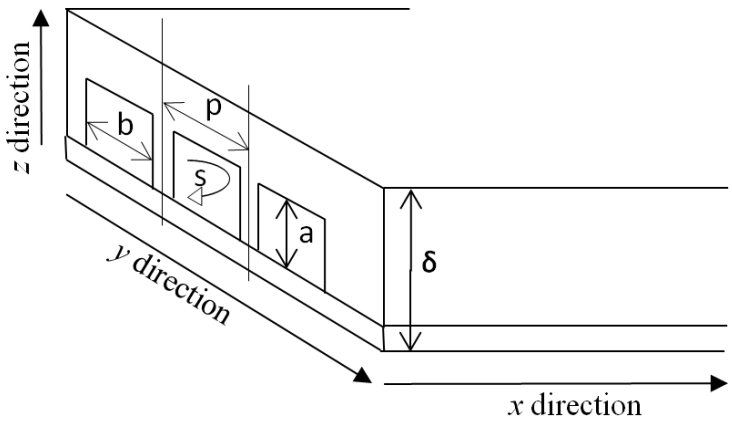

Figure 3.1: Description of micro-channel plate directions

Figure 3.1 describes the various directions in the microchannel plate.

1. The fluid flows in the x direction, along the length (longitude) of the plate from inlet to outlet.
2. The channels are arranged in parallel along the width (transverse/y direction) of the plate from left to right.

Figure 3.2 shows the dimensions of the micro-channel plate; channels have a depth *a*, width *b*, separated by a pitch distance *p*. The micro-channel plate has fluid passing along rectangular passages, the fourth side of the passage is formed by a cover plate that is clamped in place hard against the inter-passage ribs, and the plate has a total thickness δ.

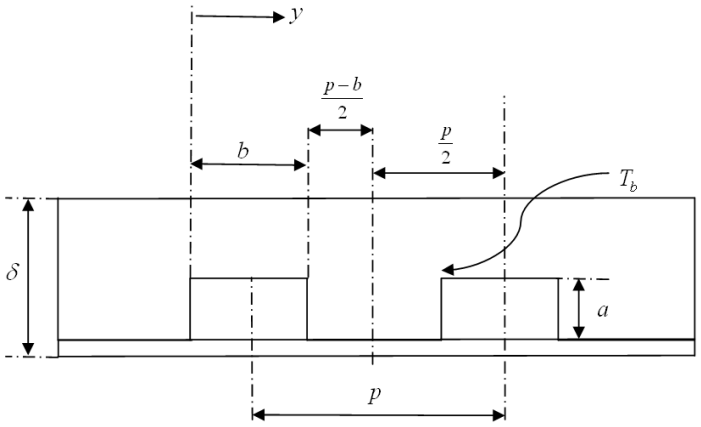

Figure 3.2: Micro-channel plate dimensions

3.2 Thermal analysis between channels (*y* direction)

In order to obtain the significance of the plate design, the following assumptions are made.

1. The heat transfer in the flow direction is temporarily neglected.
2. Since the plate is thin and will be made of a material with good thermal conductivity, the temperature gradient through the plate (*z* direction) can be neglected.
3. Convection heat transfer occurs on all four sides of the channels

A fraction of the solar irradiance on the collector will be reflected away and the rest will be absorbed by the plate; the magnitude of this will depend on several factors

such as the glazing and surface of the collector. However, since this study is focused on the absorber plate, only the solar irradiance absorbed by the plate q_t, will be considered. A part of this energy absorbed by the plate is further lost to the environment, the magnitude of this loss, which will vary based on several factors, can be defined in terms of an overall plate heat loss coefficient, U_L .

This implies that the loss from the absorber plate can be defined as

$$q_L = U_L \left(T_p - T_a \right) \tag{3.1}$$

In conventional sheet and tube solar collectors, a thermal analysis is done on the fin element. However, since this design incorporates micro-channels, the fin efficiency will yield values in excess of 99.9%. A more appropriate method of obtaining the fin efficiency will be to compare the thermal conduction resistance in the metal plate to the overall thermal resistance.

3.2.1 Fin efficiency (*F*)

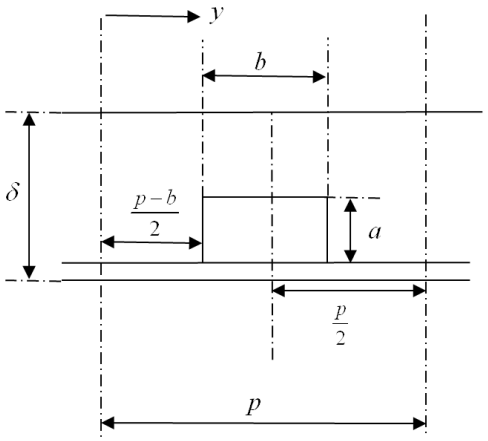

Figure 3.3: Dimensions on a single micro-channel

The thermal conduction resistance of the geometry shown in Figure 3.3, can be obtained using the conduction shape factor *SF*,

$$R_{cond} = \frac{1}{kSF} = \tag{3.2}$$

The conduction shape factor for this geometry is given as (Çengel et al., 2011)

$$SF = \frac{2\pi L}{0.93\ln\left(0.948\,{}^{p}\!/_{b}\right)} \text{ (for } p/b>1.41) \tag{3.3}$$

$$SF = \frac{2\pi L}{0.785\ln\left({}^{p}\!/_{b}\right)} \text{ (for } p/b<1.41) \tag{3.4}$$

There will be a channel wall to fluid resistance when the useful energy gain, is being transferred to the thermal working fluid. It should be noted that in conventional arrangements, an additional resistance will result from the bond between tubes and sheet, hence this absorber plate design offers lesser resistance in the transfer of useful energy to the fluid. The convection resistance in a single channel can be shown to be

$$R_{conv} = \frac{1}{sh} = \frac{1}{2h(a+b)} \tag{3.5}$$

Therefore, the fin efficiency will be

$$F = \frac{R_{conv}}{R_{cond} + R_{conv}} \tag{3.6}$$

Figure 3.4 shows variation of the fin efficiency with fin length at different values of plate thermal conductivity. The figure shows that the thermal conduction resistance decays as the pitch distance reduces and/or thermal conductivity of the material increases. Therefore, heat loss from the absorber plate can be reduced by designing plates with channels closely spaced out.

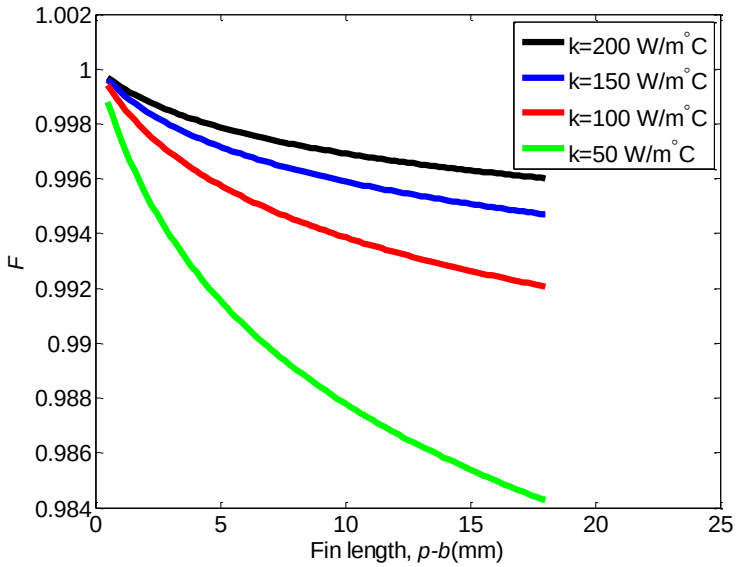

Figure 3.4: Fin efficiency versus fin length

3.2.2 Collector Efficiency Factor (*F'*)

The collector efficiency factor $F^{'}$ is defined as the ratio of the actual useful energy gain to the useful gain that would result if the collector absorbing surface was at the local fluid temperature (Duffie and Beckman, 2006).

$$F' = \frac{q_u^{'}}{p\left[q_t - U_L\left(T_f - T_a\right)\right]} \tag{3.7}$$

The collector efficiency factor F' can also be defined as the ratio of the heat transfer resistance from the absorber plate to the ambient air to the heat transfer resistance from the fluid to the ambient air (Duffie and Beckman, 2006).

$$F' = \frac{1/pU_L}{\left[\frac{1}{SFk} + \frac{1}{2h(a+b)}\right]} \tag{3.8}$$

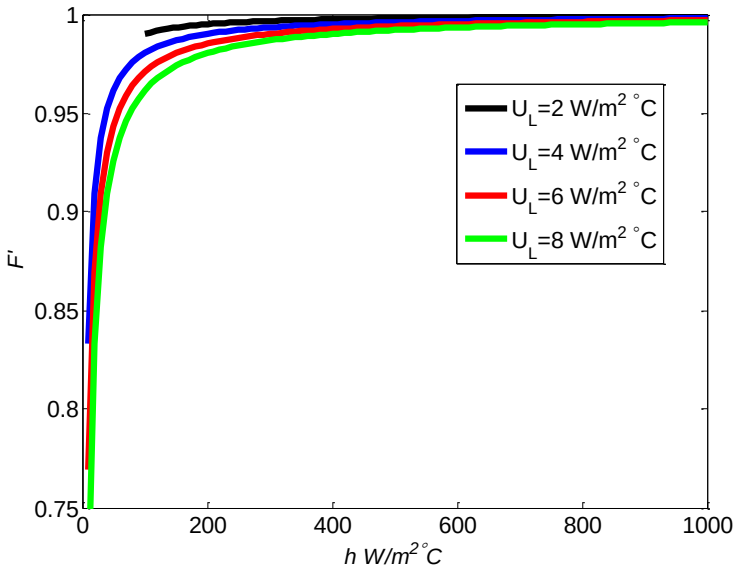

Figure 3.5: Collector efficiency factor versus heat transfer coefficient

Figure 3.5 shows a plot of the collector efficiency factor versus the heat transfer coefficient at different overall plate heat loss coefficient U_L. It can be observed that at a particular heat loss coefficient, increasing the heat transfer coefficient above about 200 W/m^2.°C results in marginal improvement of the collector efficiency factor. Also, the collector efficiency can be improved by reducing the overall heat loss coefficient; this will be achieved by placing the absorber plate in a vacuum envelope.

3.3 Thermal analysis in the flow (*x*) direction

A thermal analysis to obtain plate temperature distribution *T(x),* in the flow direction is conducted. The plate, has a thermal working fluid flowing through the channels at a mass flow rate $\dot{m}$, and local temperature *θ(x)*. For analysis purposes, the channel has been modeled as a flat plate having a surface area, *s*, equivalent to the four sides of the channel as shown in Figure 3.6. This figure shows a schematic of the heat and mass interaction in an elemental volume with length *Δx* and unit width. The following assumptions are made

1. The flow can be approximated as incompressible and steady state.
2. The system is perfectly insulated thus thermal losses are negligible.
3. Axial thermal conduction in the metal plate is in the flow direction only. The metal temperature is constant over a cross-section and heat transfer occurs through 4 sides of the channel.
4. The thermal properties of the plate and fluid are constant.
5. Typical flow rates for solar collectors usually yield laminar flow with very short entry regions; therefore a constant heat transfer coefficient is assumed from inlet to outlet.

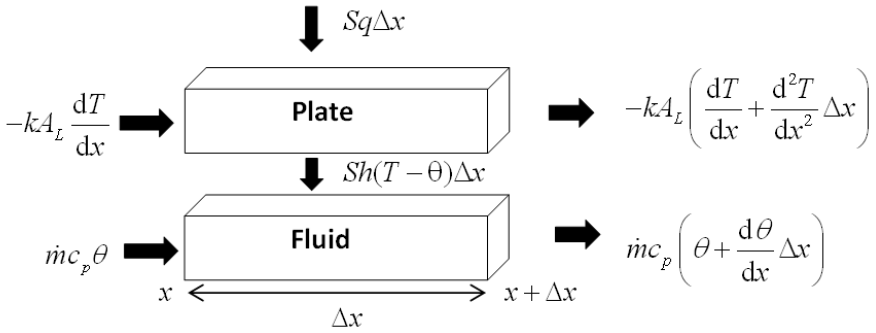

Figure 3.6: (a) Elemental volume of plate

The number of channels N_c, in a unit width of plate is given by

$$N_c = 1/\ p \tag{3.9}$$

The circumference of the channel is

$$s = 2(a+b) \tag{3.10}$$

Therefore, the total circumference of all channels in a plate is

$$S = sN_c \tag{3.11}$$

Note that the total surface area is a product of the circumference and the length

$$S_c = SL \tag{3.12}$$

The ratio of top surface area to the heat transfer surface area is given by

$$A_{pc} = \frac{p}{s} = \frac{P}{S} \tag{3.13}$$

The heat flux from the channel walls per unit length of collector is

$$q_c = q_t A_{pc} \tag{3.14}$$

The cross sectional area for thermal conduction in the longitudinal direction is given by

$$A_L = \delta P - \left(N_c ab\right) \tag{3.15}$$

To predict the plate temperature T and fluid temperature θ as a function of the position x, in the flow direction, the conservation of energy principle is applied on the elemental volume of plate and fluid, shown in Figure 3.6.

The useful solar energy into this elemental region will be

$$q'_u = Sq_c\Delta x \tag{3.16}$$

The thermal energy conducted into the plate of the elemental volume will be

$$q_{condx} = \left(-kA_L \frac{dT}{dx}\right)\Bigg|_x = -kA_L \frac{dT}{dx} \tag{3.17}$$

The heat conducted out of the elemental volume will be

$$q_{cond\,\Delta x+x} = \left(-kA_L \frac{dT}{dx}\right)\Bigg|_{x+\Delta x} = -kA_L\left(\frac{dT}{dx} + \frac{d^2T}{dx^2}\Delta x\right) \tag{3.18}$$

The heat transferred out of the elemental region by convection will be

$$Sh(T-\theta)\Delta x \tag{3.19}$$

Therefore, the energy balance on the plate can be represented by

$$Sq\Delta x + \left(-kA_L \frac{dT}{dx}\right) - \left(-kA_L\left(\frac{dT}{dx} + \frac{d^2T}{dx^2}\Delta x\right)\right) - Sh(T-\theta)\Delta x = 0 \tag{3.20}$$

Simplifying and dividing by $kA_l\Delta x$ yields

$$\frac{\mathrm{d}^2T}{\mathrm{d}x^2} - \frac{Sh}{kA_L}(T-\theta) + \frac{Sq}{kA_L} = 0 \tag{3.21}$$

This is a second order differential equation which requires two boundary conditions for a solution. The boundary conditions used are derived from the insulation of the plate at both ends, which can be represented as

$$\left.\frac{dT}{dx}\right|_{x=0} = 0 \tag{3.22}$$

And

$$\left.\frac{dT}{dx}\right|_{x=L} = 0 \tag{3.23}$$

Similarly, an energy balance is taken on the fluid element; the energy transferred from plate to the fluid is given in equation (3.19). The energy of the fluid entering the element is

$$q_{fx} = \dot{m}c_p\theta \tag{3.24}$$

The energy of the fluid leaving the element is

$$q_{fx+\Delta x} = \dot{m}c_p\left(\theta + \frac{\mathrm{d}\theta}{\mathrm{d}x}\Delta x\right) \tag{3.25}$$

Therefore the energy balance on the fluid element will be

$$Sh(T-\theta)\Delta x + \dot{m}c_p\theta - \dot{m}c_p\left(\theta + \frac{\mathrm{d}\theta}{\mathrm{d}x}\Delta x\right) = 0 \tag{3.26}$$

Simplifying and dividing by $mc_p\Delta x$ yields

$$\frac{\mathrm{d}\theta}{\mathrm{d}x} - \frac{Sh}{\dot{m}c_p}(T - \theta) = 0 \tag{3.27}$$

To make equation (3.27) a second order differential equation similar to equation(3.21), it is further differentiated to yield

$$\frac{\mathrm{d}^2\theta}{\mathrm{d}x^2} - \frac{Sh}{\dot{m}c_p}\left(\frac{\mathrm{d}T}{\mathrm{d}x} - \frac{\mathrm{d}\theta}{\mathrm{d}x}\right) = 0 \tag{3.28}$$

Equations (3.21) and (3.28) can be combined into one differential equation by subtracting (3.28) from (3.21). This will yield

$$\left(\frac{\mathrm{d}^2T}{\mathrm{d}x^2} - \frac{\mathrm{d}^2\theta}{\mathrm{d}x^2}\right) + \frac{Sh}{\dot{m}c_p}\left(\frac{\mathrm{d}T}{\mathrm{d}x} - \frac{\mathrm{d}\theta}{\mathrm{d}x}\right) - \frac{Sh}{kA_L}(T - \theta) + \frac{Sq}{kA_L} = 0 \tag{3.29}$$

For convenience, a variable *U*, which is the difference between fluid and plate temperature at a particular position, *x*, can be defined as

$$U = T - \theta \tag{3.30}$$

From this definition, equation (3.29) can be rewritten as

$$\frac{\mathrm{d}^2U}{\mathrm{d}x^2} + \frac{Sh}{\dot{m}c_p}\left(\frac{\mathrm{d}U}{\mathrm{d}x}\right) - \frac{Sh}{kA_L}(U) = -\frac{Sq}{kA_L} \tag{3.31}$$

From equation (3.30), it implies that the boundary conditions presented in equations (3.22) and (3.23) become

$$\left.\frac{\mathrm{d}U}{\mathrm{d}x}\right|_{x=0} = -\frac{\mathrm{d}\theta}{\mathrm{d}x} \tag{3.32}$$

And

$$\left.\frac{\mathrm{d}U}{\mathrm{d}x}\right|_{x=L} = -\frac{\mathrm{d}\theta}{\mathrm{d}x} \tag{3.33}$$

Equation (3.31) is a 2nd order differential equation of the form

$$aU'' + bU' + cU = d \tag{3.34}$$

The general solution of this form of differential equation is

$$U = CF + PI \tag{3.35}$$

It can be shown that (Stroud and Booth, 2013)

$$CF = C_3 e^{\lambda_1 x} + C_4 e^{\lambda_2 x} \tag{3.36}$$

Where λ_1 and λ_2 are the roots of the equation

$$a\lambda^2 + b\lambda + c = 0 \tag{3.37}$$

The PI can be obtained by assuming that

$$PI = U_{PI} = C_5 \tag{3.38}$$

This implies

$$\frac{dU_{PI}}{dx} = 0 \quad \text{and} \quad \frac{d^2U_{PI}}{dx^2} = 0 \tag{3.39}$$

Substituting equation (3.38) and (3.39) into (3.31) yields

$$-\frac{Sh}{kA_L}C_5 = -\frac{Sq}{kA_L} \tag{3.40}$$

Giving

$$PI = C_5 = \frac{q}{h} \tag{3.41}$$

Therefore,

$$U = C_3 e^{\lambda_1 x} + C_4 e^{\lambda_2 x} + \frac{q}{h} \tag{3.42}$$

Equation (3.42) defines the plate and fluid temperature difference in the flow direction. The fluid temperature can be obtained by re-arranging equation(3.27), which will result to

$$\frac{\mathrm{d}\theta}{\mathrm{d}x} = \frac{Sh}{\dot{m}c_p}(T-\theta) = \frac{Sh}{\dot{m}c_p}U \tag{3.43}$$

Therefore, the temperature of the fluid can be obtained by substituting equation(3.42) into (3.43) and integrating

$$\theta(x) = \int \frac{\mathrm{d}\theta}{\mathrm{d}x}\mathrm{d}x = \int \frac{Sh}{\dot{m}c_p}U dx = \left[\frac{Sh}{\dot{m}c_p}\left(\frac{C_3}{\lambda_1}\left(e^{\lambda_1 x}-1\right) + \frac{C_4}{\lambda_2}\left(e^{\lambda_2 x}-1\right)\right) + \frac{Sq}{\dot{m}c_p}x \right]_0^X \tag{3.44}$$

The plate temperature can be obtained by rearranging equation (3.30) and substituting (3.42)

$$T(x) = \left(C_3 e^{\lambda_1 x} + C_4 e^{\lambda_2 x} + \frac{qP}{Sh}\right) + \theta(x) \tag{3.45}$$

C_3 and C_4 can be obtained by differentiating equations (3.44) and (3.45) then substituting into the boundary conditions in equations (3.32) and (3.33), At x= 0, this will give

$$C_3\left(\lambda_1+\frac{Sh}{\dot{m}c_p}\right)+C_4\left(\lambda_2+\frac{Sh}{\dot{m}c_p}\right)=-\frac{Sq}{\dot{m}c_p} \qquad (3.46)$$

And at x=L

$$C_3\left(\lambda_1 e^{\lambda_1 L}+\frac{Sh}{\dot{m}c_p}e^{\lambda_1 L}\right)+C_4\left(\lambda_2 e^{\lambda_2 L}+\frac{Sh}{\dot{m}c_p}e^{\lambda_2 L}\right)=-\frac{Sq}{\dot{m}c_p} \qquad (3.47)$$

Equations (3.46) and (3.47) can be solved simultaneously to get the constants C_3 and C_4

3.3.1 Effects of design/operating parameters

Equations (3.44) and(3.45) were used to plot the fluid and plate temperature profiles for different flow rates, heat transfer coefficients and rates of axial thermal conduction. This was done for a heat transfer fluid flowing in a $1m^2$ collector micro-channel absorber plate, whose channel walls have a heat flux of 1000 W/m^2. The graphs for these plots are shown in Figure 3.7 – Figure 3.9 .

3.3.1.1 Flow rate

The range of flow rates plotted, 0.02 and 0.2 kg/s, corresponding to $10 < Re < 93$, represents the nominal operating range of an actual collector; these flow rates indicate that the thermal entry length is negligible and the flow can be approximated as thermally fully developed.

As expected, Figure 3.7 shows that the fluid and plate temperature profile changes with the change in flow rate. The axial conduction effects can be observed at both ends of the plate, this becomes less significant as the flow rate increases. Apart from the ends, the temperature difference between fluid and plate is quite similar for the most part of the fluid which is what is expected in a constant heat flux boundary condition.

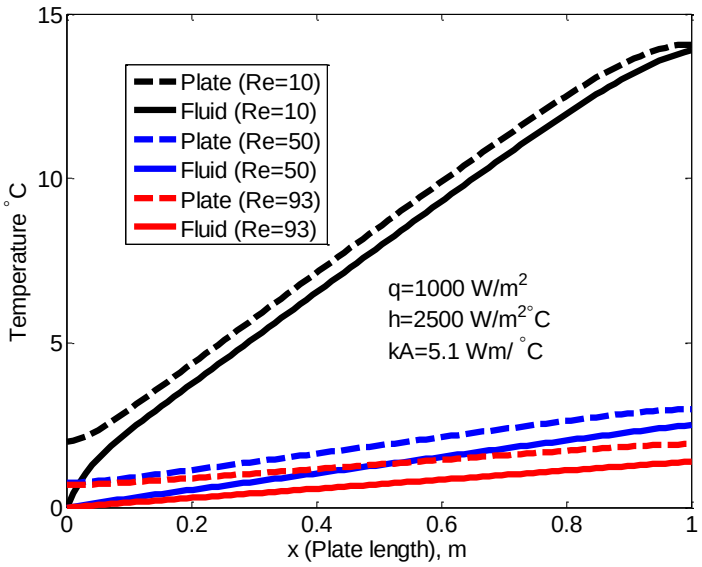

Figure 3.7: Temperature profile of fluid and metal plate at various flow rates

3.3.1.2 Heat Transfer coefficient

Figure 3.8 shows a plot covering the different possible heat transfer coefficients that can be expected from the channels (500 W/m^2 °C – 4500 W/m^2 °C). The graph shows that the fluid temperature profile remains unchanged, thus increasing the heat transfer coefficient has no effect on the fluid temperature profile, but reduces the temperature difference between metal plate and fluid. This figure further illustrates that achieving high heat transfer coefficients will bring the plate surface temperature close to fluid temperature thereby improving performance.

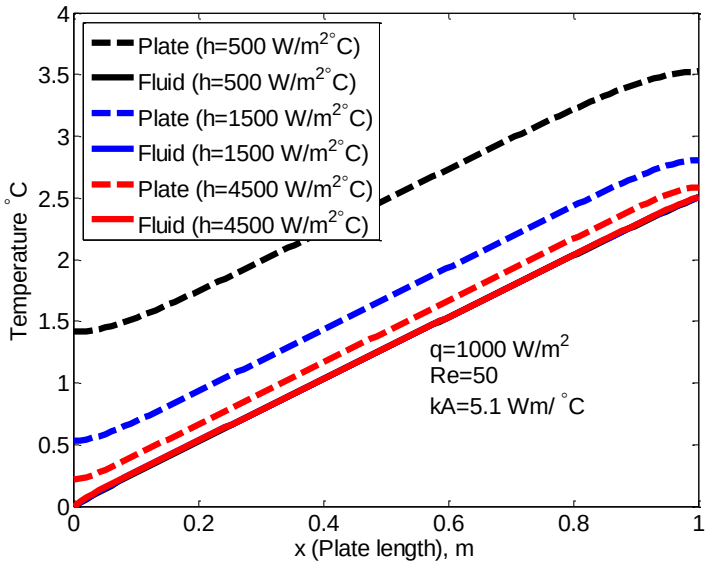

Figure 3.8: Temperature profile of fluid and metal plate at various heat transfer coefficients

3.3.1.3 Axial Thermal conduction

Figure 3.9 shows the variation of fluid and plate temperature profile along the length for varying values of kA_L. The range plotted cover actual design parameters; kA_L =0.1 – 9 Wm/ °C covers a plate made from a 3 mm PTFE sheet to a 20mm copper sheet. It can be observed that the fluid profile varies by less than 0.1°C while the plate temperature profile varies a bit more at the inlet and exit. This variation can be quite significant for plates with shorter channels. It also indicates that the sides of the plate need to be insulated properly to minimize heat loss.

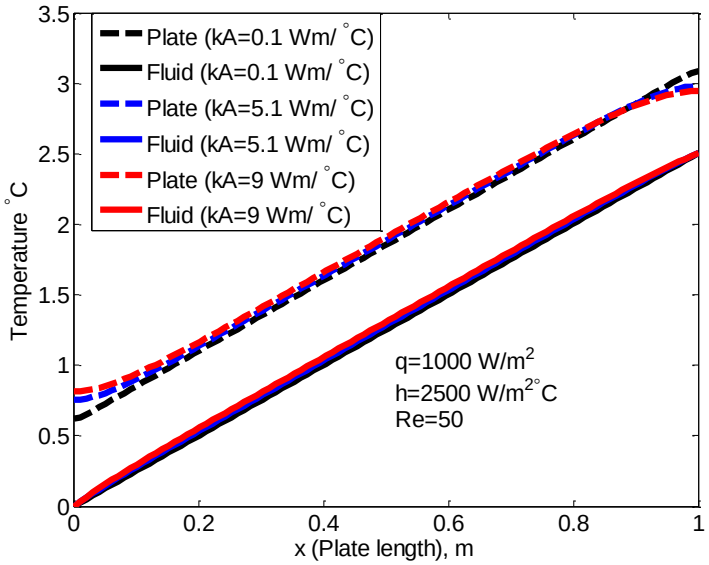

Figure 3.9: Temperature profile of fluid and metal plate at various rates of axial thermal conductivity

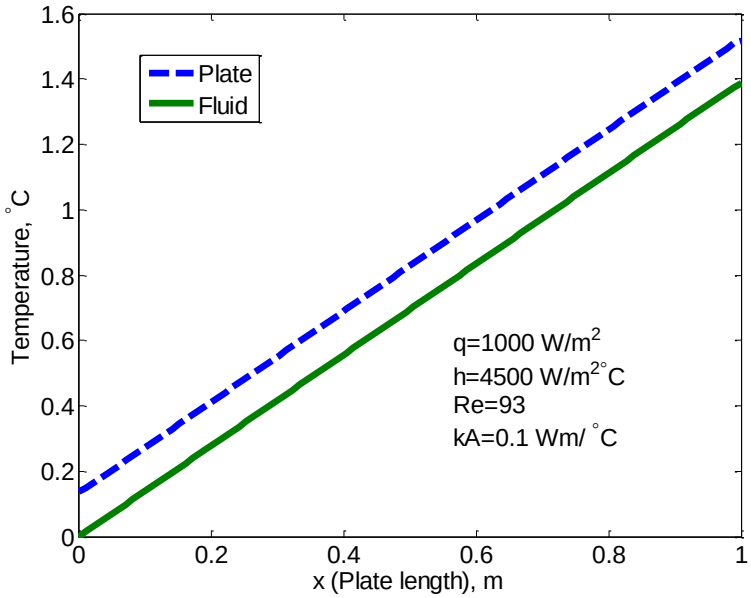

Figure 3.10: Temperature profile of fluid and metal plate for the upper extreme case

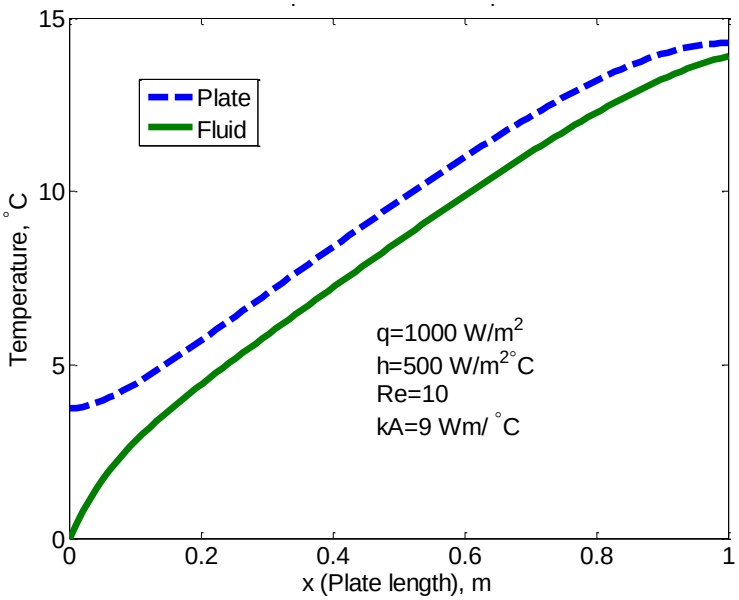

Figure 3.11: Temperature profile of fluid and metal plate for the lower extreme case

Figure 3.10 and Figure 3.11 show the plate and fluid temperature profile for two extreme cases. From Figure 3.10, it can be observed that axial thermal conduction is negligible and the difference between fluid and plate temperature profiles is constant. This is the expected trend in conventional laminar forced convection heat transfer with a constant heat flux boundary; this signifies that if axial conduction is negligible, conventional heat transfer analysis will suffice. Figure 3.11 shows a combination of a constant heat flux wall boundary condition and isothermal wall boundary condition. A trend synonymous with a constant temperature wall boundary condition is observed at the inlet and exit while the constant heat flux condition is observed at the middle section of the plate.

Figure 3.12 compares the temperature difference between plate and fluid (U) at two extreme cases, it can be observed that when the axial conduction is significant U gives an 's' shaped curve and this flattens out with reduction in axial conduction until it approximates the expected straight line for constant heat flux wall boundary

condition. It also indicates that the length of channel can make the axial conduction more pronounced.

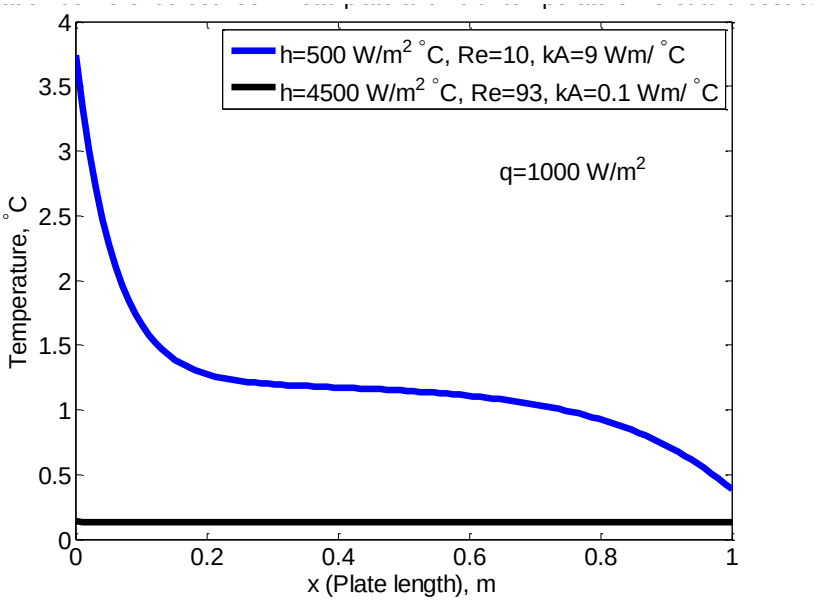

Figure 3.12: Temperature difference between plate and fluid (U) for the two extreme cases

3.3.2 The Heat Removal Factor (F_R)

The collector heat removal factor $F_{R,}$ is a quantity that relates the actual useful energy gain of a collector to the useful gain if the whole collector surface were at the fluid inlet temperature (Duffie and Beckman, 2006). This quantity can be evaluated by

$$F_R = \frac{\dot{m}C_p\left(T_{out} - T_{in}\right)}{A_c\left[q_t - U_L\left(T_{in} - T_a\right)\right]} \tag{3.48}$$

By substitution and rearrangement, F_R can also be expressed as

$$F_R = \frac{\dot{m}C_p}{A_c U_L}\left[1 - \exp\left(-\frac{A_c U_L F'}{\dot{m}C_p}\right)\right] \tag{3.49}$$

F_R can be observed to be similar to the effectiveness of a heat exchanger, which is the ratio of the heat transferred to the maximum possible heat that can be transferred. Therefore, the actual useful energy gain can be represented by

$$Q_u = A_c F_R\left[q_t - U_L\left(T_{in} - T_a\right)\right] \tag{3.50}$$

Figure 3.13 shows the variation of F_R with mass flow at various values of U_L and Figure 3.14 shows the variation of F_R with mass flow at various values of F' (F' is a function of design parameters such as *a*, *b* and *p*)

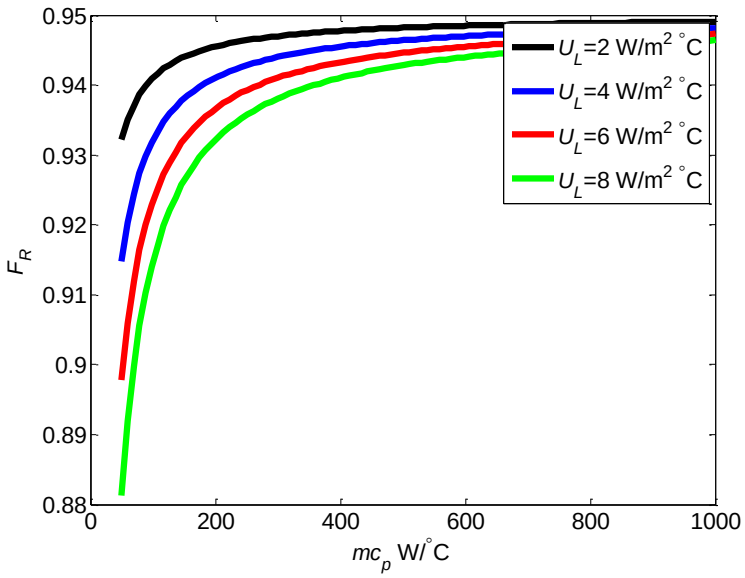

Figure 3.13: Heat removal factor versus mass flow rate at different U_L

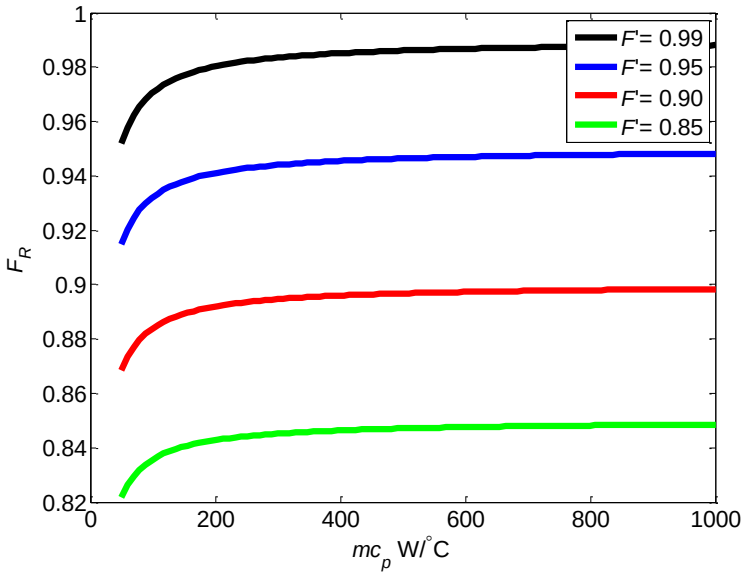

Figure 3.14: Heat removal factor versus mass flow rate at different F'

3.3.3 The Flow Factor (F'')

The collector flow factor F'' is defined as the ratio of the heat removal factor to the collector efficiency factor

$$F'' = \frac{F_R}{F'} = \frac{\dot{m}C_p}{A_c U_L F'}\left[1 - \exp\left(-\frac{A_c U_L F'}{\dot{m}C_p}\right)\right] \tag{3.51}$$

From equation (3.51), it can be observed that the flow factor is a function of a single variable which is defined as the dimensionless collector capacitance rate, CCR (Duffie and Beckman, 2006). Where

$$CCR = \frac{\dot{m}C_p}{A_c U_L F'} \tag{3.52}$$

Therefore equation (3.51) can be written as

$$F'' = CCR\left[1 - \exp\left(-\frac{1}{CCR}\right)\right] \tag{3.53}$$

Figure 3.15 shows a plot of the flow factor as a function of the collector capacitance rate, as expected, the flow factor increases with the collector capacitance rate, therefore the collector performance can be improved by increasing the mass flow rate per collector area, $\dot{m}/A_c$, and/or reducing U_L . Higher $\dot{m}/A_c$ can be achieved by pumping the fluid at higher velocities; the increased mass flow rate then also reduces the overall collector temperature rise, albeit at the expense of increased pumping power. This will result in lower losses and increase in energy gain since the collector is at a lower temperature.

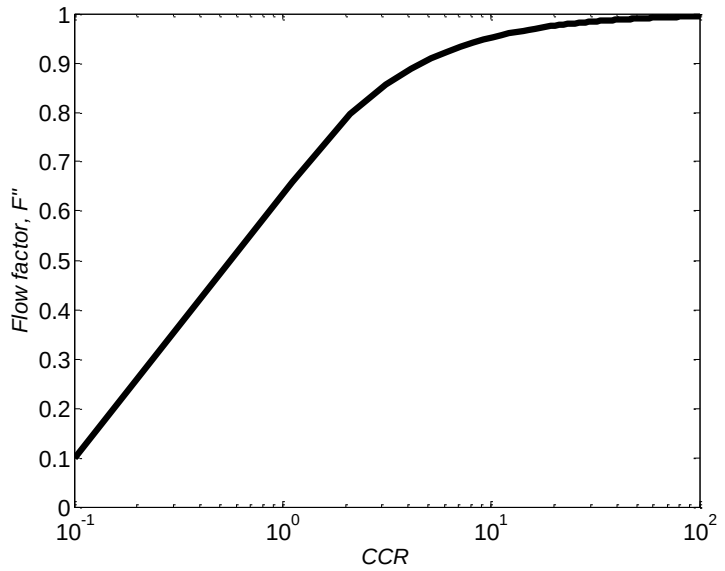

Figure 3.15: Collector flow factor versus collector capacitance rate

3.4 Summary

An analytical investigation into micro-channel absorber plates for compact flat plate collectors has been presented. Standard parameters for predicting performance of the flat plate collectors have been estimated; these include fin efficiency, *F*, collector

efficiency factor, *F'*, heat removal factor, F_R, flow factor *F''*, local plate temperature, *T(x)*, and local fluid temperature, $\theta(x)$. These were evaluated over a range covering typical flat plate collector operating values; overall heat loss coefficient in the range 2 – 8 W/m^2.°C, flow rate in the range 0.01 – 0.1 kg/s/m^2 and heat transfer coefficients in the range 200 -1000 W/m^2.°C. The results showed that values of *F* and *F'* very close to unity can be achieved with this design when the overall heat loss coefficient is below 2 W/m^2.°C. The analysis further revealed that increasing the fluid-plate heat transfer coefficient beyond 300 W/m^2.°C has marginal effect on the collector efficiency factor at a given U_L value. It was also observed that the effect of axial thermal conduction can significantly alter the temperature profile of the metal plate and should be accounted for, especially in short plates. The collector flow factor *F''* and the heat removal factor can be improved by increasing the collector capacitance rate; this can be achieved by increasing the mass flow rate per collector area $\dot{m}/A_c$, as well as reducing the overall heat loss, U_L.

4. Experimental Setup and Data Acquisition

4.1 Background

The analysis presented in chapter 3, suggests that very high performance can be obtained from the micro-channel absorber plate design. However, the review of literature (chapter 2), indicate that traditional heat transfer and fluid flow correlations could yield misleading results due to scaling effects in micro-channels. Hence, an experimental study proves to be a necessity in predicting actual thermal and hydraulic behaviour of these micro-channel plates. Therefore, experiments were designed to closely match real life operation of the proposed compact solar collector. These experiments were aimed at measuring performance accurately as well as investigating the significance of scaling effects.

The essential parameters needed for estimating performance include heat transfer coefficient (h), Nusselt number (Nu), fluid velocity (v), Reynolds number (Re), pump power (P) and friction factor (f). The quantities required to be measured experimentally to calculate these parameters are plate temperatures (T_p), fluid temperature at inlet, (T_{in}), fluid temperature at outlet (T_{out}), mass flow rate, ($\dot{m}$) and pressure drop (Δp). other quantities such as the specific heat capacity (C_p), density (ρ) and thermal conductivity (k) are fluid properties that can be obtained from the literature. This chapter gives a detailed explanation of the two test rigs that were designed (the heated sandwich and the counter flow heat exchanger); it also discusses the various components of the experimental apparatus, how they were calibrated and the various design considerations. The procedures adopted for data analysis are also presented.

4.2 Heated Sandwich

4.2.1 Description

One of the aims of this experiment was to investigate optimal geometry effects of the channel geometry hence a rig, which allowed a variety of relatively simple channel plates to be tested without each needing its own inlet and outlet connections, was made. It consisted of two 340 × 240 × 10 mm aluminium slabs – a "top" and "bottom" piece, with the thinner (3 mm) micro-channel plate sandwiched between them. The sandwich was held together by M4 screws along the edges with an O-ring ensuring a leak tight seal. A cross section of the test rig is shown in Figure 4.1. Longitudinal and transverse 3D cross sections are shown in Figure 4.2 and Figure 4.3 The rig was insulated with a box constructed from Polyisocyanurate foam.

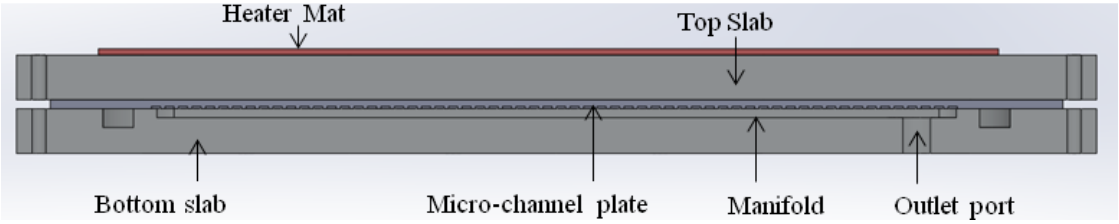

Figure 4.1: Cross section of test rig through outlet port

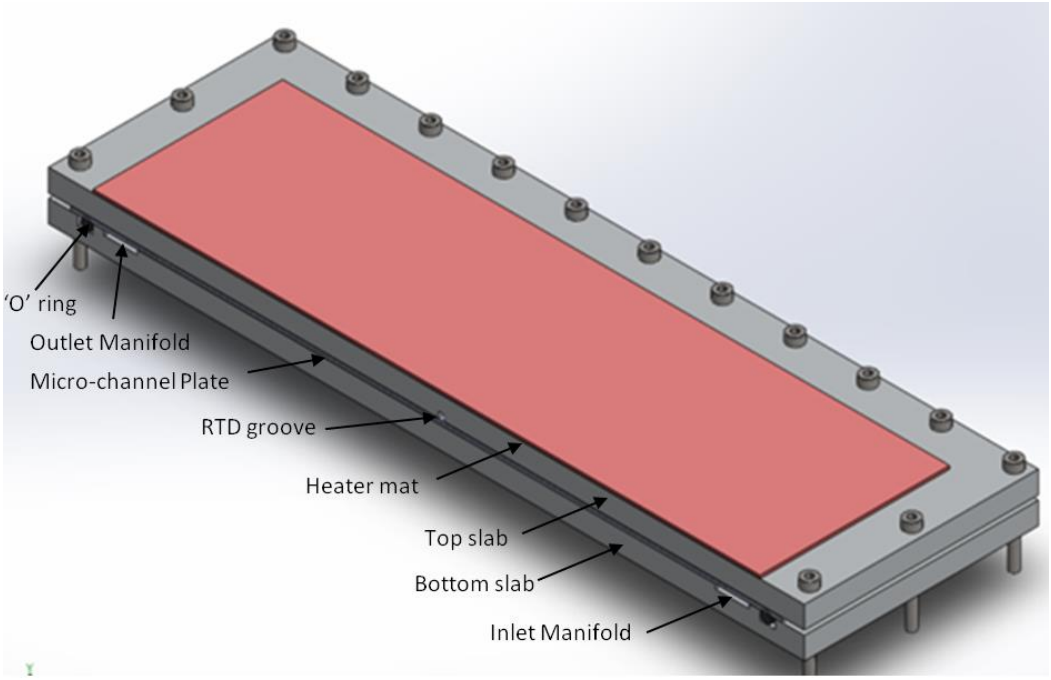

Figure 4.2: Longitudinal 3D section of test rig

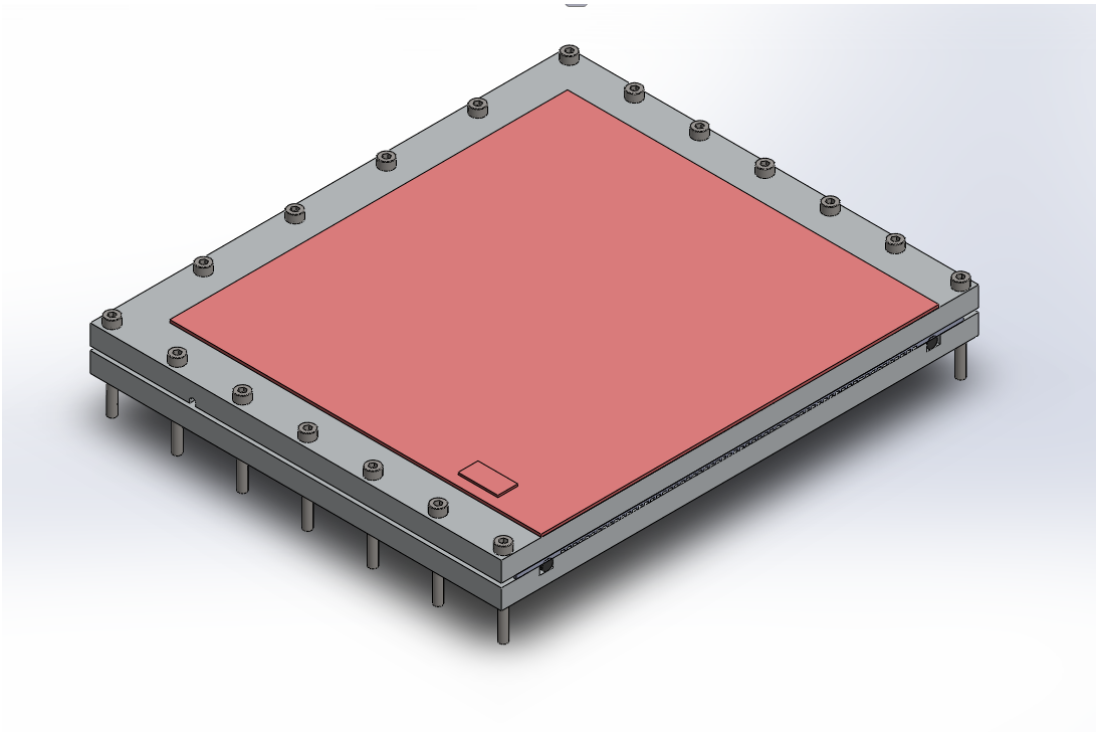

Figure 4.3: Transverse 3D section of test rig

Absorbed solar irradiation was simulated with self-adhesive heater mats, capable of supplying heat flux density in the range 100 W/m^2 – 5000 W/m^2. These were mounted on the the upper face of the top slab. The uniformity of the heat flux imposed by the heater mat was validated in two ways; firstly, an infrared camera was used to check the temperature profile on the resistance heater. This was done by quickly removing the insulation to take the infrared picture – a maximum variation of less than 0.25 °C was observed longitudinally when the plate temperature was about 30°C. Secondly, the transient temperature profile of the micro-channel plate was examined when the heater mat was turned on with no flow through the channels. A uniform temperature profile was observed on the plate, which signifies a uniform heat flux from the mat.

The 10 mm thickness of the slab and relatively high thermal conductivity of aluminum implied that an even heat flux from the lower surface of the bottom slab can be expected. Thermocouples were embedded between the mat and the slab for heat loss calibration and grooves were machined on the lower face of the top slab. These grooves were for positioning Resistance Temperature Detectors (RTDs) required for measuring the micro-channel plate temperature.

The lower face of the bottom slab had a BS 381 O-ring groove and two 180 × 15 × 2 mm manifolds machined on it. Each manifold had a ¼" BSP connection port (for fluid entry and exit); the ports were located at opposite sides to promote even distribution of the fluid across the plate; the positions of the manifold and ports are illustrated in Figure 4.4a. Three pieces of the bottom slab were made, each from a different material; Aluminum, Perspex and PTFE. The aluminum was the default slab used while the PTFE slab was made to investigate the effect the thermal wall

boundary condition. The Perspex slab was made to enable visualization of the flow through the channels.

The fluid temperature at inlet (T_{in}) and outlet (T_{out}), were measured using thermocouples and RTDs. These temperature probes were placed inside the ports after elbow fittings to promote fluid mixing and ensure accurate bulk fluid temperatures were read. Thermocouples were stuck at the outside walls of these ports as a second check of the fluid temperature measurements.

Figure 4.4: (a) Inner face of Test Rig (b) Thermocouple arrangement on plate

A total of 10 plates measuring 320 × 225 × 3 mm having 270 mm long channels were made, Table 4.1 presents the geometric details of the plates; the channels on 8 plates were made by machining with a circular saw while the channels on the other 2 plates were made by an etching procedure. Figure 4.6 shows pictures of some plates, the fourth side of the channel was formed by the bottom slab that was clamped in place hard against the inter-passage ribs. Figure 4.4b shows the arrangement of thermocouples stuck on top of the micro-channel absorber plate to measure the plate temperatures, (T_{pi}), at different points. A schematic showing the position of the thermocouples is shown in Figure 4.5

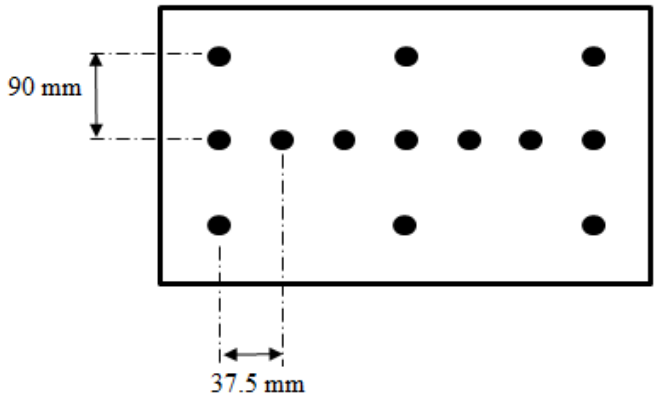

Figure 4.5: Schematic showing thermocouple positions

Table 4.1: Geometric parameters of the channels

Plate	N_c	a (mm)	b (mm)	P (mm)	L(mm)	D_h (mm)	$\alpha = a/b$
Machined							
A	180	0.5	0.5	1	270	0.5	1
B	72	1	2	2.5	270	1.33	0.5
C	60	1	2	3	270	1.33	0.5
D	60	0.75	2	3	270	1.1	0.375
E	60	0.5	2	3	270	0.8	0.25
F	60	0.25	2	3	270	0.44	0.125
G	45	1	2	4	270	1.33	0.5
H	36	1	2	5	270	1.33	0.5
Etched							
K	180	0.5	0.5	1	270	0.5	1
L	60	0.5	2	3	270	0.8	0.25

The flow rate ($\dot{m}$) and pressure drop (Δp) were measured using a Corriolis mass flow meter and a differential pressure sensor respectively. Pipes and fittings in the hydraulic loop were insulated. All the measured quantities were logged with a 16-bit National Instruments data acquisition system via Labview. Thermocouples were connected through a SCXI-1102 thermocouple interface board.

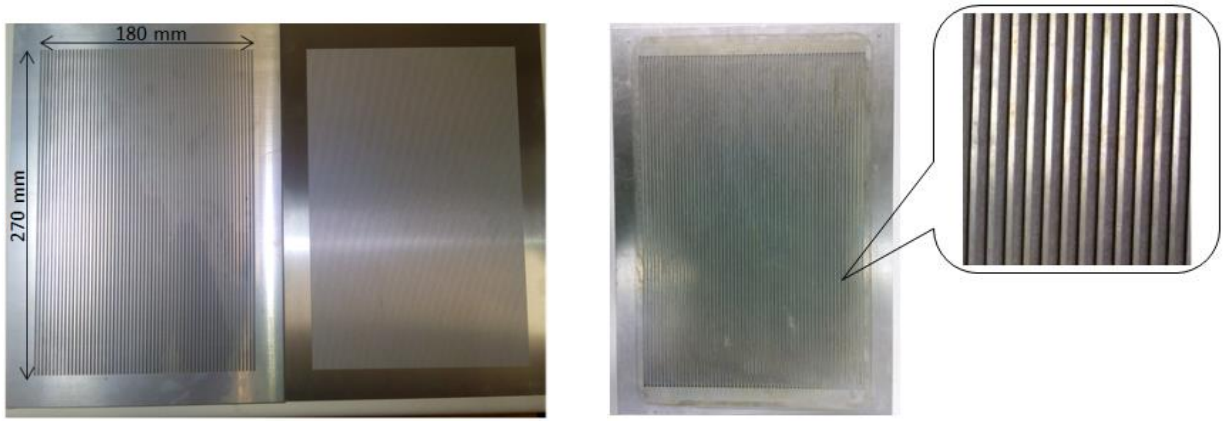

Figure 4.6 : Picture showing some of the plates

A flow schematic of the experimental setup is shown in Figure 4.7; a temperature controlled circulating bath supplied the heat transfer fluid at constant flow rate and temperature to the heated sandwich, in a closed loop hydraulic system. Figure 4.8 shows the actual experimental setup. Details of the various components in the setup are discussed in section 4.4.

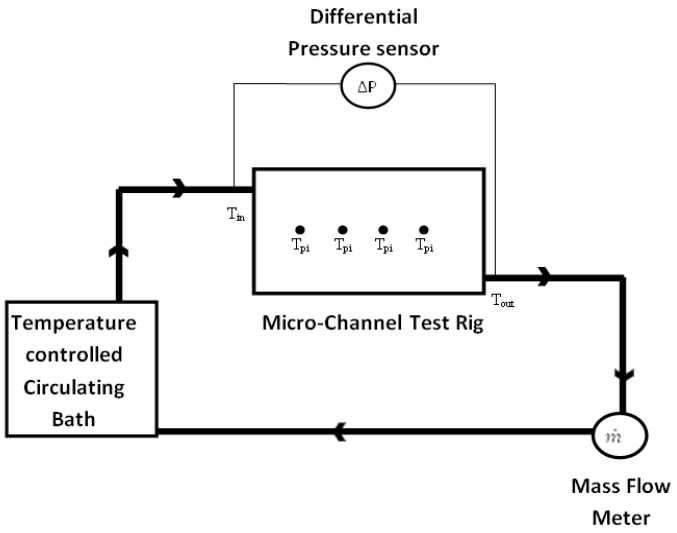

Figure 4.7: schematic of experimental setup

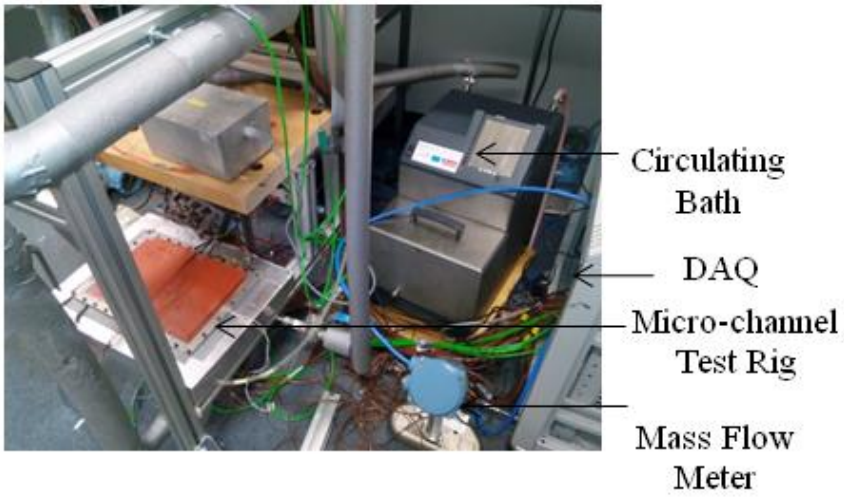

Figure 4.8: Actual experimental setup

4.2.2 Design considerations

4.2.2.1 Clamping Force to withstand pressure of liquid

The circulating bath used has a maximum delivery pressure (head) of 70 kPa . The fluid flows between the plate and bottom slab (face area is 340 × 240 mm). Therefore, the maximum force exerted on the plate by the fluid can be estimated from

$$F_f = P_f \times A_p \tag{4.1}$$

Substituting values will result in

$$F_f = 70 \times 0.24 \times 0.34 = 5.712kN \tag{4.2}$$

Thirty (30) grade 12.9 M4 cap screws, with a maximum axial force, F_{screw} = 6.75KN (Budynas, 2011), were used to clamp the test rig together. The screws were closely spaced (46 mm along the breadth and 32.8 mm along the length) to keep the edges

rigid, this arrangement is shown Figure 4.9. Therefore, the total compressive force exerted by the screws will be

$$F_{ScrewTotal} = 6.75 \times 30 = 202.5kN \tag{4.3}$$

And the resulting compressive stress will be

$$\frac{F_{ScrewTotal}}{A} = \frac{202.5}{0.24 \times 0.34} = 2481kPa \tag{4.4}$$

Comparing the maximum force exerted by the fluid (4.2) to the total compressive force exerted by the screws (4.3), it can be observed that

$$F_{ScrewTotal} \gg F_f \tag{4.5}$$

This shows that the screws exert sufficient force to withstand the pressure of the flow.

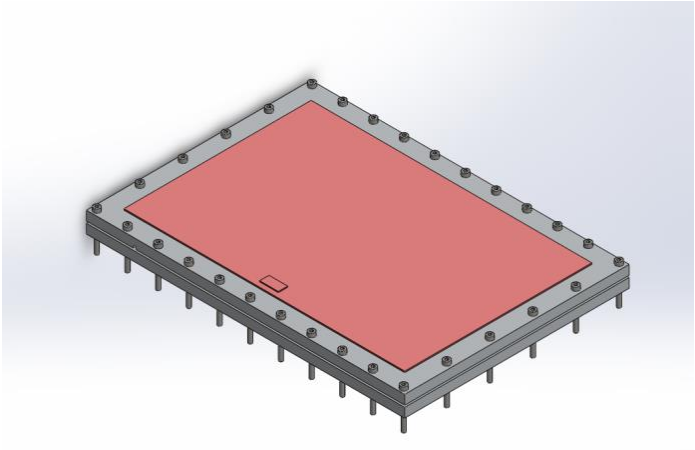

Figure 4.9: Isometric view of test rig showing fasteners

4.2.2.2 Deflection and thermal expansion of Slabs and Plates

The maximum deflection of a flat plate whose edges are rigidly fixed is given by (Budynas, 2011)

$$y_m = C_6 \frac{P_s L_x^{\,4}}{E\delta^3} \tag{4.6}$$

The linear thermal expansion can be estimated by

$$\Delta L = \alpha_{TE} L \Delta T \tag{4.7}$$

Table 4.2 shows the values of maximum deflections and thermal expansion of the plates and slabs. These were obtained by substituting values into equation (4.6) and (4.7). Since the values of maximum deflection are small, it may be concluded that its effects can be neglected. The engineering drawing presented in Figure 4.10 shows that 1 mm allowances were made between the plate and the screws. This implies that the plate can expand along the length and width thus preventing deflection of the plate due to thermal expansion. Also since the components are made of the same material, there will be no bimetallic deflection.

Table 4.2: Deflection and expansion of slabs

Component	x_m **(mm)**	y_m **(mm)**	$x_{\alpha TE}$ **(mm)**	$y_{\alpha TE}$ **(mm)**
slabs	0.04	0.01	0.63	0.44
Plate	0.4	1.3	0.63	0.44

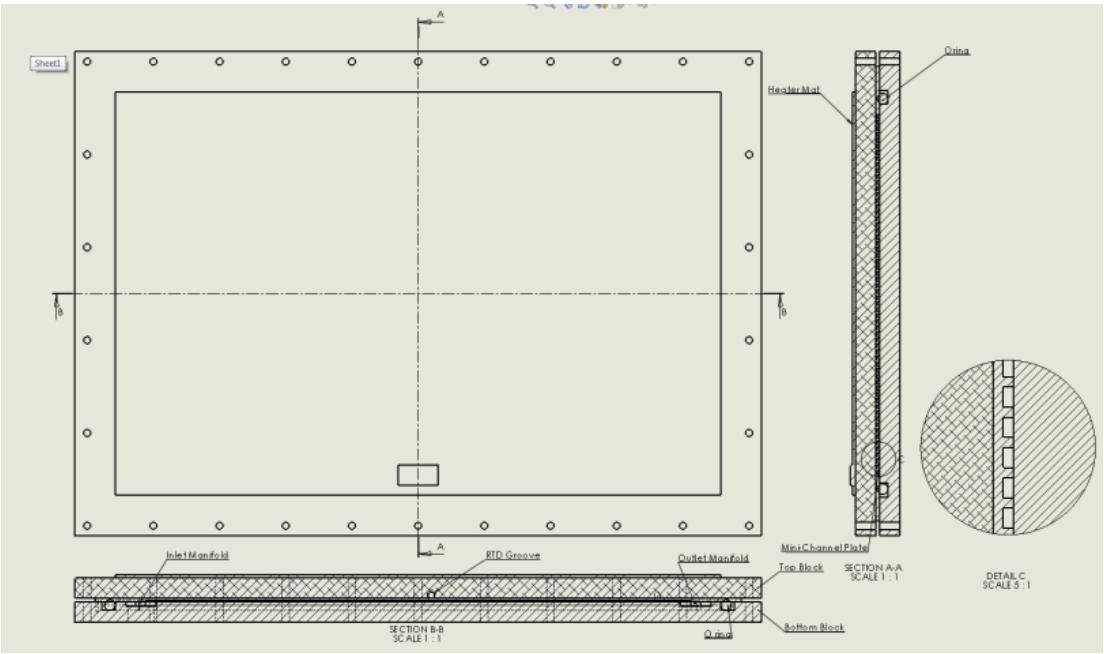

Figure 4.10: Engineering Drawing of the Test Rig

4.2.2.3 Thermal Resistance at Plate – Top slab interface

A thermal analysis was done on the test rig to validate its performance. Figure 4.11 shows the schematic of the thermal network representing the test rig. One of the most important segments is the interface between the top slab and the micro-channel plate. This segment is crucial because 0.25 mm diameter thermocouples measuring plate temperatures are located here. It was difficult to measure the thermal contact resistance at this interface; hence this segment can pose significant uncertainty in plate temperatures measured. Thermal resistance details of each segment are shown in Table 4.3, four different scenarios for the interface are presented; filling the interface with 1 mm of grease and 3 different effective gap thicknesses (filled with air). From this table, it can be observed that the scenario, in which the interface is filled with 1 mm layer of grease, shows that thermal resistance can be reduced by a factor of 10 compared with having an effective 0.1 mm air gap and by a factor of 60

with a 0.5 mm air gap. This method was initially adopted and some experiments were run with grease at the interface. However, this proved to be very challenging because, firstly, it was difficult to apply an even surface of grease and secondly, the grease layer was observed to be distorted after experiments, as shown in Figure 4.12. This distortion was due to changes in viscosity which resulted from extreme temperature changes during experiments.

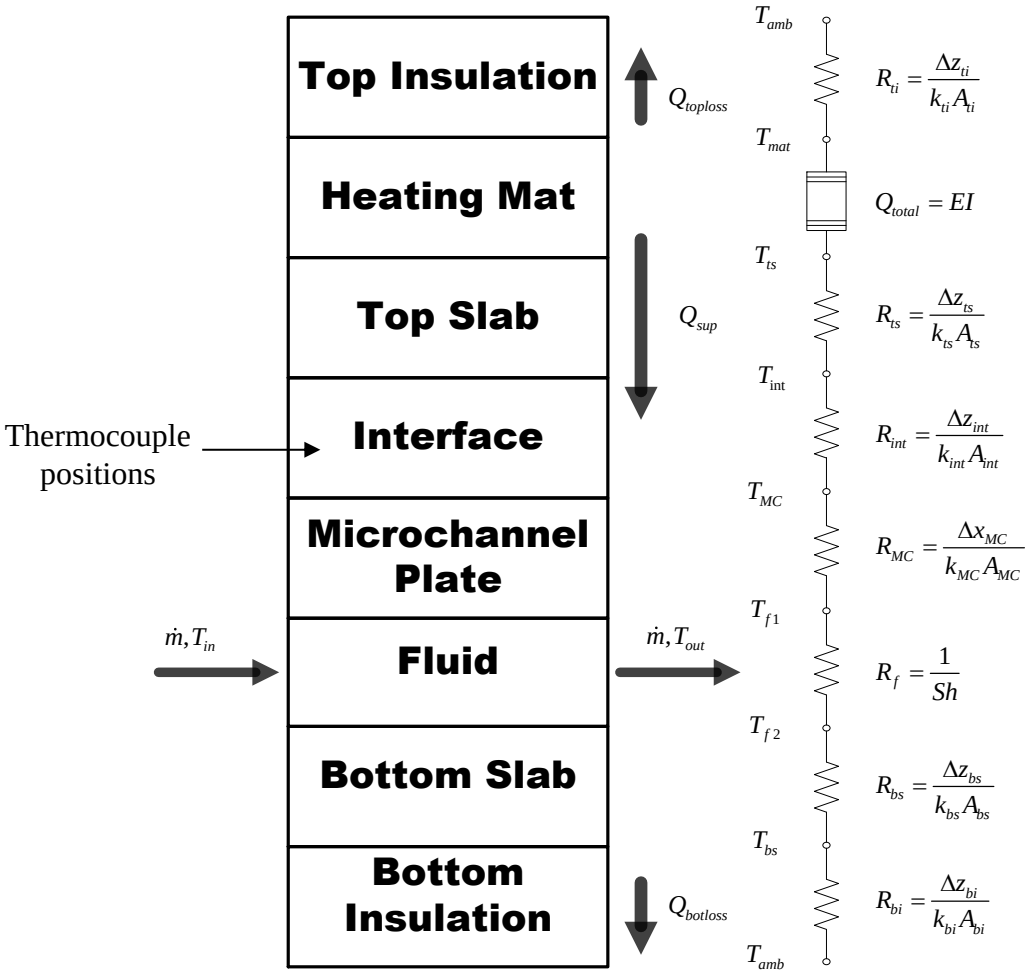

Figure 4.11: Schematic of thermal resistances in the test rig

Table 4.3: Thermal Resistance Details of Test rig Segments

Component	Material	$A(cm^2)$	$k(W/m^{\circ}C)$	$\Delta z(mm)$	$R(\mathrm{m}W/^{\circ}C)$
Top Insulation	Polyisocyanurate	1575	0.022	50	14430
Top slab	K6082 Aluminum	816	180	10	0.681
Interface (1)	Air	720	0.02	0.1	69.44
Interface (2)	Grease	720	2.31	1	6.013
Interface (3)	Air	720	0.02	0.2	138.9
Interface (4)	Air	720	0.02	0. 5	347.2
Micro-channel plate	K6082 Aluminum	720	180	3	0.231
Bottom slab	K6082 Aluminum	816	180	1	0.681
Bottom insulation	Polyisocyanurate	1575	0.022	50	14430
Thermal Attachment pads	Fiber Glass fabric	0.15	2.64	0. 1	252.5

The temperature difference across the interface can be quite substantial if the grease layer is removed. This can cause significant uncertainties in temperatures measured by thermocouples and RTDs. Also, the thermocouple tips have very low thermal resistance; this implies a potential for higher rates of heat flow through the tips, which can compromise the plate temperature readings. The strategy adopted to overcome these challenges was to use adhesive fiber-glass thermal attachment pads. These pads were used to stick the thermocouples to the plate and act as a thermal insulation between the top slab and the tips of the thermocouples; the high thermal resistance of the fiber glass reduces the chances of making the 0.5 mm thermocouple tips a path for thermal conduction. Similarly, putting a number of the thermal attachment pads, which were uniformly distributed, promoted a uniform air gap contributing to a fairly even thermal resistance between the plate and top slab. Though, this approach leads to a significant thermal gradient at the interface, the thermal attachment pads increases the probability of the thermocouples reading the temperature of the plate rather than the interface.

The interface thickness was then checked by comparing the sum of the individual thicknesses of the slabs and plate, to the thickness of the clamped sandwich (procedure for measuring the sandwich is shown in Figure 4.12b).

The surface contact between the micro-channel plate and the bottom slab was checked in two ways. Firstly, an imprint the channel ribs can be seen on top surface of the bottom slab in Figure 4.4a, which suggests good contact between the channel ribs and the bottom slab. Secondly, the Perspex bottom slab was used to visualize the flow; the fluid was observed to flow through individual channels suggesting that the ribs between channels were in good contact with the bottom slab. Therefore the difference between the sum of the individual components thickness and the assembled sandwich thickness can be concluded to be the interface thickness; this was found to be approximately 0.15 mm .

Figure 4.12: (a) Distortion of grease layer (b) Procedure for measuring the sandwich

4.2.2.4 Heat loss

The insulation box has a very high thermal resistance (see Table 4.3), hence it is expected that the bulk of the heat flux from the heater mats, will ultimately be transferred to the fluid. However, since the insulation is not perfect, some of the

heat will be lost to the ambient. This heat loss was estimated by applying the conservation of energy principle (assuming no internal heat generation and negligible heat loss from the sides) as illustrated in Figure 4.11.

The heat loss from the top insulation will be

$$Q_{toploss} = R_{ti}\left(T_{mat} - T_{amb}\right) \tag{4.8}$$

The heat loss from the bottom insulation will be

$$Q_{botloss} = R_{bi}\left(T_{bs} - T_{amb}\right) \tag{4.9}$$

The heat absorbed by the top slab which is then transferred to the micro-channel plate (since side losses are negligible) will be

$$Q_{sup} = Q_{total} - Q_{toploss} \tag{4.10}$$

Therefore, the heat supplied to fluid should be equal to the enthalpy change.

$$Q_{fluid} = Q_{sup} - Q_{botloss} = \dot{m}c_p\left(T_{out} - T_{in}\right) \tag{4.11}$$

However, when experimental data were analysed, the equality in equation (4.11) did not hold. This could be attributed to the imperfect insulation at joints and at points where instruments/piping pass through. Heat loss to the ambient can be amplified as a result of these. A modified method of estimating the heat loss, equation(4.12), was therefore adopted.

$$Q_{loss} = VI - \dot{m}c_p\left(T_{out} - T_{in}\right) \tag{4.12}$$

This is the difference between the electrical power consumed by the heater mats and the enthalpy change in the fluid. This method provided higher certainty as fluid temperature at inlet and exit could be checked in about three ways; the temperature probes inside the ports, the thermocouples at the outside walls of the ports and the control panel of the temperature controlled bath. Similarly, the mass flow meter was checked by timing flow into a measuring cylinder (details of calibrations/checks of all instruments are presented in section 4.4). Figure 4.13a shows the heat loss as a function of mass flow rate at various temperatures. The heat loss in this figure is defined as

$$Q_{loss} = 1 - \frac{\dot{m} c_p \left(T_{out} - T_{in} \right)}{VI} \tag{4.13}$$

It can be observed that above flow rates of 10 g/s, the heat loss can be seen to be fairly constant at a given temperature. Also, as expected, the heat loss increases with temperature. Figure 4.13b shows the heat loss as a function of power supplied, a linear relationship can be observed and the heat loss can be seen to be a function of the power supplied. It should be noted that the ambient temperature was fairly constant (around 22 °C) for all experiments.

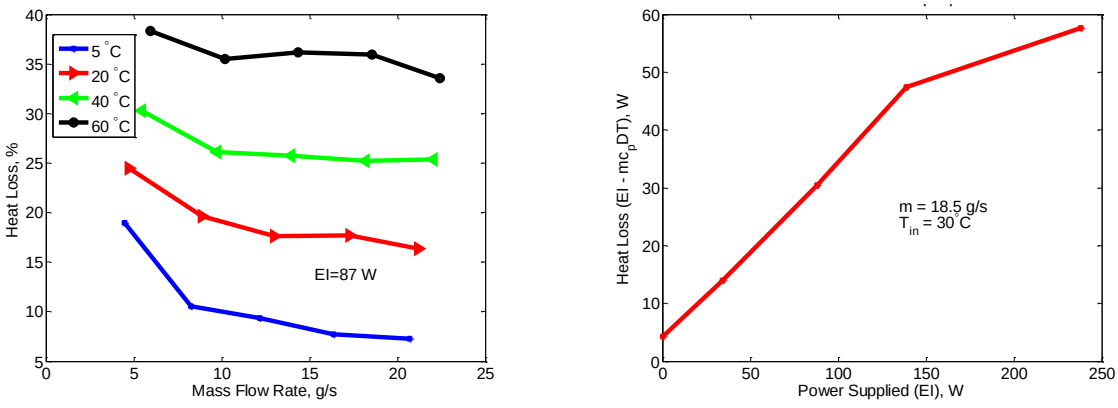

Figure 4.13: Heat loss at different (a) temperatures (b) input power

4.2.2.5 Temperature differences

The temperature difference across the interface will be

$$\Delta T_{int} = Q_{sup} R_{int} \tag{4.14}$$

The thermal resistance across the sandwich (between top and bottom insulation) will be

$$R_{rig} = R_{ts} + R_{int} + R_f + R_{bs} \tag{4.15}$$

The expected temperature difference between the upper face of the top slab and the lower face of the bottom slab will be

$$\Delta T_{rig} = Q_{sup} R_{rig} \tag{4.16}$$

This will result in a temperature gradient across the test rig of

$$\frac{\Delta T_{rig}}{z_{rig}} \tag{4.17}$$

Figure 4.14 compares the measured temperature gradient to predictions for three (3) interface thicknesses. It can be observed that at heat fluxes below 100 W (which corresponds to heat fluxes used for most experiments), the measured temperature gradient is between predicted temperature gradients for 0.1 mm and 0.2 mm thick interface. This is similar to the interface thickness obtained from measurement procedure outlined in sub – section 4.2.2.3.

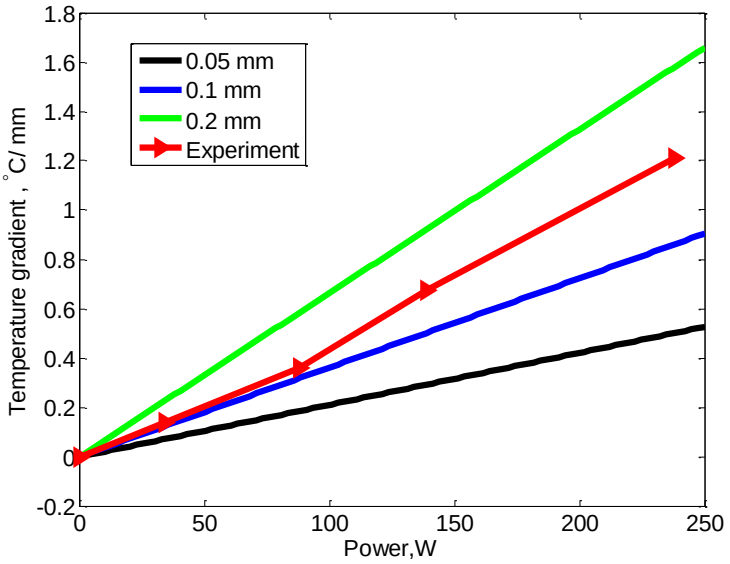

Figure 4.14: Temperature gradient across test rig

4.2.3 Data Reduction

Post steady state data were used for analyses. The criterion for steady state was defined by

$$\frac{dT}{dt} < 2.5\times10^{-5}\ ^{\circ}\text{C/s} \tag{4.18}$$

This was reached after approximately 10–15 minutes for any given constant flow rate. The mean of about 200 data points, after reaching steady state were used for analysis. This sample size is sufficiently large to minimize errors in estimating the mean (Holman, 2012), giving a typical standard deviation of 0.016 °C. Below are some of the main parameters estimated from the measured quantities.

4.2.3.1 Mean plate temperature

The mean plate temperature T_p, was estimated by taking an average of all the thermocouples on the plate.

$$T_p = \frac{\sum_{i=1}^{n} T_{pi}}{n} \tag{4.19}$$

4.2.3.2 Mean fluid temperature

The mean fluid temperature, T_f was estimated as the average of the inlet and outlet fluid temperatures. Thermo physical properties of the fluid such as specific heat capacity, thermal conductivity and dynamic viscosity were estimated at the mean fluid temperature.

$$T_f = \frac{T_{in} + T_{out}}{2} \tag{4.20}$$

4.2.3.3 Heat flux

The heat flux to the fluid was estimated using the enthalpy change in the fluid (assuming negligible viscous heating). As noted in sub – section 4.2.2.4, this method is a more reliable option due to heat losses that may not be accounted for. Therefore, the heat flux into the fluid will be

$$Q_{fluid} = \dot{m} c_p \Delta T_f \tag{4.21}$$

Where

$$\Delta T_f = \left(T_{out} - T_{in}\right) \tag{4.22}$$

4.2.3.4 Surface Area

The surface area available for heat transfer will be

$$S_c = 2N_c L(a+b) \tag{4.23}$$

4.2.3.5 Heat transfer coefficient

The heat transfer coefficient was estimated by rearranging Newton's law of cooling which yields

$$h = \frac{Q}{S_c\left(T_p - T_f\right)} \tag{4.24}$$

4.2.3.6 Pumping power per collector area

The power required per collector area was estimated by

$$\dot{w} = \left(\frac{\dot{m}}{A_p}\right)\frac{\Delta p}{\rho} \tag{4.25}$$

4.2.3.7 Friction Factor

The friction factor was estimated by

$$f = \Delta p \frac{D_h}{L}\frac{2}{\rho v_m{}^2} \tag{4.26}$$

Details of other parameters estimated from the measured quantities are presented in the relevant chapters. Comprehensive results from this test rig are presented in chapter 6.

4.3 Counter Flow Heat Exchanger

A different test rig was designed to confirm the results obtained (presented in chapter 6) from the heated sandwich test rig. Some of the objectives of this test rig design are

I. This test rig was made as a counter flow heat exchanger to eliminate uncertainties resulting from the thermal contact resistance at the interface of the heated sandwich.
II. The micro-channels were made longer to ensure a higher percentage of fully developed flow .
III. The rig was designed to have much higher heat fluxes into the fluid; this was done to reduce the magnitude of errors in estimating the heat transfer coefficient (i.e. higher heat flux implies higher temperature and a reduction in the percentage error from thermocouple measurement).
IV. This test rig was made to have fewer channels for a more even flow distribution between channels.

4.3.1 Description

The counter flow heat exchanger was made up of two identical 540 × 80 × 10 mm aluminum slabs – a “hot” and “cold” side. A thinner (4 mm) plate with 2 mm micro-channels on both faces, was sandwiched between the two slabs. A cross section illustrating the arrangement is shown in Figure 4.15 . The slabs and plate were held together by M4 fasteners along the edges. A Polyisocyanurate box was used to insulate the test rig.

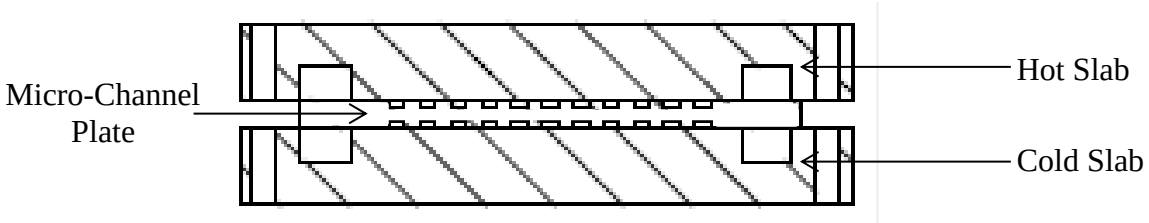

Figure 4.15: Cross section of counter flow heat exchanger

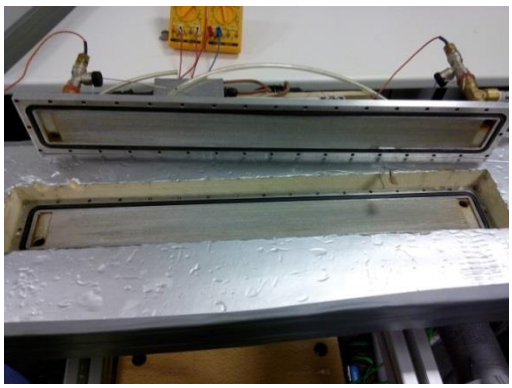

Figure 4.16: Inner faces of slabs

Figure 4.16 shows the inner faces of the two slabs; each slab had two 45× 15 × 2 mm manifolds machined on opposite ends. The thermal working fluid entered and exited the manifolds through ¼" BSP fittings which were located diagonally across each other. These faces had grooves for O – rings to be placed to ensure a firm seal. Five (5) thermocouples (arranged 125 mm apart) were mounted on the outer faces of both slabs (as shown in Figure 4.17). These were used to measure the temperature of the hot and cold side slabs (T_{shi} and T_{sci}). One thermocouple and one RTD were placed inside each of the 4 ports. These were used to measure fluid inlet (T_{hin} and T_{cin}) and fluid outlet (T_{hout} and T_{cout}) temperatures. These temperature probes were inserted after elbow fittings to promote fluid mixing and ensure accurate bulk fluid temperatures were read. Thermocouples were also stuck at the outside walls of these ports as a second check for fluid temperature measurements.

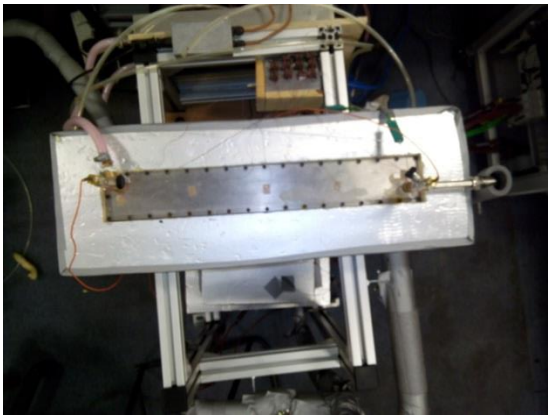

Figure 4.17: Thermocouple arrangement on slab

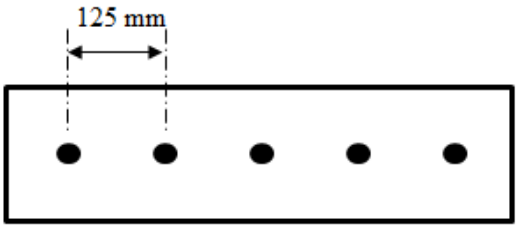

Figure 4.18: Schematic showing position of thermocouples

The temperature controlled circulating bath supplied the heat transfer fluid to the inlet port of the hot slab, the fluid from the exit port of the hot side was then passed through a fan heat exchanger. The cooler fluid from the fan heat exchanger was then supplied to the inlet port of the cold side. This arrangement was done to eliminate duplication of equipment (which could be an additional source of error) and ease of measurement arising from a constant mass flow rate at both sides. A schematic of this is shown in Figure 4.19 while the actual apparatus can be seen in Figure 4.20.

The mass flow rate ($\dot{m}$) was measured using a Coriolis mass flow meter and a differential pressure sensor was connected to the inlet and exit port of the hot side to measure the pressure drop (Δp). All the measured quantities were logged with a 16-bit National Instruments data acquisition system via Labview. At a given flow rate, the temperatures reached steady state after approximately 10–15 minutes. Enthalpy

change of the fluid at both sides were used to calculate the heat flux out of and in to the fluid at the hot side and cold side respectively, the difference in heat flux at both sides was less than 5 % which can be attributed to heat loss.

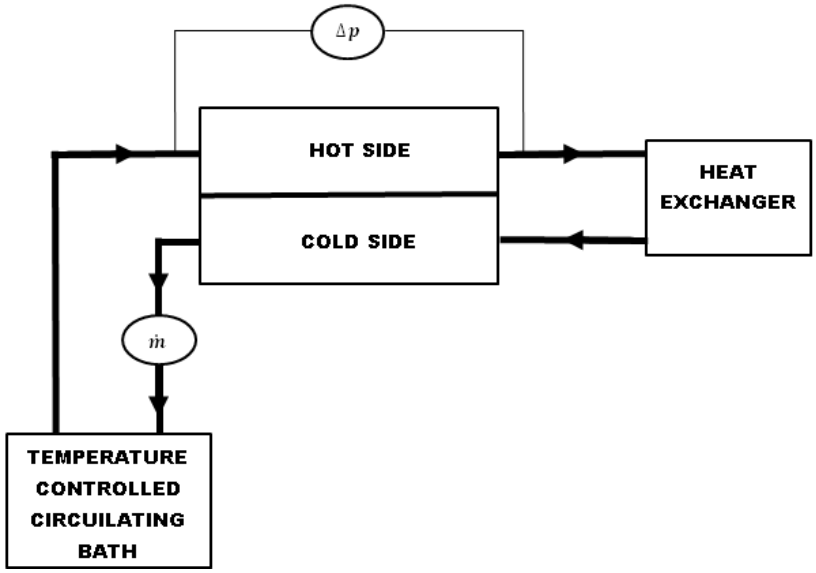

Figure 4.19: schematic of counter flow heat exchanger

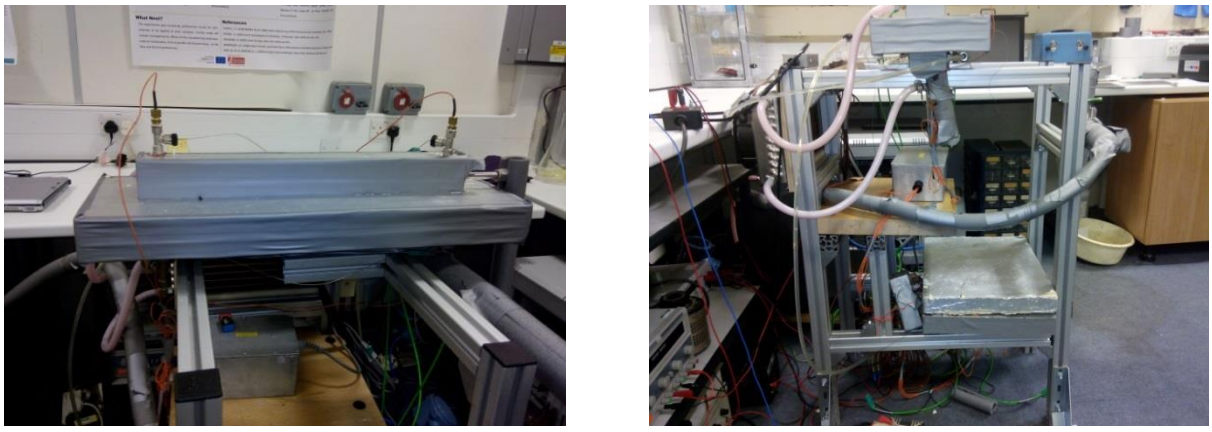

Figure 4.20: The counter flow heat exchanger test rig (a) side view (b) end view

A picture of the micro-channel plate can be seen in Figure 4.21. Relevant design considerations and calibrations outlined in sub – section 4.2.2 were applied to this

test rig also. This counter flow heat exchanger was connected in parallel with the heated sandwich test rig. Two valves(2-way) were used to switch flow between the two test rigs. The whole arrangement can be seen in Figure 4.20b.

Figure 4.21: Micro – channel plate for counter – flow heat exchanger

4.3.2 Data Reduction

4.3.2.1 Mean Slab temperature

The mean temperature of the slab on the hot side was estimated by

$$T_{sh} = \frac{T_{sh1} + T_{sh2} + T_{sh3} + T_{sh4} + T_{sh5}}{5} \tag{4.27}$$

The mean temperature of the slab on the cold side was estimated by

$$T_{sc} = \frac{T_{sc1} + T_{sc2} + T_{sc3} + T_{sc4} + T_{sc5}}{5} \tag{4.28}$$

4.3.2.2 Mean fluid temperature

The mean fluid temperatures at both sides were estimated by taking the average of the fluid temperature at inlet and outlet. The mean fluid temperature at the hot side was estimated by

$$T_{hf} = \frac{T_{hin} + T_{hout}}{2} \tag{4.29}$$

The mean fluid temperature at the cold side was estimated by

$$T_{cf} = \frac{T_{cin} + T_{cout}}{2} \tag{4.30}$$

The thermo physical properties of the fluid such as specific heat capacity, thermal conductivity and dynamic viscosity, were estimated with the mean fluid temperature at the cold side.

4.3.2.3 Log mean Temperature difference

The log mean temperature difference which is used for heat exchanger calculations was estimated by

$$\Delta T_{LM} = \frac{\left(T_{hin} - T_{cout}\right) - \left(T_{hout} - T_{cin}\right)}{\log\left(\frac{T_{hin} - T_{cout}}{T_{hout} - T_{cin}}\right)} \tag{4.31}$$

4.3.2.4 Heat flux

The heat flux from the hot fluid to the micro-channel plate was estimated by

$$Q_{hf} = \dot{m} c_{ph} \left(T_{hin} - T_{hout}\right) \tag{4.32}$$

The heat flux from the micro-channel plate to the cold fluid was estimated by

$$Q_{cf} = \dot{m} c_{pc} \left(T_{cin} - T_{cout} \right) \tag{4.33}$$

The heat flux into the cold fluid was used as the heat flux for estimating other parameters.

4.3.2.5 Surface Area

The surface area available for heat transfer is calculated from

$$S_c = 2N_c L(a+b) \tag{4.34}$$

4.3.2.6 Heat transfer coefficient

The overall heat transfer coefficient of a heat exchanger is given by

$$H = \frac{Q_{cf}}{S_c \Delta T_{LM}} \tag{4.35}$$

And the heat transfer coefficient was estimated by

$$h = 2H \tag{4.36}$$

Details of other parameters estimated from the measured quantities are presented in subsequent sections.

4.3.2.7 Pumping power per collector area

The pump power required per plate was estimated by

$$\dot{w} = \left(\frac{\dot{m}}{A_p} \right) \frac{\Delta p}{\rho} \tag{4.37}$$

4.4 Measuring Instruments and Equipment

This section discusses the various instruments and equipment used in the experimental facilities as well as the techniques adopted to ensure accurate measurements were obtained.

4.4.1 Thermocouples

Thermocouples were used as the main instruments for measuring temperatures. Most of the quantities were measured with type T (copper constantan) thermocouples. Applied sensor technologies (AST) recommends this thermocouple type for use in in mildly oxidising atmospheres and applications where moisture is present (AST, 2014). The copper constantan alloy is also suitable for these low temperature measurements since the homogeneity of the component wires can be maintained better than with other base metal wires. Therefore, errors due to material variation within wires in zones of temperature gradients are greatly reduced (AST, 2014). A few type K thermocouples were used randomly for validation. Diameter of thermocouples ranged from 0.25mm to 1mm, depending on the location.

4.4.1.1 Calibration

The main parameters needed to be estimated from temperature measurements are mostly functions of a difference in temperature rather than the absolute temperature measurement. Therefore, it was imperative to ensure high precision of all thermocouples. This was achieved by using the calibration function of the Data Acquisition (DAQ) system. The function calibrates all the selected channels thereby

compensating for the inaccuracies in the whole measurement system. All the thermocouples to be used were bonded together, put in the bath and calibrated at a number of temperatures (0 -100 °C) to match bath temperature readout. Figure 4.22a shows a picture of the bonded thermocouples in the bath. A handheld thermometer and a temperature calibration kit (shown Figure 4.22b) were used to confirm accuracy of bath read out.

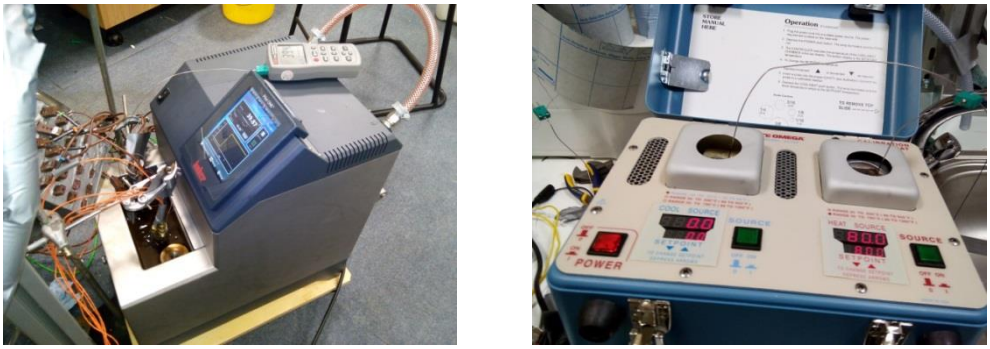

Figure 4.22: (a) Thermocouples in bath (b) Calibration Kit

Figure 4.23 shows a plot of the temperature readings before and after calibration. A difference of up to ± 0.35 °C can be observed before calibration, this reduces to less than ±0.06 °C after calibration; this difference was consistent at various temperatures and several experiments. It was therefore adopted as the uncertainty in thermocouple measurement. Table 4.4 shows the standard deviation, variance and 95% confidence level (Student t's) of 100 measurements from 14 thermocouples.

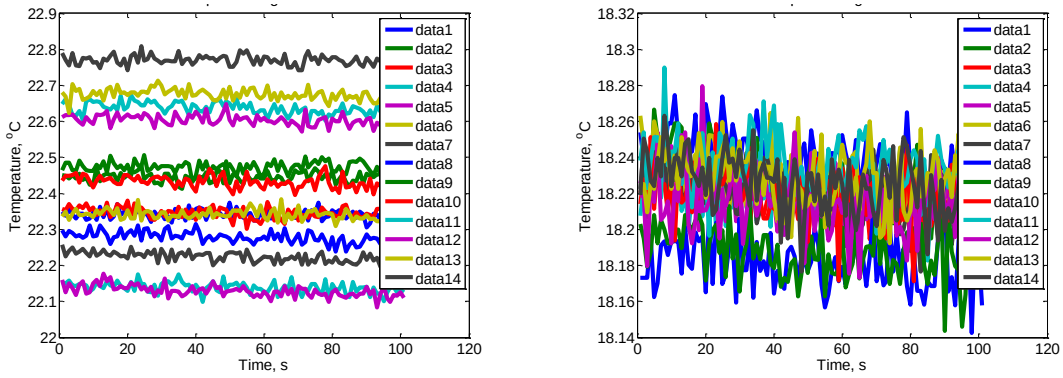

Figure 4.23: Thermocouple reading (a) before and (b) after calibration

Table 4.4: Statistical Analysis on thermocouple readings $\times 10^{-3}, ^{\circ}C$

TC	1	2	3	4	5	6	7	8	9	10	11	12	13	14
σ,	14.1	14.3	13.2	13.3	14.8	15.0	14.4	14.6	14.3	14.3	15.5	16.5	13.8	16.2
σ^2	2.0	2.0	1.8	1.8	2.2	2.2	2.1	2.1	2.0	2.0	2.4	2.7	1.9	2.6
Δ_{95}	28.1	28.4	26.3	26.4	29.5	29.8	28.6	29.0	28.4	28.4	30.8	32.9	27.5	32.3

4.4.2 Resistance Temperature Detectors (RTDs)

The experimental facility was initially designed to utilise Platinum (PT100) Resistance Temperature Detectors (RTDs) as primary temperature probes. However, this proved difficult due to the size of the RTDs; the smallest available RTD off the shelf, had diameter of 3 mm. For example, the RTDs measuring the plate temperature were inserted in a groove in the top slab which implies that the readings from the RTD could be a temperature at the interface or the top slab temperature. However, RTDs which were placed inside fluid/entry/exit ports proved to be highly valuable as they confirmed fluid temperatures.

A signal converter module (shown in Figure 4.24) was designed and built. This module was used to supply excitation current to the RTDs as well as convert the output current to the standard 4 – 20 mA output signal. The output signal from each RTD was conducted through a 250Ω precision resistors and the voltage (1-5 V)

across each resistor was logged by the DAQ. These voltages were converted to temperature via a linear scale in the scale function of measurement and automation explorer (MAX) software in the NI DAQ. Further details of the module are presented in Table 4.5. The RTDs were calibrated in the same way as the thermocouples and a similar variation was observed.

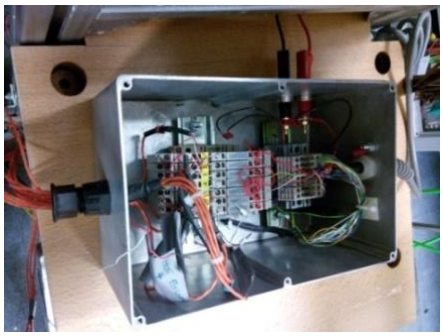

Figure 4.24: RTD signal converter module

Table 4.5: Details of RTD signal converter module

Output into 750Ω @ 24V	**4 - 20mA**
Temperature range	-50°C – 150°C
Power Supply Voltage	9-30Vdc
Transmission Error	typ. 0.2% max. 0.5% V. FSR
Linearity	< 0.1% V. FSR
Supply Current/RTD	0.8mA
Ambient Temperature	0 to +50°C
Resistor	250Ω

4.4.3 Coriolis Mass Flowmeter

A CM025 Coriolis mass flowmeter was used to measure the mass flow rate. This instrument uses the Coriolis principle to simultaneously but independently measure mass flow rate and density. The accuracy of mass flowmeter read-out was checked by timing deionised water flow into a measuring cylinder (shown in Figure 4.25a).

Figure 4.25b compares the measured flow rate to the flow meter's display; the curves can be observed to differ by less than 2% .

The voltage output of the mass flowmeter was connected to the DAQ and a linear scale, which converts voltage to grams per second (g/s), was created in MAX and assigned to this channel. This channel was then calibrated to match the display read-out of the mass flowmeter. Figure 4.26 shows the mass flow rate logged continuously for 500 seconds; a variation of about ± 0.06 g/s can be observed indicating a high level of precision.

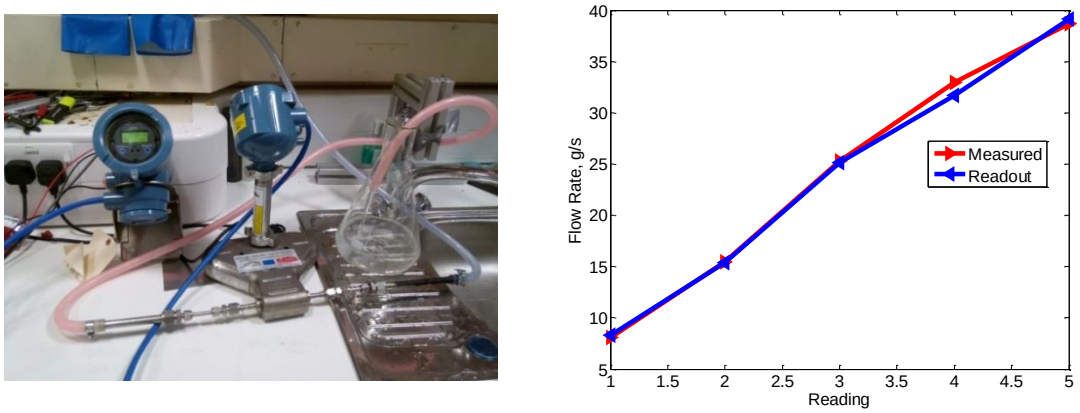

Figure 4.25: verifying accuracy of Coriolis mass flow meter

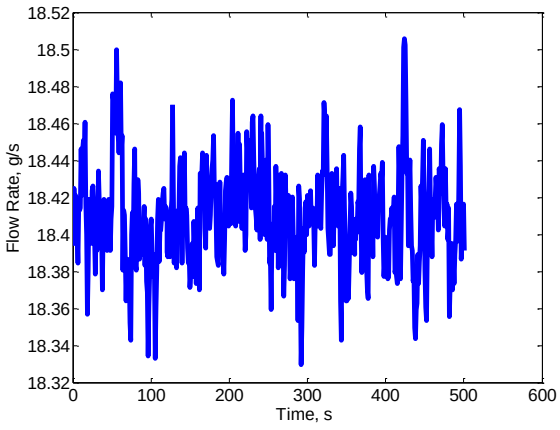

Figure 4.26: Mass flowmeter readings after calibration

4.4.4 Differential pressure transducer

A differential PMP 5023 Pressure Transducer from GE Measurement & Control Solutions (shown in Figure 4.27a) was used to measure the pressure drop across the test section. The pressure transducer was designed to have a full thermal calibration, and a compensated temperature range of -40 °C to +125 °C. The pressure transducer channel was calibrated, as described in the previous sections, to match a hand held manometer. Figure 4.27b shows the differential pressure readings logged over 400 seconds after calibration, an average variation of ±40 Pa can be observed which is small compared to expected pressure drop (which will be in the kPa range).

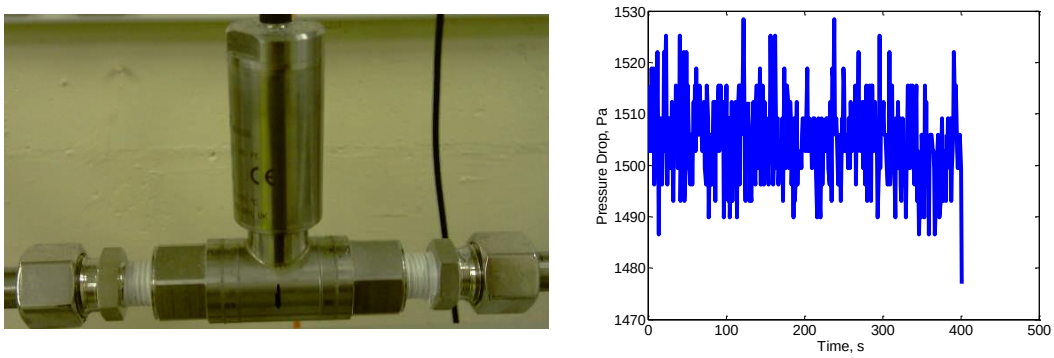

Figure 4.27: (a) Differential Pressure transducer (b) Pressure drop readings after calibration

4.4.5 National Instrument data acquisition system

The signals from the measuring instruments were logged with a NI SCXI DAQ system. This system included several 32 channel SCXI-1303 terminal blocks (shown in Figure 4.28b) to which the measuring instruments were connected. These terminal blocks include isothermal construction that minimizes errors caused by thermal gradients between terminals and the cold-junction sensor. They also include circuitry

for open-thermocouple detection as well as automatic ground referencing for floating (non- grounded) thermocouples. The terminal block was connected to a NI SCXI-1102 thermocouple/voltage input module (shown in Figure 4.28a). These modules are designed for high-accuracy thermocouple measurements but can also acquire millivolt, volt, 0 to 20 mA, and 4 to 20 mA current input signals. Each input channel includes an instrumentation amplifier and a 2 Hz low pass filter. Analog input channels can be scanned at rates up to 333 kS/s (3 µs per channel) (NI, 2014). Two of these modules were connected to a NI PXI 1052 chassis and a NI 8352 controller was used. Graphical programs were written in Labview to write all measurements to file.

Figure 4.28: (a) SCXI-1102 Voltage input module (b) SCXI-1303 Terminal Block

4.4.6 Circulating Bath

A Huber ministat 240cc bath (shown in Figure 4.22a) was used to supply the heat transfer fluid at constant temperature and flow rate to the test rig. A summary of the technical details of the temperature controlled circulating bath is presented in Table 4.6.

Two heat transfer fluids were used during the course of the experiments; distilled water and Tyfocor® LS, a propylene glycol-based heat transfer fluid for solar

collectors. Using two fluids allowed for a wider range of fluid properties variation to be studied. Also, using Tyfocor LS further strengthened the comparability of the test to real life operation. The relevant properties of Tyfocor are presented in

Table 4.7

Table 4.6: Details of circulating Bath

Technical Data	
Operating temperature	-40 to 200 °C
Heating power	2 kW
Cooling power 0-80 °C	0.55 kW
Pressure pump max delivery	27 l/min
Delivery pressure (head)	0.7 bar
Max delivery (suction)	20 l/min
Delivery suction (head)	0.4 bar
Max permissible kinematic viscosity	50 mm^2/s
Bath Volume	4.9 l

Table 4.7: Properties of Tyfocor

Temp °C	**Density Kg/m^3**	**Viscosity mm^2/s**	**Specific Heat KJ/Kg °C**	**Thermal Conductivity W/m °C**	**Prandtl Number**
0	1044	15	3.52	0.4	137.81
10	1040	8	3.55	0.406	72.75
20	1033	5	3.6	0.413	45.02
30	1028	3.5	3.64	0.42	31.18
40	1022	2.5	3.68	0.428	21.97
50	1015	1.95	3.72	0.434	16.97
60	1008	1.7	3.76	0.441	14.61
70	1001	1.4	3.8	0.449	11.86
80	994	1.1	3.84	0.455	9.23

4.4.7 Statistical Analysis

The standard deviation, variance and 95% confidence level (Student t's) of 100 measurements from each instrument were estimated. In the case of thermocouples,

the mean of 200 measurements of each thermocouple were taken and then the mean of all the thermocouple mean temperatures was used. The same was done for the RTDs. Equations (4.38)-(4.40) (Holman, 2012), show the relation for these parameters and their corresponding values are presented in Table 4.8.

Standard deviation,

$$\sigma = \left(\frac{1}{n-1} \sum_{i=1}^{n} \left(x_i - \overline{x} \right)^2 \right)^{\frac{1}{2}} \tag{4.38}$$

Variance,

$$\sigma^2 = \left(\frac{1}{n-1} \sum_{i=1}^{n} \left(x_i - \overline{x} \right)^2 \right) \tag{4.39}$$

Confidence level,

$$\Delta = \frac{t\sigma}{\sqrt{n}} \tag{4.40}$$

Where

$$t = \frac{\overline{x} - X}{\sigma} \sqrt{n} \tag{4.41}$$

Table 4.8: Statistical parameters of measured instrument

Parameter	Thermocouples (°C)	RTDs (°C)	Flowmeter (g/s)	Pressure transducer (Pa)
Standard Deviation	0.016331	0.016331	0.032	8.37
variance	0.000267	0.000267	0.001	70.13
95% confidence Level	0.009428	0.009428	0.006	1.67

4.4.8 Uncertainty

The uncertainty in each instrument has been presented above. Uncertainties in geometric parameters were estimated using high precision measuring instruments as well as manufacturers' specifications. Table 4.9 shows the uncertainty in the relevant measured and geometric quantities assuming that the deviations in each term were uncorrelated. The uncertainty in parameters calculated from measured and geometric quantities were estimated by equations (4.42) – (4.45) (Holman, 2012).

For a product function of the form

$$R = x_1^{a_1} x_2^{a_2} \ldots x_n^{a_n} \tag{4.42}$$

The uncertainty was estimated as

$$\frac{\omega_R}{R} = \left[\sum \left(\frac{a_i \omega_{xi}}{x_i} \right)^2 \right]^{1/2} \tag{4.43}$$

While for an additive function of the form

$$R = a_1 x_1 + a_2 x_2 + \ldots a_n x_n = \sum a_i x_i \tag{4.44}$$

The uncertainty was estimated as

$$\omega_R = \left[\sum \left(a_i \omega_{xi} \right)^2 \right]^{1/2} \tag{4.45}$$

Equation (4.43) and (4.45) can be combined in functions which are both additive and product.

For example, equation (4.46) was used to estimate the uncertainty in the heat transfer coefficient. Figures showing error bounds on various parameters will be presented in chapter 8.

$$\omega_h = h\left[\left(\frac{\omega_Q}{Q}\right)^2 + \left(\frac{\omega_A}{A}\right)^2 + \left(\frac{\omega_{\Delta T_{pf}}}{\Delta T_{pf}}\right)^2\right]^{1/2} \tag{4.46}$$

Table 4.9: Uncertainties in measurement

S/No	Parameter	Uncertainty
1	*a, b,L*	±0.025mm
2	D_h	±0. 055 mm
3	*S*	±1145 mm^2
4	*Ac*	±0.05 mm
4	T_{in}, T_{out} , T_{pi}	±0.06°C
6	$\dot{m}$	±0.15 g/s
7	***ΔP***	±15 Pa

4.5 Summary

This chapter has presented a detailed description of the two experimental test rigs (the heated sandwich and the counter – flow heat exchanger) designed to investigate heat transfer and fluid flow in micro-channel absorber plates. It discusses the various design considerations as well as the evolution of the experiment. Details of the various instruments and equipment used were discussed and procedures undertaken to ensure accuracy, precision and repeatability of experimental data were outlined.

5. Numerical Analysis

5.1 Background

Several studies focused on heat transfer and fluid flow in micro-channels have highlighted the importance of carrying out numerical investigation in conjunction with experimental studies. For example, Rosa et al. (2009), in a comprehensive review of heat transfer and fluid flow in micro-channels, noted that for the case of heat exchangers with parallel micro-channels or when scaling effects are significant, correlations may only give a gross estimation of the Nusselt number hence suitable numerical simulations are necessary. Gamrat et al. (2005) stated that numerical modelling may be a very helpful tool to interpret experimental data, to test assumptions and may be also very useful to evaluate the relative importance of the physical phenomena possibly involved in micro-channel heat transfer. Fedorov and Viskanta (2000) investigated conjugate heat transfer in a silicon heat sink with rectangular micro-channels. Their numerical and experimental results were in good agreement and they observed very complex heat flow patterns. They further showed that there is a very strong coupling between convection in the fluid and conduction in the silicon substrate that can only be resolved by a detailed three dimensional (3D) simulation. Lee et al. (2005) investigated heat transfer in 10 parallel rectangular micro-channels with hydraulic diameters ranging 0.3 – 0.9 mm and found that that the experimental results disagreed with all of the tested correlations but were well predicted by numerical simulations. This was attributed to the fact that 3D effects in the solid walls and fluid can significantly modify the thermal wall boundary condition in a heat exchanger with parallel channels. They recommended the use of numerical simulations with suitable boundary conditions, instead of correlations, to predict the performance of heat sinks using micro-channels.

In view of these, a 3D numerical simulation seems to be a pertinent part of investigating heat transfer and fluid flow in these micro-channel absorber plates. A numerical simulation has the potential to accurately measure the scaling effects, mal-distribution in the manifolds as well as address the 3D effects in the solid and fluid. Several commercial CFD software tools can be used to achieve this, for example, star CCM, Comsol, Fluent and CFX. This chapter presents details of the methods used in performing 3D numerical simulation on the micro-channel plates using a commercial CFD package - ANSYS CFX.

5.2 ANSYS CFX - Overview and Validation

ANSYS CFX software is a high-performance, general purpose fluid dynamics program that has been applied to solve wide-ranging fluid flow problems for over 20 years (Ansys, 2014). The package uses the Navier–Stokes equations to describe the fundamental processes of momentum, heat, and mass transfer. The solver is highly parallelized and incorporates a number of mathematical models that can be used together with the Navier–Stokes equations to describe other physical or chemical processes such as turbulence, combustion, or radiation thus offering a wide range of physical models to capture virtually any type of phenomena related to fluid flow.

This solver, like most commercial CFD packages, uses a finite volume approach; it integrates the conservation equations (equations (5.1),(5.2) and (5.3)) over all the control volumes in the region of interest i.e. applying a basic conservation law to each control volume.

Continuity

$$\frac{\partial \rho}{\partial t} + \nabla \bullet \left(\rho U_E \right) = 0 \qquad (5.1)$$

Momentum

$$\frac{\partial(\rho U_E)}{\partial t} + \nabla \bullet (\rho U_E \otimes U_E) = -\nabla p + \nabla \bullet \tau + S_M + S_E \qquad (5.2)$$

Energy

$$\frac{\partial \rho h_{Etot}}{\partial t} - \frac{\partial \rho}{\partial t} + \nabla \bullet (\rho U_E h_{Etot}) = \nabla \bullet (k \nabla T) + \nabla \bullet (U_E \bullet \tau) + U_E \bullet S_M + S_E \quad (5.3)$$

Where

$$\tau = \mu \left(\nabla U_E + (\nabla U_E)^T - \frac{2}{3} \delta \nabla \bullet U_E \right) \qquad h_{Etot} = h_E + \frac{1}{2} U^2$$

The integral equations are then converted to a system of algebraic equations by generating a set of approximations for the terms in the integral equations (Ansys, 2010b). The algebraic equations are solved iteratively (because of the non-linear nature of the equations), until it converges (approaches the exact solution). One of the most important features of CFX is that it uses a coupled solver, which solves the fluid flow and pressure as a single system and faster than the segregated solver up to a certain number of control volumes as it requires fewer iterations to achieve equally converged solutions (Qi et al., 2010).

This study is focussed on heat transfer and fluid flow therefore, a thermal energy model, which solves the energy transport equation, was used. The thermal energy model for the fluid is shown in equation (5.4), this model neglects variable density effects, however it is appropriate for the analysis as it is recommended for low speed liquid flows (Ansys, 2010b). The model for heat transfer in the solid domain is presented in equation(5.5).

$$\underbrace{\frac{\partial \rho h_{Etot}}{\partial t} - \frac{\partial \rho}{\partial t}}_{Transient} + \underbrace{\nabla \bullet \left(\rho U_E h_{Etot}\right)}_{Convection} = \underbrace{\nabla \bullet \left(k \nabla T\right)}_{Conduction} + \underbrace{\nabla \bullet \left(U_E \bullet \tau\right)}_{viscouswork} + \underbrace{S_E}_{Sources} \quad (5.4)$$

$$\underbrace{\frac{\partial \left(\rho c_p T\right)}{\partial t}}_{Transient} = \underbrace{\nabla \bullet \left(k \nabla T\right)}_{Conduction} + \underbrace{S_E}_{Source} \quad (5.5)$$

As can be expected, this 20 year old solver has been used and validated by many, examples include Sklavounos and Rigas (2004), Frank et al. (2010) and Qi et al. (2010). The validity of using this CFD package for this application was checked by simulating the heated sandwich test rig. The simulation results were then compared to experimental results. The procedure for performing the heated sandwich validation is discussed in detail to illustrate the methods adopted in geometry creation, mesh generation, domain setup, boundary condition and general solver settings.

5.2.1 Heated Sandwich Validation

The software was validated by simulating the heated sandwich experiment. This was done using the Ansys Workbench platform which incorporates the various stages necessary for performing a CFD analysis; these stages are discussed in detail below.

5.2.1.1 Geometry Creation

The first step in a CFD simulation is to create a geometry that adequately represents the physical system to be studied. A geometry representing the heated sandwich test rig was created with Ansys DesignModeller. This geometry consisted of four computational domains within which the equations of fluid flow and heat transfer were solved. The domains are the fluid, micro-channel plate, top slab and bottom

slab. It should be noted that the two domains of interests are the fluid and micro – channel plate; however, the bottom and top slabs were included to have a geometry representing the experimental test rig. Figure 5.1a shows a wireframe of the whole geometry, it can be observed to be an exact replica of the actual test rig. Figure 5.1b shows the isolated fluid domain; it was created by filling the cavity between the micro-channel plate and the bottom slab. This can be seen to adequately represent fluid flow in the channels as well as the manifolds. The dimensions of the channel depth, width and pitch were set as workbench input design parameters to easily match the different plates.

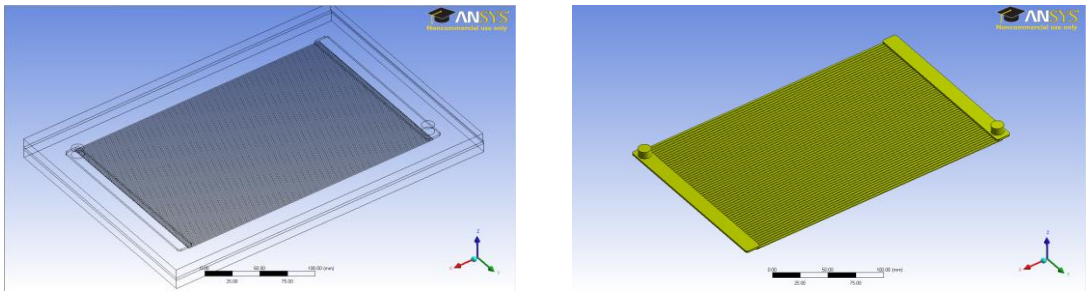

Figure 5.1: (a) Heated sandwich geometry (b) Fluid domain

5.2.1.2 Mesh

The next stage of the analysis is to discretise the domains into a number of small control volumes. This was done using the Ansys meshing program. Due to the small size of channel walls and plate thickness, unstructured grids consisting of tetrahedral, pyramid and prismatic elements, were employed. It is pertinent to carefully choose the mesh size so as to avoid adverse effect on the simulation accuracy, hence the quality of the mesh was checked in two ways. Firstly, mesh-associated parameters such as the edge length ratio, maximum and minimum face angle, connectivity number, and element volume ratio were checked (Ansys, 2010c). Secondly, the

influence of mesh size on the parameters of interest was checked. This was achieved by running simulations with differently refined meshes. It should be noted that the coarseness of the mesh for fluid and plate could not be more than half of the channel depth because the 3D simulation requires at least two mesh layers in a domain. Figure 5.2a shows the effect of the mesh size on the micro-channel plate domain by comparing the micro-channel plate temperature profile at different number of mesh nodes. It can be observed that the four finer meshes show mesh independent solutions (temperature varies by less than 0.1° at any given position) while the coarsest mesh can be observed to have a more significant difference (about 2 °C). The effect of mesh refinement on fluid temperature is shown in Figure 5.2b, the temperature at any given position varies by less than 0.1°C which indicates a mesh independent solution for the fluid.

Table 5.1 gives details of meshes for the various domains; finer meshes were adopted for the domains of most importance (plate and fluid); a magnified and sectioned view the mesh in these domains can be seen in Figure 5.3. The fineness of the mesh was limited to a total of half a million nodes (this is the limit the academic licence available at the institution of study), therefore, the mesh could not be made fine enough to resolve the boundary layer growth on all channels. The mesh on the fluid domain in a few channels was however made very fine, by using various mesh tools and controls. The boundary layer development on these few channels could be resolved and could be used as a representation for all channels. More details of the boundary layer will be given in subsequent discussion chapters.

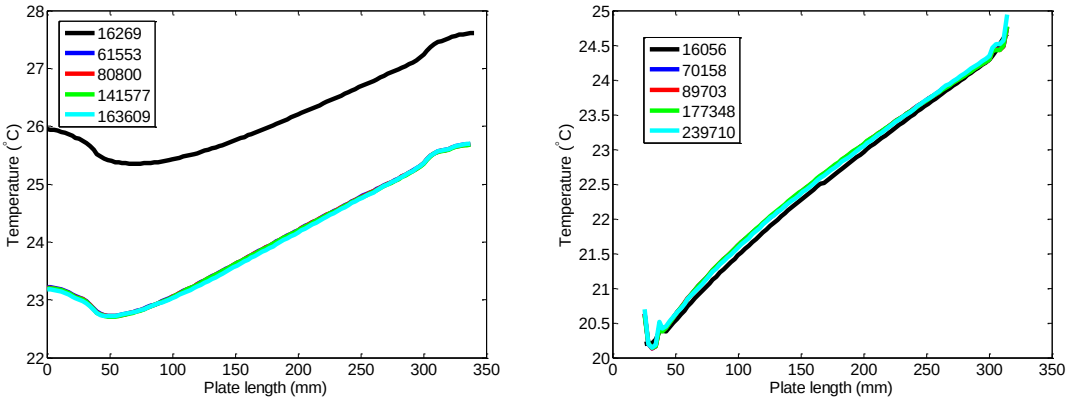

Figure 5.2: Temperature in flow direction at different number of nodes (a) Plate (b) Fluid

Table 5.1: Details of the mesh used

Domain	Nodes	Elements	Body Spacing	Min size	Curvature Normal Angle
Fluid	29968	811786	1.5 mm	0.1 mm	18 ^{o}
MC Plate	163989	654770	0.8 mm	0.1 mm	18 ^{o}
Top Slab	20984	15300	-	0.2 mm	18 ^{o}
Bottom Slab	29968	138149	-	0.2 mm	18 ^{o}
All Domains	454706	1620005			

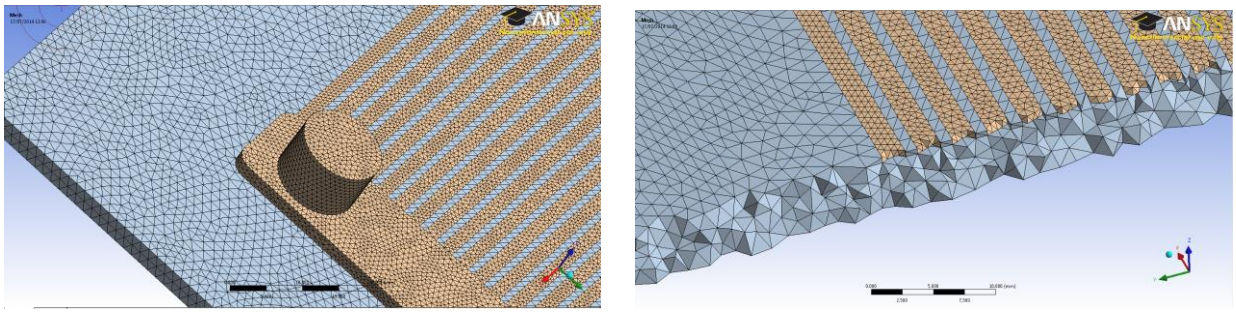

Figure 5.3: A magnified view of the mesh

5.2.1.3 Domain and boundary conditions

The next step of the simulation is to define the properties of the various domains and their corresponding boundary conditions. These were done to match actual experiments as much as possible however, some assumptions were made. These include

I. The flow is laminar and can be approximated as steady state.
II. Incompressible fluid flow.
III. Fluid properties are constant.
IV. Viscous dissipation, radiation and buoyancy are negligible.

The domain definition and corresponding boundary conditions for the four computational domains are discussed below.

(a) Top Slab

The component of the geometry representing the top slab was defined as a solid domain with the material type set to aluminium. Properties of aluminium in the material library were corrected to those for aluminium 6082 alloy; this was the material used to make components of the test rig. The thermal energy option of the heat transfer physical model was selected. The domain initialisation was set to automatic, this option allows CFX-Solver to calculate values for the solved variable at the start of the solution(ANSYS, 2010a).

The boundary conditions were set to represent the various experimental runs. The main boundary condition set for the top slab was the heat flux supplied by the heater mat. This was done by setting the upper face of the top slab to a constant heat flux

boundary condition. To account for thermal losses in the experiment, the value of this was set to the fluid's enthalpy change obtained from the experiment instead of measured electrical power consumed by the heater mat. Expressions for experimental variables were written using the CFX expression language (CEL). These expressions were then set as workbench input parameter which allowed experimental variables to be easily set. The four sides of the top slab were set to adiabatic walls, thereby simulating a perfect insulation at the sides since the thermal losses have been taken into account in the value of heat flux supplied. The lower face of the top slab formed a solid – solid interface with the micro-channel plate; this is discussed further in the interface section below.

(b) Bottom Slab

The bottom slab domain was similar to the top slab hence a similar setup was applied. The sides and lower face of this slab were set to adiabatic walls while the upper face which was in contact with the fluid, was set as a solid – fluid interface. Figure 5.4 is a picture of the geometry highlighting the bottom slab (The geometry is upside down to highlight the bottom slab).

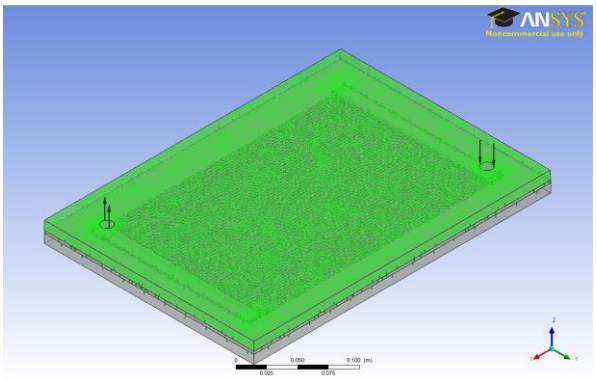

Figure 5.4: The bottom slab domain

(c) Micro-channel plate

The micro-channel plate was also set as a solid 6082 aluminium domain with an automatic domain initialisation. Since the plate was sandwiched between the top and bottom slab, the boundary conditions at the upper and lower faces are as a result of the interface. Details of the various interfaces are discussed in the interface section below. The sides of the micro-channel plate were set to adiabatic walls to indicate no heat loss from the sides.

(d) Fluid

The part of the geometry representing the fluid was set as a fluid domain. The fluid type set corresponded to the fluid used in the experiment to be simulated. Water is already defined in the library however the other fluid used, Tyfocor LS, had to be defined in the material library. The morophology option was set to '*continuous fluid*' and buoyancy model was turned off. The thermal energy option of the heat transfer physical model was selected. This models the transport of enthalpy through the fluid domain and neglects effects of mean flow kinetic energy and is therefore adequate for low speed flows (ANSYS, 2010a). Since all experiments were run at very low flow rates (Re<100), no turbulence model was used i.e. The '*None (laminar)*' option of turbulence model was selected. Combustion and thermal radiation were also set to '*None*'. Domain initialisation was set to '*automatic*' which is recommended for steady state simulation(ANSYS, 2010a).

The face of the fluid at one of the ports (see Figure 5.5) was defined as the inlet boundary with the flow regime set to '*subsonic*' as this corresponds to the regime of flow in the experiments. Since direct and accurate measurements of the mass flow

rates were taken in experiments, the '*Mass Flow Rate'* option of the mass and momentum model was selected and a statistic temperature was set as the heat transfer boundary condition for the inlet fluid. The mass flow rate and inlet fluid temperature are experimental variables, CFX expression language (CEL) expressions were written for these two variables and set as workbench input parameters. The face at the other port was set as the outlet boundary, following the conservation of mass principle; the value of the mass flow rate was set as equal to the mass flow rate at inlet. The other walls of the fluid, which are interfaces, will be discussed in the interface section below.

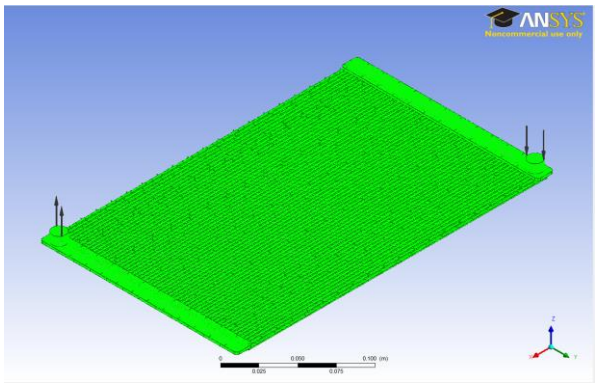

Figure 5.5: The fluid domain

(e) Interfaces

As has been highlighted earlier, the geometry consisted of several interfaces. The main interfaces are discussed here. The first interface of interest is between the top slab and the micro-channel plate. This was defined as a solid – solid interface with heat transfer. The thin material option for the interface material was selected and was defined as air with 0.15 mm interface thickness i.e. measured interface thickness as discussed in chapter 4. Another solid – solid interface with a

conservative heat flux heat transfer model was set between the channel ribs of the micro-channel plate and the bottom slab.

Another interface is between the channel walls and the fluid, the manifolds and the fluid as well as the bottom slab. This was set to a fluid – solid interface. A heat transfer model was enabled to allow for a conjugate heat transfer solution. Figure 5.6 shows the fluid – solid interface between the channels/manifold and the fluid.

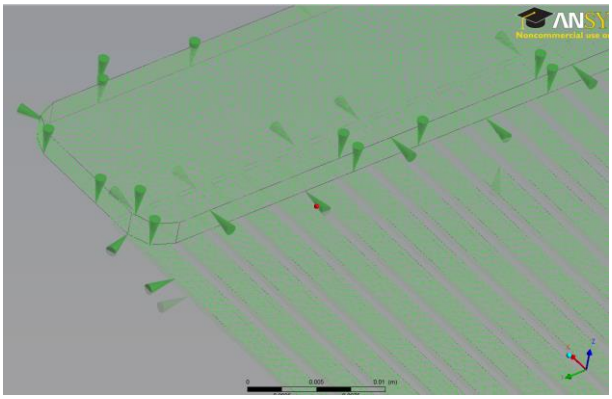

Figure 5.6: The fluid-solid interface

5.2.1.4 Solution

After accurate definition of the domains and boundary conditions, simulations were run to match some of the experimental runs. Some of the precautions taken to ensure accurate solutions include

I. The solution no longer changes with subsequent iterations (checked by increasing the minimum number of iterations for different runs).
II. Overall mass, momentum, energy, and scalar balances are achieved (checked by viewing the solver monitor).
III. Setting the maximum residual to 10^{-6}

IV. Monitoring convergence using residual history.

V. Monitoring other relevant key variables/physical quantities for a confirmation.

One of the advantages of the Ansys Workbench is the interactive post processing GUI that allows results of simulations to be thoroughly investigated. Most of the variables of interest such as heat flux, wall heat transfer coefficient, skin friction and fluid velocity for the whole domain are calculated and written to file. This allows the value of any of these variables at any point in the domain to be estimated. This is illustrated in Figure 5.7, which shows the CFD estimated temperature profile of the micro-channel plate. Temperature measurements can therefore be taken at the same location as temperature probes in the experiment thus making experimental and numerical results more comparable. Expressions and new variables can also be written using the CEL. This was used to define parameters whose experimental and numerical values were to be compared; these variables were set as workbench output parameters. More representative quantities could be measured in CFX post, for example, the average fluid temperature can be estimated as the mass average fluid temperature using the built in mathematical function *MassAve*, the average plate temperature can be estimated as the average temperature at the plate-fluid interface using the built in mathematical function *AreaAve* in conjunction with the 'location' function. It should be noted that the heat transfer coefficient written to file is the wall heat transfer coefficient i.e. the temperature difference between the plate – fluid interface and the adjacent fluid temperature. Therefore, an expression was written to estimate the average heat transfer coefficient from the mass averaged bulk fluid temperature and the average plate wall temperature.

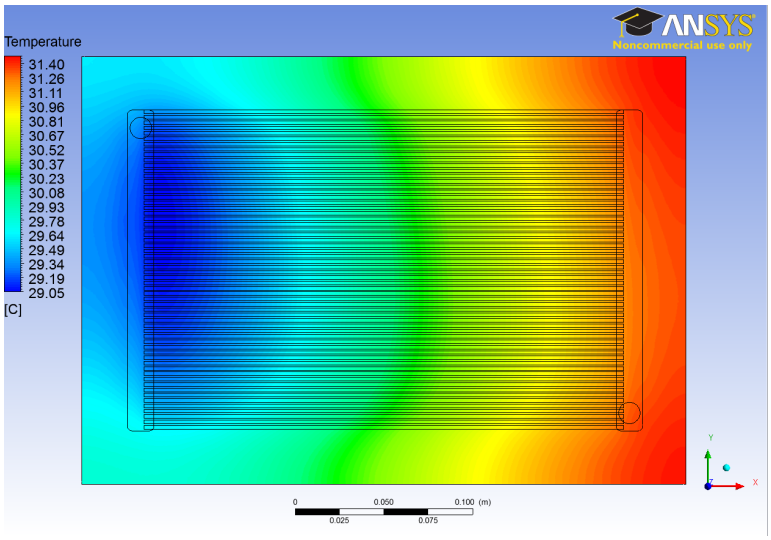

Figure 5.7: Plate temperature at the plate fluid interface

5.2.1.5 Comparing numerical and experimental results

Figure 5.8 shows a graph comparing the experimental and numerical results. Due to the difficulty of experimentally measuring the fluid temperature along the channel (Obot, 2002), only the inlet and outlet fluid temperatures are used. The curve from the numerical simulation intersects both inlet and outlet fluid temperatures suggesting energy is conserved. The simulated plate temperature profile differs slightly from the experimental values, however, the difference is fairly constant signifying that this might be an error resulting from uneven interface thickness in the experimental setup.

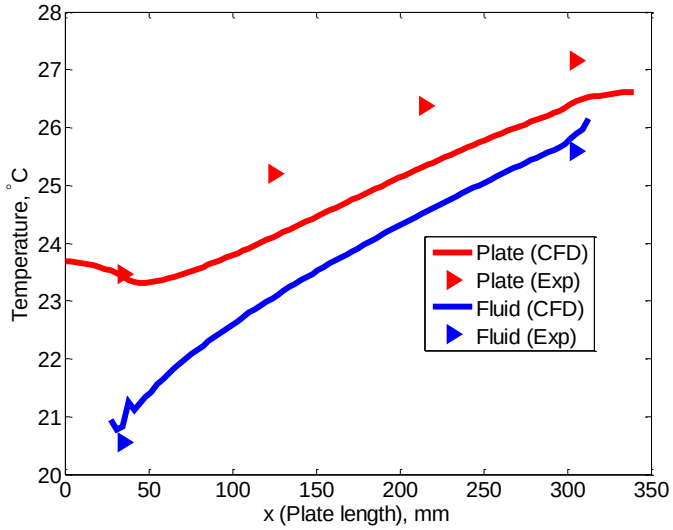

Figure 5.8: Comparing experimental and numerical results

5.3 Summary

This chapter presented an overview of the commercial CFD package, ANSYS CFX, used for numerical analysis. The operation of the program was illustrated by a detailed description of a study to validate experimental results; this highlighted geometry creation, mesh generation as well as the domain and boundary conditions setup. The numerical simulation also produced comparable results to the experiments.

6. Results

6.1 Experimental results

6.1.1 Heated Sandwich

In this test rig, experiments were run at four different inlet fluid temperatures (5°C, 20°C, 40°C and 60°C). For each fluid temperature, seven (7) different mass flow rates were used. This section presents some representative results from the different variations of this test rig.

6.1.1.1 Aluminium Base

Figure 6.1 shows the measured temperature profile from 12 thermocouples on the micro-channel plate. The temperature can be observed to be fairly constant in the transverse direction.

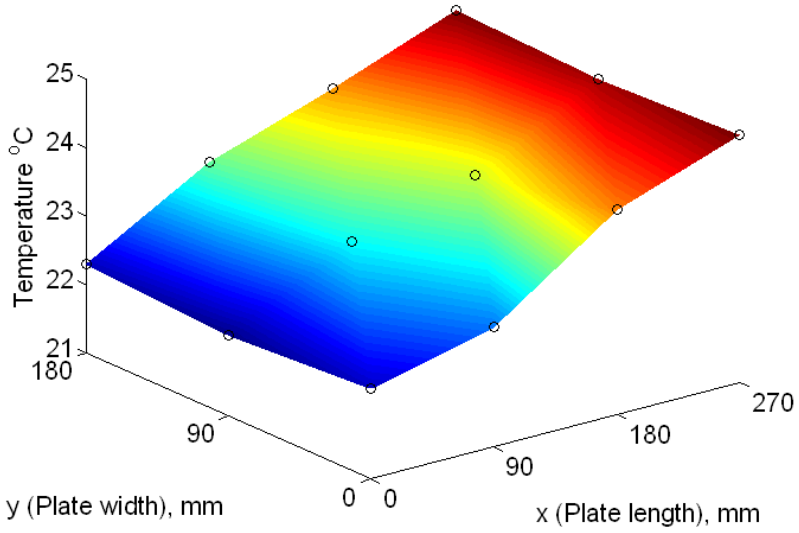

Figure 6.1: Measured temperature distribution in metal plate

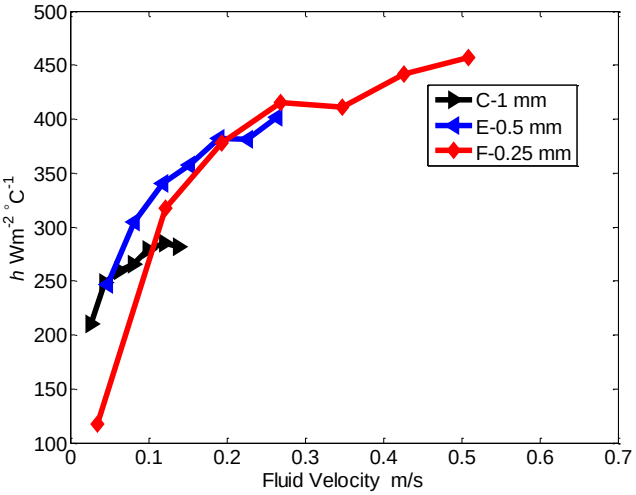

Figure 6.2: Heat transfer coefficient versus fluid velocity

Figure 6.2 shows measured heat transfer coefficients against fluid velocities for three plates with different depths. A strong dependence of heat transfer coefficient on fluid velocity can be observed.

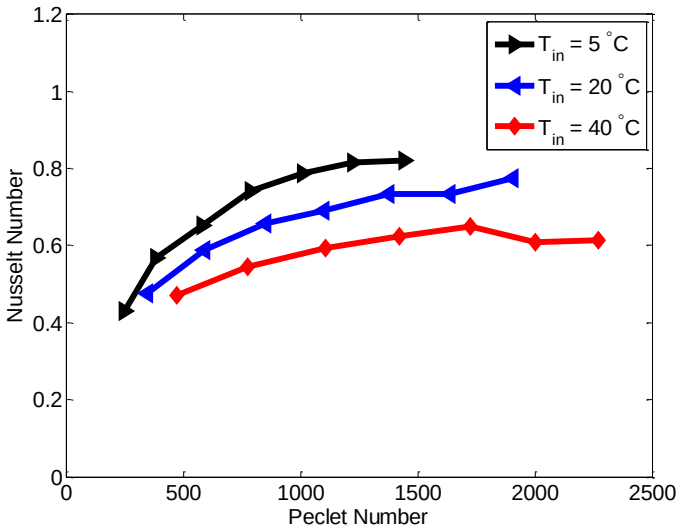

Figure 6.3: Nusselt number versus Peclet number

Figure 6.3 shows the measured Nusselt number as a function of the Peclet number. The data is ploted against the Peclet number because the Prandtl number of Tyfocor

LS varies from about 100 at 5°C to 22 at 40°C. Nusselt numbers for laminar flow through channels with this aspect ratio will be expected to lie between 1.148 and 6.29, depending on the boundary condition. The measured Nusselt numbers are however much lower.

Figure 6.4 shows measured pressure drop against fluid velocity: a linear relationship between velocity and pressure drop is observed, as expected. The three plates have similar pressure drops, in fact, the three curves can be approximated as one.

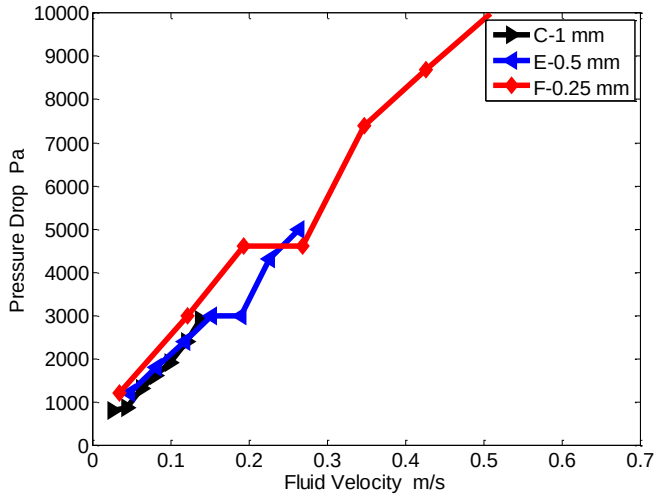

Figure 6.4: Pressure drop versus fluid velocity

Figure 6.5 compares the measured and predicted friction factors; a similar trend of friction factor with Reynolds number can be observed in both predicted and measured values although measured friction factors are slightly lower than predicted values based on numerical Poiseuille numbers for rectangular channels.

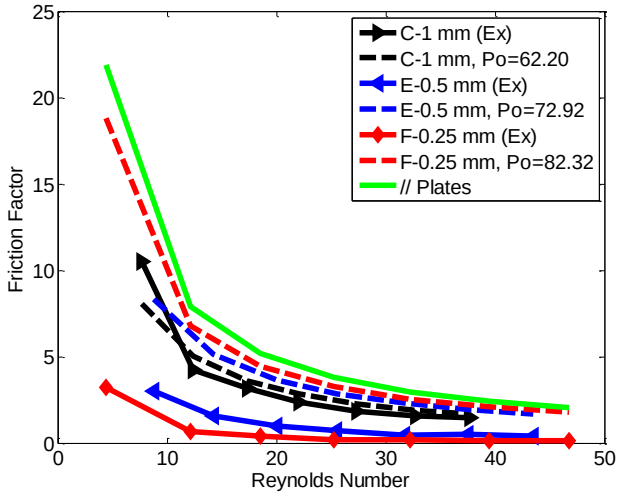

Figure 6.5: Friction factor versus Reynolds number

6.1.1.2 PTFE and Perspex slabs

Figure 6.6 shows a plot of Nusselt number versus Peclet number for experiments with the PTFE slab, the Nusselt numbers in this figure can be observed to be in the the same range as observed previously.

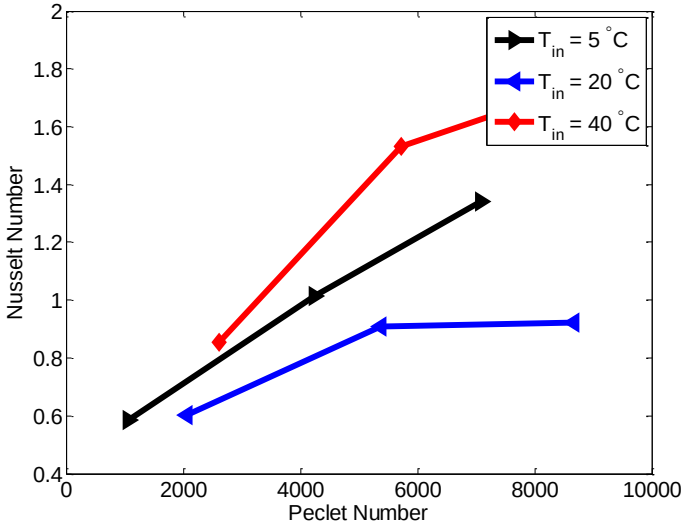

Figure 6.6: Nusselt number versus Peclet number

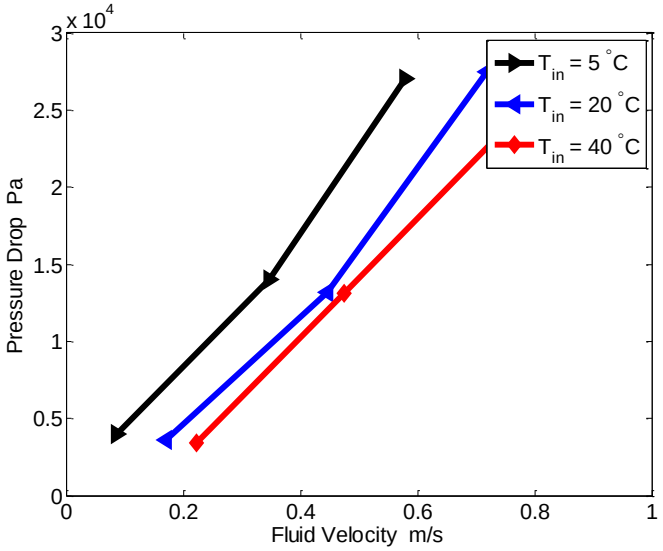

Figure 6.7: Pressure drop versus fluid velocity

Figure 6.7 shows a plot of Pressure drop with fluid velocity for the PTFE base. The pressure drop can be observed to increase with fluid velocity as well as well as viscosity, which are both expected.

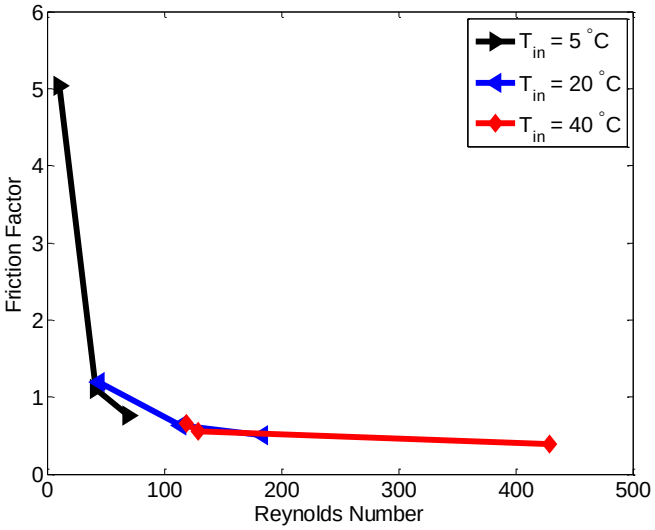

Figure 6.8: Friction factor versus Reynolds number

Figure 6.8 shows a plot of friction factor with Reynolds number. Trends similar to those observed previously can be seen here.

It should be noted that the results from the PTFE test rig were not very useful as the elasticity of the PTFE material caused it to deform resulting in a challenging experiment.

The Perspex base was made primarily for visualising the flow. A fairly even distribution of fluid (coloured to improve visibility) was observed through all channels as opposed to no flow through some channels or flow under the channel ribs.

6.1.2 Counter Flow heat exchanger

In this test rig, experiments were run at three different inlet fluid temperatures (40°C, 60°C and 80°C). Tyfocor and deionised water were used at different runs. The schematic of this test rig was presented in section 4.3; the various temperatures are defined there. For each fluid temperature, at least three (3) different mass flow rates were used. Figure 6.9 shows the temperature profile of the slabs. A concave and convex profile can be observed at the cold and hot side respectively.

Figure 6.10a and Figure 6.10b show plots of heat transfer coefficient against fluid velocity for Tyfocor and deionized water respectively. The heat transfer coefficient shows dependence on fluid velocity in both cases, however, using water produces slightly higher heat transfer coefficients. Similarly, in Figure 6.11, a Reynolds number dependent Nusselt number can be observed. These Nusselt numbers are within 25% of predicted Nusselt numbers for fully developed flow in rectangular channels.

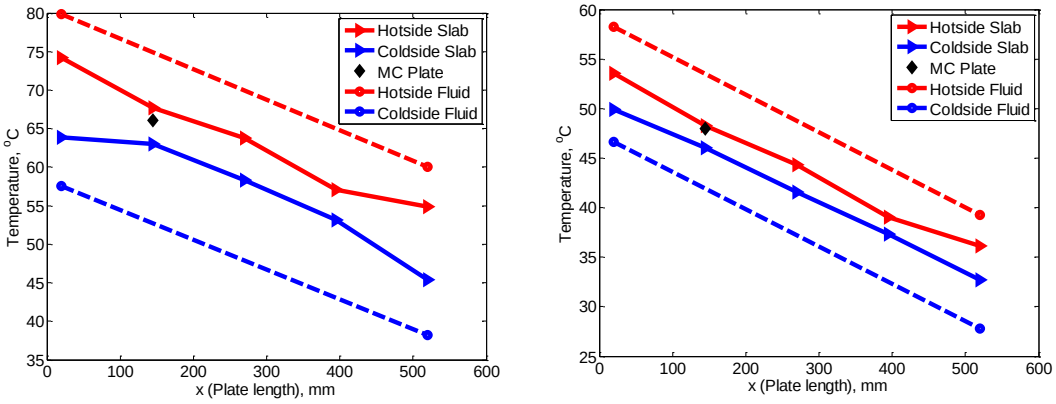

Figure 6.9: Temperature profile on slabs (a) T_{hin} = 80°C (b) T_{hin} =60°C

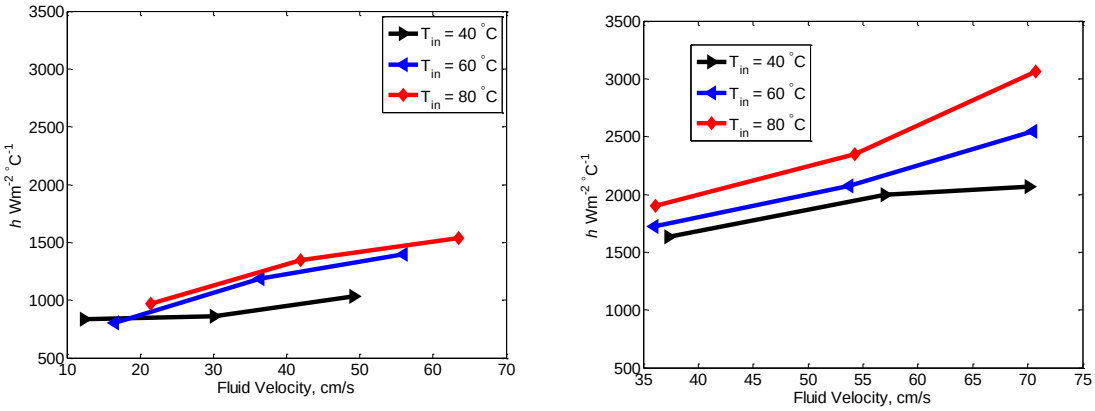

Figure 6.10: Heat transfer coefficient versus fluid velocity (a) Tyfocor (b) Water

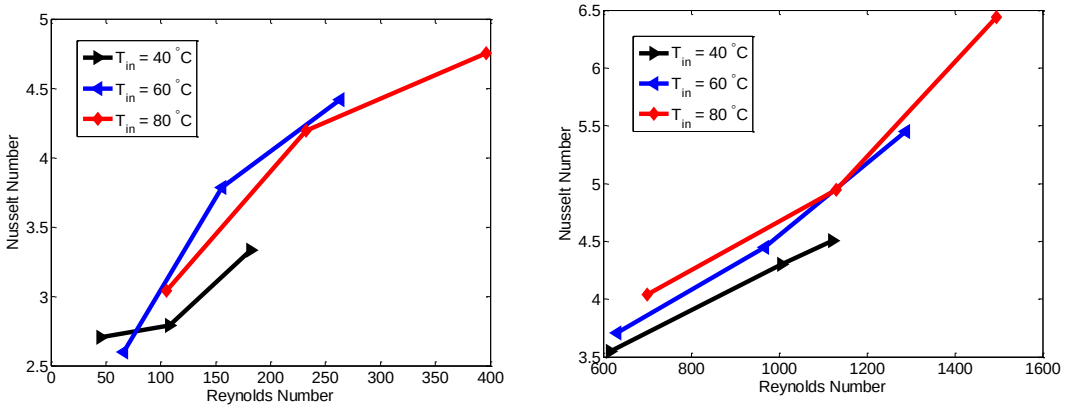

Figure 6.11: Nusselt number versus Reynolds number (a) Tyfocor (b) Water

Figure 6.12 shows the pressure drop as a function of fluid velocity, tyfocor can be observed to have up to four times higher pressure drops compared with water. Also the pressure drop varies with temperature, while experiments using deionized water have similar pressure drops regardless of the fluid temperature. The observations in the experiments with Tyfocor can be attributed to its wide variation of Prandtl numbers with temperature. Figure 6.13 shows plots of friction factors against the Reynolds numbers, a similar trend can be observed at all fluid temperatures.

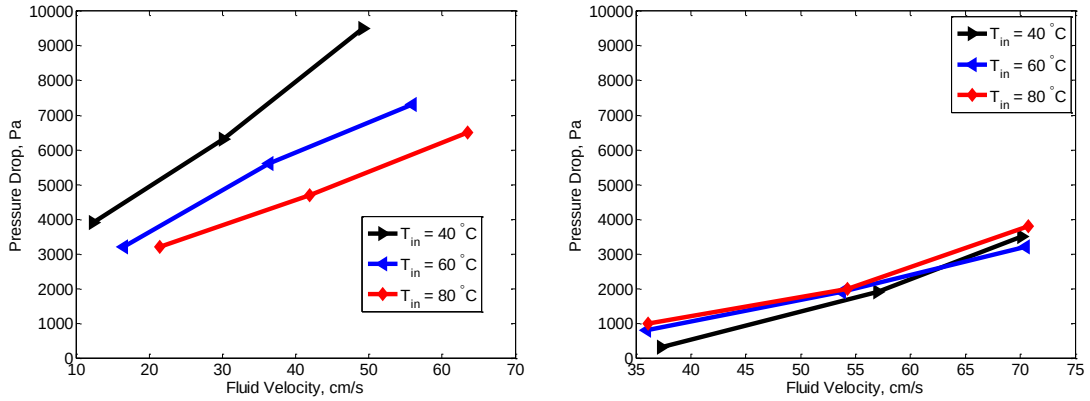

Figure 6.12: Pressure drop versus fluid velocity (a) Tyfocor (b) Water

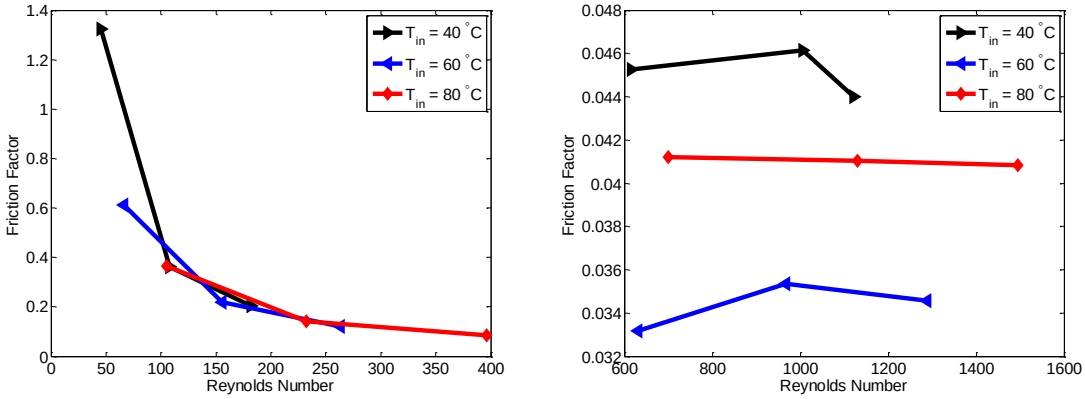

Figure 6.13: Friction factor versus Reynolds number (a) Tyfocor (b) Water

6.2 Numerical Results

Several Numerical simulations were carried out. This section presents some of the results from the Numerical simulation.

6.2.1 Heated Sandwich Simulation

Figure 5.7 shows the temperature profile of the plate at 0.1 mm below the fluid – solid interface. This profile is almost impossible to detect with thermocouples.

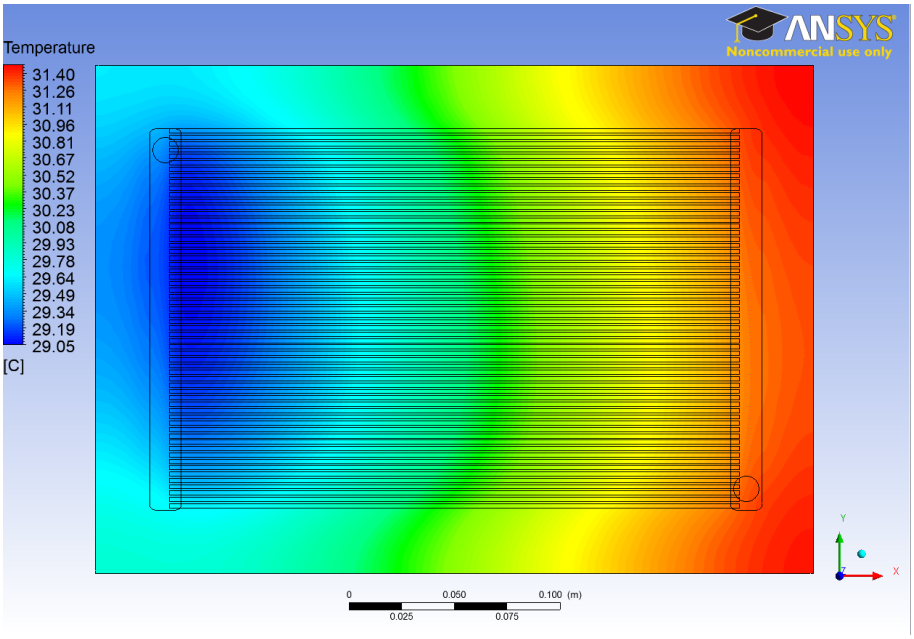

Figure 6.14: Plate temperature at the plate-fluid interface

Figure 6.15 shows the longitudinal temperature profile in 3 selected channels; left (inlet port side – top of Figure 6.14), middle and right (outlet port side – bottom of Figure 6.14). At the channel entry, a difference of about 1°C can be observed between the channel close to the inlet port and that close to the outlet port, this difference reduces in the flow direction becoming less than 0.1°C at the outlet manifold.

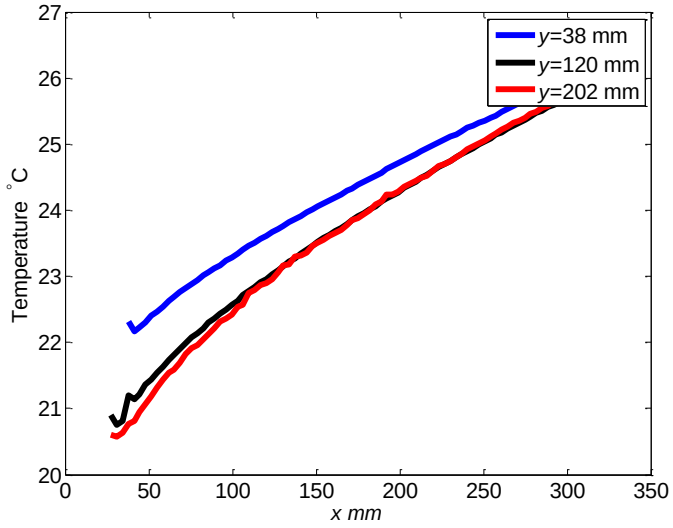

Figure 6.15: Longitudinal fluid temperature profile for 3 channels

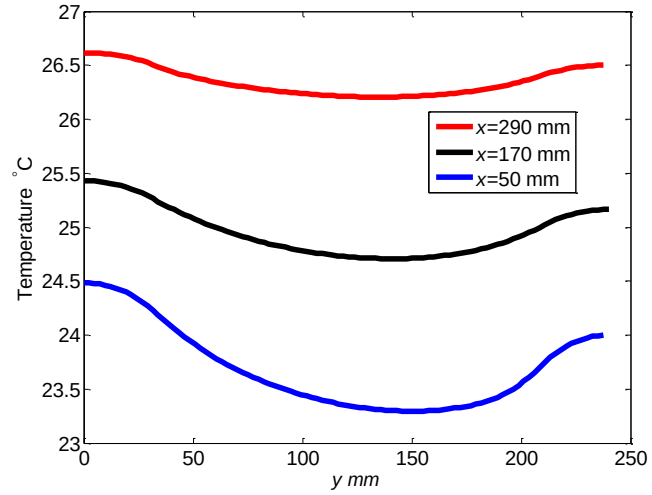

Figure 6.16: Transverse fluid temperature profile at different lengths

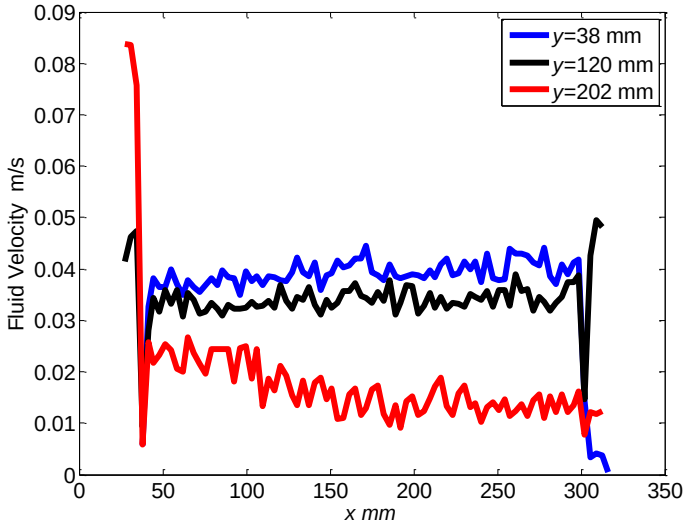

Figure 6.17: Longitudinal velocity profile for 3 channels

Figure 6.16 shows the transverse temperature profile of plate at different lengths, it can be observed that the profile flattens out in the flow direction; with a maximum temperature gradient of 6.3°C/m at the entry and 1.5°C/m at the exit. Figure 6.17 shows the velocity profiles for the three channels selected previously: a large variation in velocity can be observed from channel to channel. It shows that the transverse velocity profile decreases from left to right. A clearer picture of the velocity profiles are shown as contours in Figure 6.18.

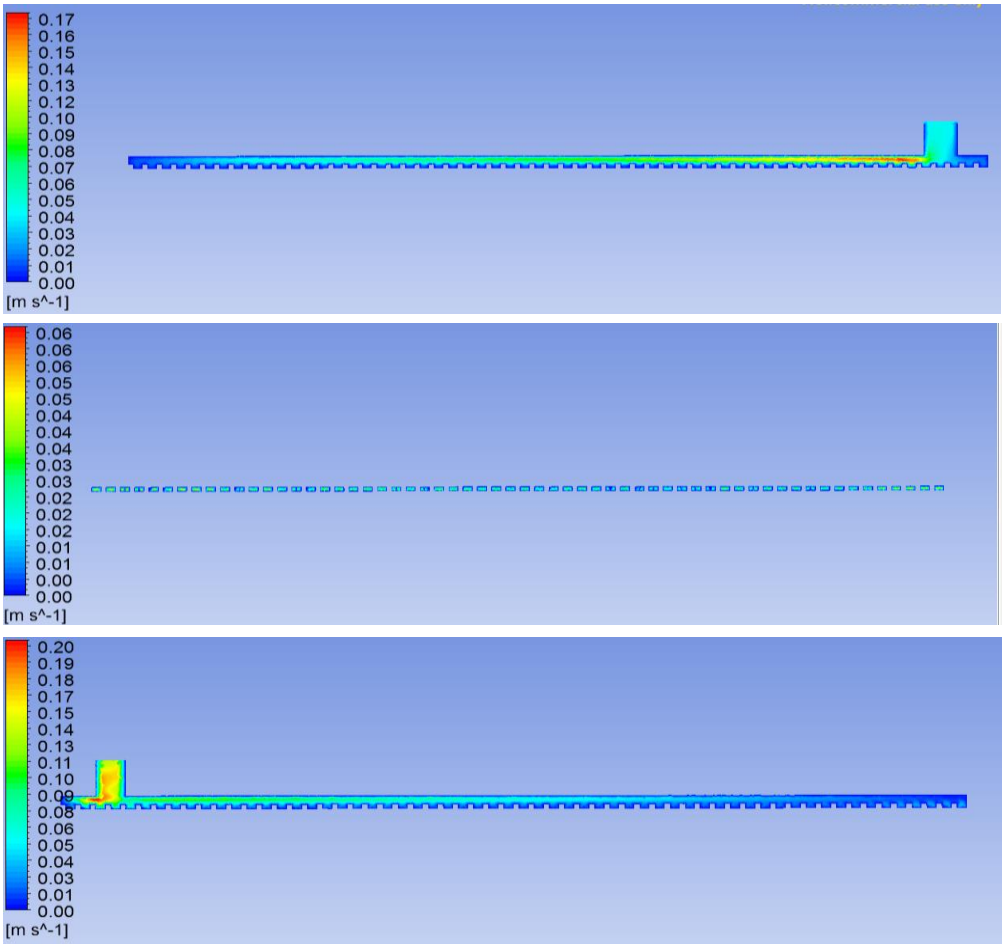

Figure 6.18: Velocity contours at (a) Inlet manifold (b) Middle of channels (c) Outlet manifold

6.2.2 Simplified Model

In addition to the test rig geometry described in Chapter 5, a simplified geometry of the proposed design was created with Ansys DesignModeller. This simplified model was done to be able to perform simulations on finer meshes, because the academic license is limited by the number of nodes. This geometry (shown in Figure 6.19) consisted of three computational domains; the fluid, the micro-channel plate and the cover plate. The results of this simulation are discussed in subsequent chapters.

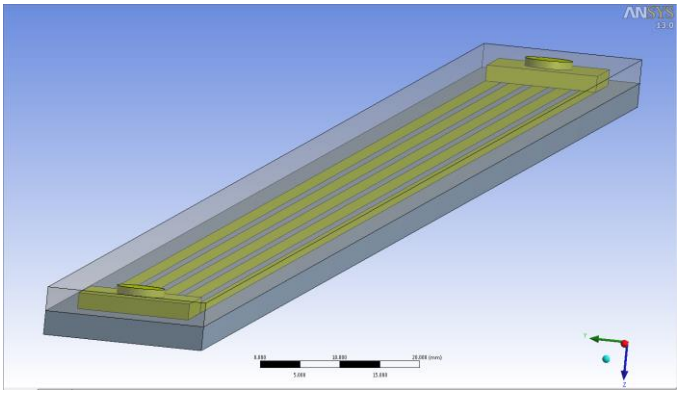

Figure 6.19: CFD geometry

6.3 Comparing Results

The axial temperature profiles of the fluid and plate were chosen as the parameters for comparing results. This is because temperature profile is of significant importance in estimating the overall thermal performance. Direct temperature measurements were also taken at several locations in the experiment.

6.3.1 Analytical and experimental results

Figure 6.20, Figure 6.21 and Figure 6.22 show plots comparing the data points of the heated sandwich experiment with the analytic model presented in Chapter 3. It can be noted that the fluid profile intersects the measured inlet and outlet temperatures and the curve becomes more linear with flow rate. In Figure 6.20, the measured profile matches predicted profile within experimental uncertainty bounds; however, in Figure 6.21 and Figure 6.22, which have higher flow rates, the predicted and measured plate temperature profiles differ. In Figure 6.22, the predicted curve divides the data points into two halves, which indicate a variation in the local heat transfer coefficient in the flow direction. Comparing Figure 6.21 and Figure 6.22

shows that this difference between measured and predicted plate temperature profile increases with flow rate.

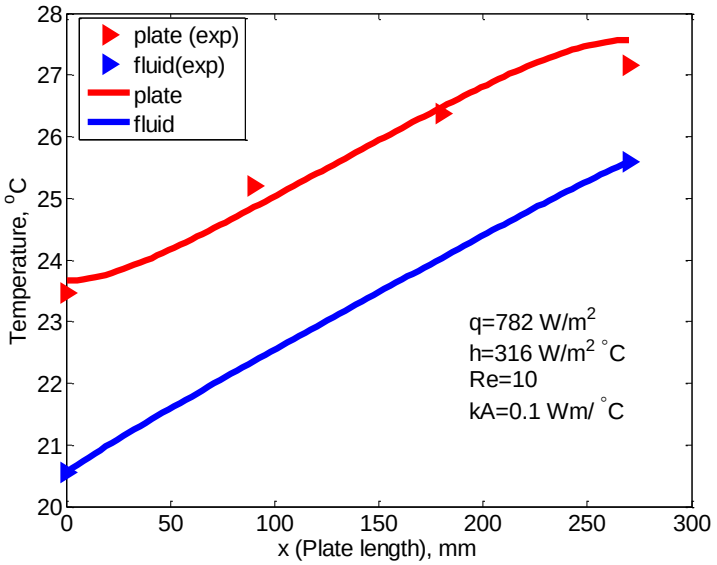

Figure 6.20: Comparing analytic and experimental results (*Re*=10, T_{in}=20.5 °C)

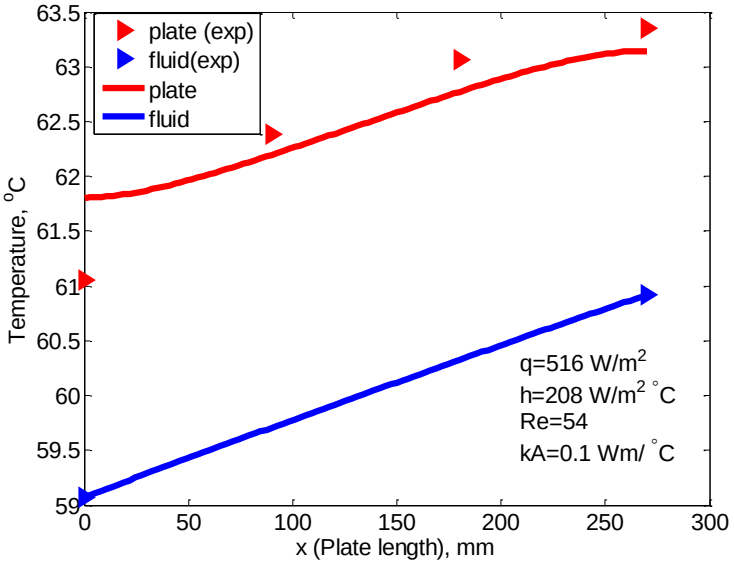

Figure 6.21: Comparing analytic and experimental results (*Re*=54, T_{in}=59 °C)

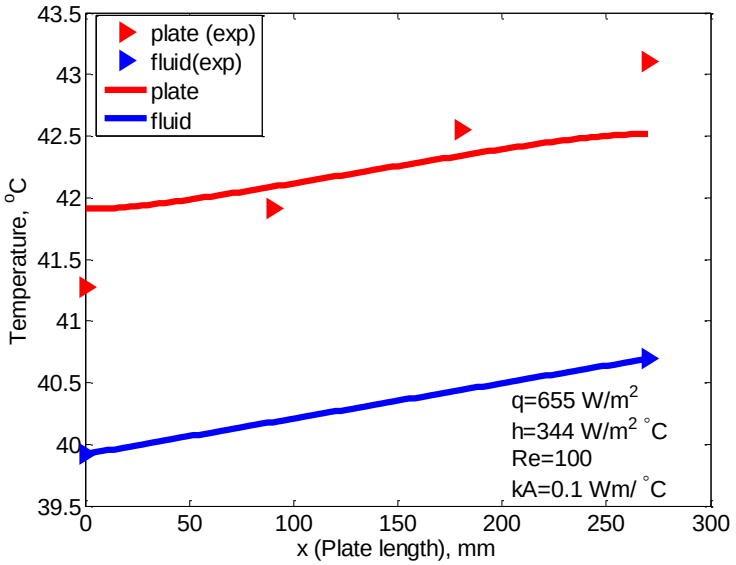

Figure 6.22: Comparing analytic and experimental results (Re=100, T_{in}=40 °C)

6.3.2 Simulation and experimental results

Figure 6.23 compares experimental (heated sandwich) and simulation results as a function of temperature in the flow direction. It can be observed that the simulation curve for the fluid temperature profile intersects experimentally measured inlet and outlet fluid temperatures. This indicates that the conservation of energy principle is satisfied. It should be noted that due to the difficulty of experimentally measuring the fluid temperature along the channel, only the inlet and outlet fluid temperatures are used. Simulated and experimental plate temperature profiles are similar in trend although simulated temperature profile is slightly lower. This difference may be due to the position of the thermocouples in the experiment. The thermocouples in this experiment were at least 2 mm from the liquid/solid interface and slot in between the top slab and micro-channel plate with a fibre-glass adhesive layer between the top

slab and the thermocouple tip. This could have contributed to the slightly higher measured plate temperatures.

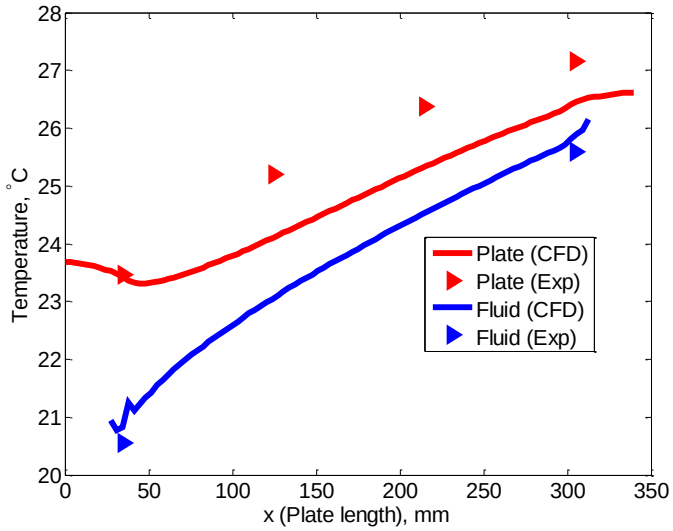

Figure 6.23: Comparing experimental and simulated results

6.3.3 Analytical and simulated results

Figure 6.24 compares the simulated profiles to those predicted by the analytical model. The predictions are based on the average heat flux density as well as heat transfer coefficient from numerical H1 Nusselt number for a channel with aspect ratio of 0.5 and one adiabatic wall (Nu=3.306). The simulated and predicted profile can be observed to match closely although a slight variation can be seen at the inlet and exit. This can be attributed to the mass of fluid in the manifolds; the analytical model only considers flow in the channel.

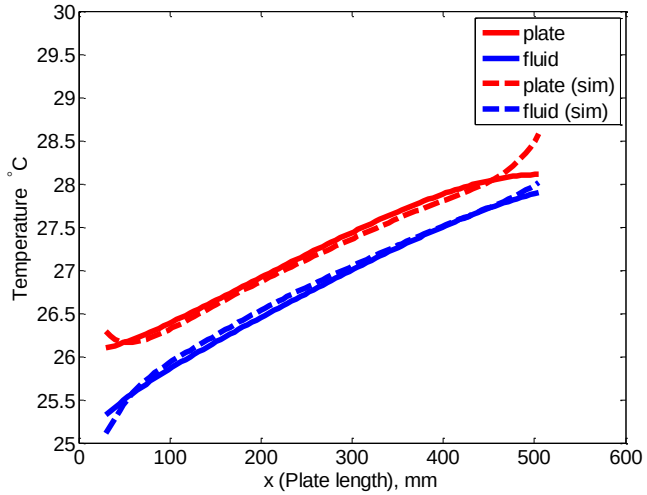

Figure 6.24: Comparing analytical and simulated results

6.4 Summary

This chapter presented representative results of the analytical, experimental and computational analyses. The results from the analytical study were in close agreement with the experimental results, especially for low Reynolds number flows. Similarly, results from the CFD study, using the same design and operating parameters, produced results comparable with experiments. Thermal contact resistance in the experimental setup resulted in a slight difference in measured and computed metal plate temperature profile. A comparison of the analytical and computational results showed almost identical results with the exception of the entry and exit sections.

7. Investigating Geometrical Parameters

7.1 Background

The collector efficiency factor *F'* is a parameter often used to characterise flat plate collectors. *F'* represents the ratio of the useful energy gain to the useful gain that would result if the collector absorbing surface had been at the local fluid temperature (Duffie and Beckman, 2006). Therefore, the convective heat transfer coefficient, *h*, which determines the temperature difference between the absorber plate and the fluid, is a good parameter for characterising the thermal performance of the plates; the higher the heat transfer coefficient, the lower the temperature difference between plate and fluid, the better the thermal performance of the plate. The heat transfer coefficient depends on several factors including fluid properties, fluid velocity, surface roughness and geometry (Çengel et al., 2011, Shah and London, 1978). The performance can be enhanced both at the design (geometry and surface roughness) and operation phases (fluid properties and fluid velocity). This chapter investigates the effects of aspect ratio, surface roughness and manifolds.

7.2 Aspect Ratio

The theory and correlations for heat transfer and fluid flow in conventional sized rectangular channels are well established; constant Nusselt number in the range 0.457 – 8.235, with the exact value depending on the cross sectional geometry and surface boundary conditions, are expected for fully developed laminar flow (Shah and London, 1978, Holman, 2010). Similarly in terms of friction factor, constant Poiseuille numbers in the range 56.92 – 96.00 are expected for rectangular channels with aspect ratios ranging from 0 – 1. Extensive studies over the past three decades have however produced very inconsistent results. Some studies have found the average Nusselt number to be Reynolds number dependent in the laminar regime

(Peng et al., 1994, Peng and Peterson, 1996, Choi et al., 1991), some recorded lower Nusselt numbers (Dixit and Ghosh, 2013, Qu et al., 2000, Gamrat et al., 2005) while some recorded higher Nusselt numbers (Adams et al., 1998, Celata et al., 2002, Bucci et al., 2003, Lee et al., 2005). Reviews on experimental and numerical studies of heat transfer in micro-channels published by Sobhan and Garimella (2001), Hetsroni et al. (2005b), Morini (2006), and Rosa et al. (2009) confirm the very large scatter in published results. In fact, quite recently, Dixit and Ghosh (2015) who presented the state of the art on heat transfer in micro and mini channels, noted that standard design and analysis methodology for miniaturised channels, whether using theoretical or experimental techniques, are not yet available.

The importance of the micro-channel geometry has been highlighted by many; Naphon and Khonseur (2009) concluded that the micro-channel geometry configuration has significant effect on the enhancement of heat transfer and fluid flow. Dogruoz et al. (2010) stated that the wall heat transfer coefficient shows more dependence upon geometry than upon flow rate. This chapter therefore investigates the effects of the channel geometry on the overall plate performance.

7.2.1 Theory

A numerical investigation for Nusselt numbers for laminar flow in rectangular channels under H1(constant axial wall heat flux with constant peripheral wall temperature) boundary condition was presented in Shah and London (1978). Similarly, Dharaiya and Kandlikar (2011) numerically investigated the H2 (constant axial wall heat flux with uniform peripheral wall heat flux) boundary condition in rectangular channels. These boundary conditions represent the theoretical limits for different 4-wall conductivity cases; the experimental results from this study should

fall between them. Figure 7.1a shows plots of Nusselt numbers against aspect ratios for H1(Shah and London, 1978) and H2 (Dharaiya and Kandlikar, 2011) wall boundary conditions. This figure suggests that if these heat transfer correlations apply in micro-channel absorber plates, there is significant scope for improving the heat transfer by varying the aspect ratio. It can be observed from this figure that the trend of Nusselt number with aspect ratio differs depending on the wall boundary condition; some conditions yield an increase in Nusselt number with aspect ratio while others yield reduction in Nusselt number with aspect ratio.

Solar collectors are often characterised by low flow velocities to minimise the (electrical) pumping power required. There is however a trade-off between low pumping power and reduced performance due to temperature rise in the fluid. Fully developed laminar flow will be expected in these channels because of the low flow velocities and the micro scale of the hydraulic diameter. This implies that constant Nusselt number correlation for fully developed laminar flow can be expected. The heat transfer coefficient can be expressed as

$$h = \frac{kNu}{D_h} \tag{7.1}$$

Therefore, if the fluid properties can be assumed constant, a reciprocal relationship will be expected between the heat transfer coefficient and the hydraulic diameter. This suggests that improvements in heat transfer coefficient can be achieved by reducing the hydraulic diameter. A corresponding $\Delta T_{pf} < 1°C$, can also be expected from the range of hydraulic diameters studied. Furthermore, by varying the hydraulic diameter by about 1 mm as well as changing the aspect ratio, up to 300% increase in heat transfer coefficient can be achieved. Figure 7.1b shows the corresponding heat

transfer coefficient expected at various hydraulic diameters for two extreme Nusselt number correlations. This graph suggests that varying the aspect ratio can result in up to 65% increase in heat transfer coefficient.

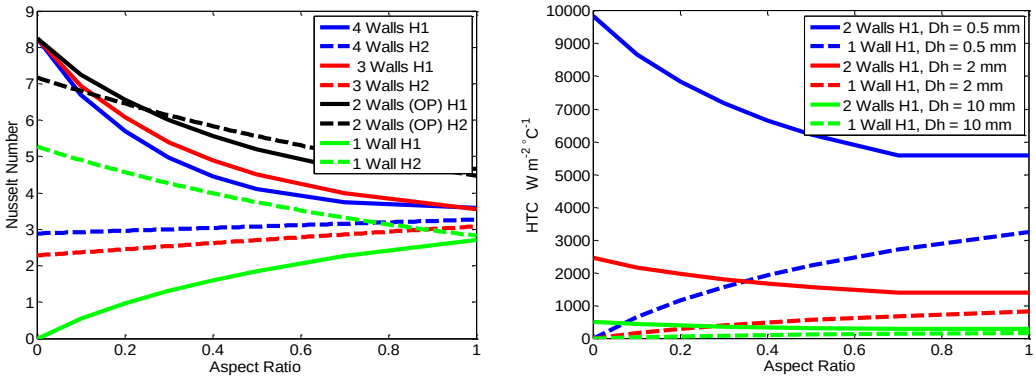

Figure 7.1: (a) H1 and H2 Nusselt numbers versus Aspect ratio (Shah and London, 1978, Dharaiya and Kandlikar, 2011) (b) Predicted heat transfer coefficient

This section investigates the effect of aspect ratio. Three plates with channels having the same width but different depths were used in the heated sandwich test rig. The geometry details of the plates are shown in Table 7.1

Table 7.1: Geometric parameters of the channels

Plate	***a*** **(mm)**	***b*** **(mm)**	***p*** **(mm)**	D_h **(mm)**	***L*** **(mm)**	**α**	N_c
C	1	2	3	1.33	270	0.5	60
E	0.5	2	3	0.8	270	0.25	60
F	0.25	2	3	0.44	270	0.125	60

7.2.2 Thermal Performance

Figure 7.2a shows measured heat transfer coefficients against fluid velocities; the three plates showed a strong dependence of heat transfer coefficient on fluid velocity, this relationship may be anticipated in some heat transfer cases as Çengel

et al. (2011) noted "*In fact, the higher the fluid velocity, the higher the rate of heat transfer*" [p.374]. At any given velocity, heat transfer coefficients from the three plates are however much lower than the predictions based on the standard *Nu* values. A heat transfer coefficient of 400 W/m^2°C (typical of these results) would be expected if the channels had D_h = 8 mm. In fact the micro-channels had D_h<1.33mm and higher heat transfer coefficients were expected. From Figure 7.2b it can be observed that the Nusselt numbers show some dependence on the Reynolds number, a trend resembling laminar predictions for flat plates and turbulent flow as opposed to laminar pipe flow. It can also be observed that the Nusselt number increases as aspect ratio approaches unity. It should be noted that the entry length for all tests in the present study was less than 20% of channel length; its effects can therefore be neglected (Rosa et al., 2009).

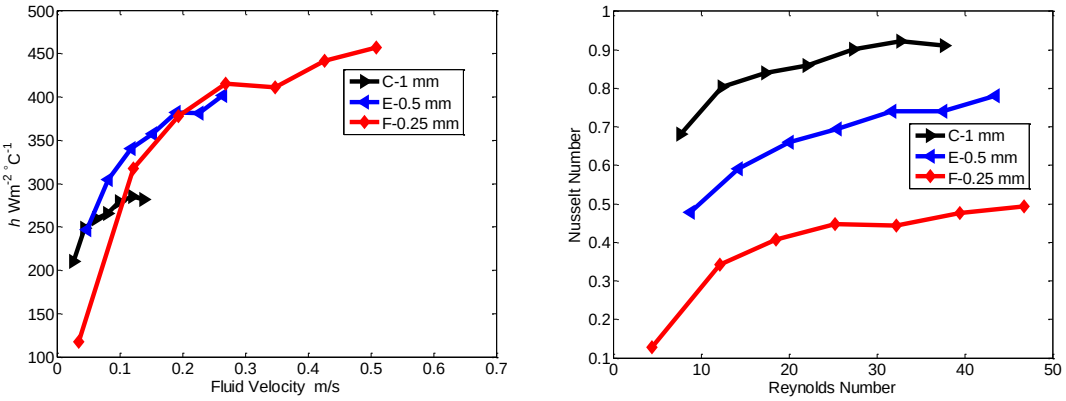

Figure 7.2: (a) Heat transfer coefficient versus fluid velocity (b) Nusselt number versus Reynolds number

Nusselt numbers of this order have been observed by several scholars who have experimentally and/or numerically studied heat transfer in micro-channels, for example, Dixit and Ghosh (2013), Qu et al. (2000), Peng et al. (1994) and Wu and

Cheng (2003). Reynolds number dependent Nusselt number correlations for micro-channels have also been proposed by Choi et al. (1991), Peng and Peterson (1996) and Peng et al. (1994). Various explanations have been postulated for these low Nusselt numbers. Celata et al. (2006) attributed this to a heat loss term, Rahimi and Mehryar (2012) and Nonino et al. (2009) attributed it to conjugate heat transfer (axial heat conduction in the duct wall).

The thermocouple position might have contributed to the low Nusselt numbers observed in the present study because thermocouple tips were at least 2 mm from the liquid/solid interface. The thermocouples in this experiment were slotted in between the top slab and micro-channel plate with a fibre-glass adhesive layer between the top slab and the thermocouple tip. Thermocouples were calibrated before and checked after the experiments and the three plates were tested under identical experimental setups. Therefore, the position of the thermocouples may yield some uncertainty in the absolute values of Nusselt numbers, but will have no effect on the relative values. In other words, the plate performance can still be qualitatively compared with minimal uncertainty. The effects of the thermocouple position will be discussed in chapter 8.

Figure 7.3a shows plots comparing the measured Nusselt numbers with predictions (Dharaiya and Kandlikar, 2011) for a channel with all four sides transferring heat under a H2 wall boundary condition. Though the value of the Nusselt number differs, a similar trend can be observed in the predicted (Dharaiya and Kandlikar, 2011) and measured Nusselt numbers. (i.e. Nusselt number increases as aspect ratio approaches unity). Figure 7.3b is a similar plot but at a fluid inlet temperature of 20 °C.

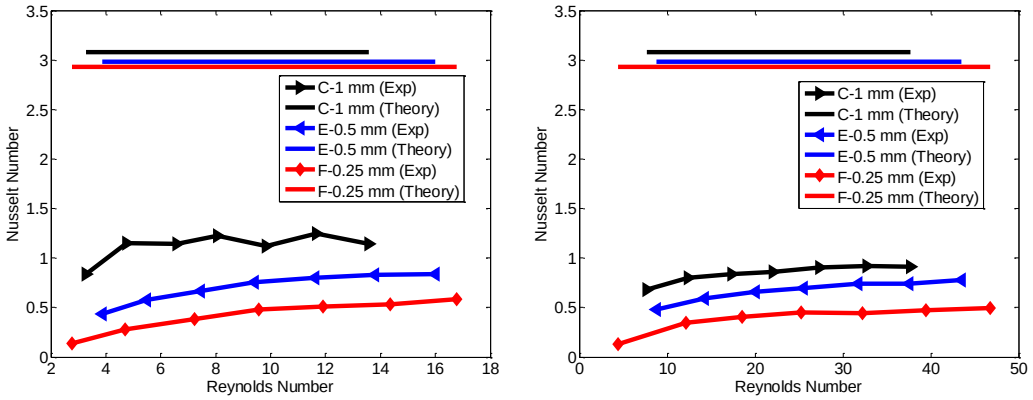

Figure 7.3: Comparing experimental results with theory (a) T_{in} = 5°C (b) T_{in} =20°C

Previous studies have produced a variety of empirical correlations, including:

- Peng and Peterson (1996), $$Nu_{\text{p\&p}} = 0.1165\alpha^{-0.79} Re^{0.62} Pr^{0.333} \left(\frac{D_h}{p}\right)^{0.81} \quad (7.2)$$
- Peng et al. (1994) $$Nu_{\text{peng et al.}} = 0.038 Re^{0.62} Pr^{0.333} \quad (7.3)$$
- Choi et al. (1991), $Nu_{\text{Choi}} = 0.000972 Re^{1.172} Pr^{0.333}$ (7.4)

Figure 7.4 compares the experimental result with these correlations; the experimental data can be observed to be in the range of correlations by Peng et al. (1994) and Choi et al. (1991) however, a lesser Reynolds number dependence can be observed in the experimental data. The correlation of Peng and Peterson (1996) , which is also aspect ratio dependent, yields Nusselt numbers that lie between these experiments and traditional correlations. The trend from this correlation is however opposite to that observed (i.e. $Nu_{\text{p\&p}}$ reduces as aspect ratio tends to unity). Actual values of heat transfer coefficient, though in the range predicted by Peng et al. (1994) and Choi et al. (1991), will need to be confirmed by further investigations.

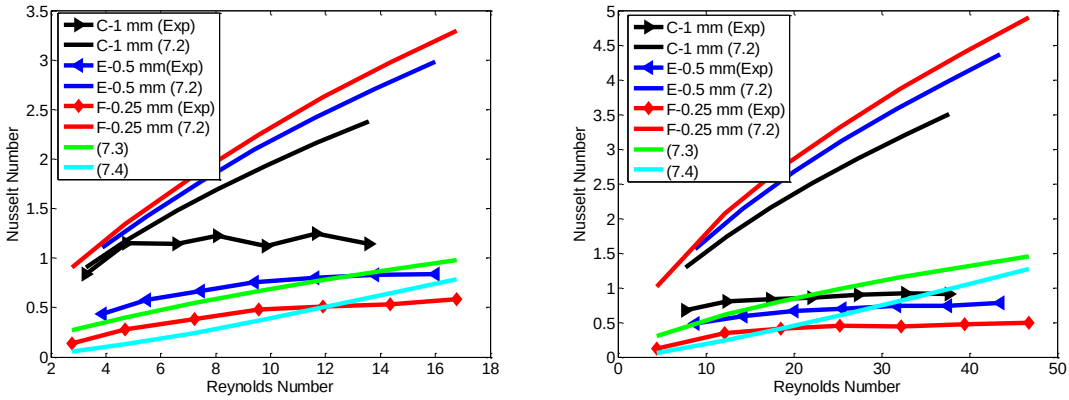

Figure 7.4: Comparing results with correlations (a) T_{in} = 5°C (b) T_{in} = 20°C

The results suggest a similar heat sinking performance (heat transfer coefficient) for the three plates, despite a difference of up to 65% in hydraulic diameters. This implies that reducing the channel size only provides marginal improvements. This trend is advantageous from a manufacturing perspective as smaller channels are potentially more expensive to fabricate due to the higher precision required. It also has the benefit of requiring less power for pumping and less likelihood of blockage.

7.2.3 Hydraulic Performance

Hydraulic performance is one characteristic that influences plate design. If the energy output is to be maximised, the power expended on pumping the fluid should be minimised. Figure 7.5a shows measured pressure drop against fluid velocity; a linear relationship between velocity and pressure drop is observed, as expected. In fact, the three curves can be approximated as one. A similar observation was noted by Hetsroni et al. (2004). These results suggest that in the range studied, the geometry design has negligible effects on the pressure drop, however, the rate of fluid flow has more significant effects. Therefore, the pressure drop is more dependent on fluid velocity rather than geometry.

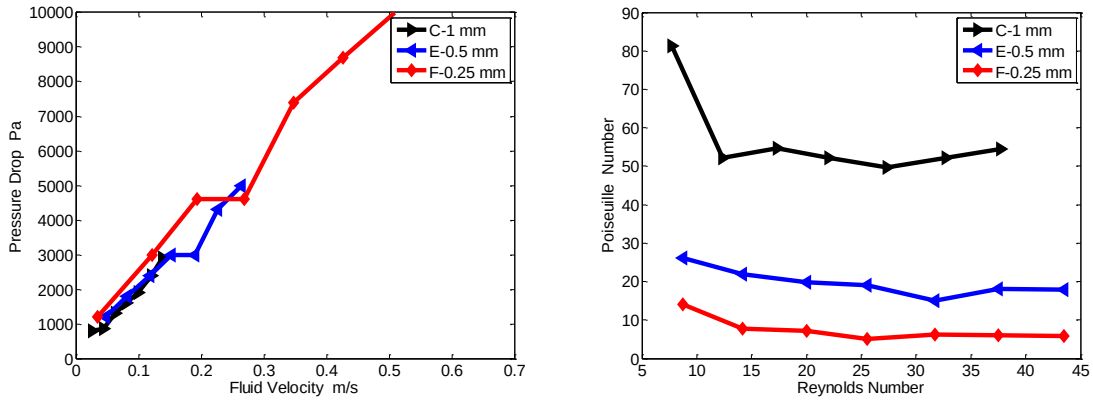

Figure 7.5: (a) Pressure drop versus fluid velocity (b) Poiseuille number versus Reynolds number

Figure 7.5b shows plots of Poiseuille numbers against Reynolds number; curves which can be approximated as horizontal lines are observed. This indicates that the flow can be approximated as a Poiseuille flow (i.e. $dPo/dRe = 0$ (Hetsroni et al., 2005a)), therefore, at a specified flow rate, the required pumping power is proportional to the length of the channel and the viscosity of the fluid but inversely proportional to the fourth power of the hydraulic diameter. Channels with larger hydraulic diameters will therefore be preferred to minimise the pumping power.

Figure 7.6a compares measured friction factors with predictions (Çengel, 2010) based on numerical Poiseuille numbers for rectangular channels. A similar trend of friction factor reducing with Reynolds number can be observed although measured friction factors are slightly lower than predicted values. Lower friction factors in micro-channels have been observed in other studies, principally for gas flows (Choi et al., 1991, Harley et al., 1995), but also for liquid flows (Xu et al., 1999, Judy et al., 2000). Lower friction factors observed in the present study may be attributed to the significant fluid temperature rise in the flow direction which is a result of low

flow velocities. Fluid temperature rise can have significant effects on the frictional characteristics; for example, when Tyfocor rises from 5°C to 10°C, the kinematic viscosity decreases by about 40% which results in a corresponding 40% increase in the local Reynolds number. Since the laminar friction factor is inversely proportional to the Reynolds number ($f=Po/Re$), an increase in local Reynolds number in the flow direction will result in lower average friction factors. This also explains the lower Poiseuille numbers observed in Figure 7.5b; at a given pumping power, smaller channels will have lower flow rates which will yield higher fluid temperature rise and consequently a lower Poiseuille number.

A plot of the pump power per collector area against fluid velocity is shown in Figure 7.6b. It indicates that the smaller the channel, the lower the power required for a given fluid velocity. This agrees with the predictions of Moss and Shire (2014), however, their predictions further show that increasing the channel size slightly can improve performance at a pumping power requirement of less than 2% of collected solar energy. Therefore, larger channels may be used; this should be sized based on pumping power limit, required fluid temperature rise and fluid properties.

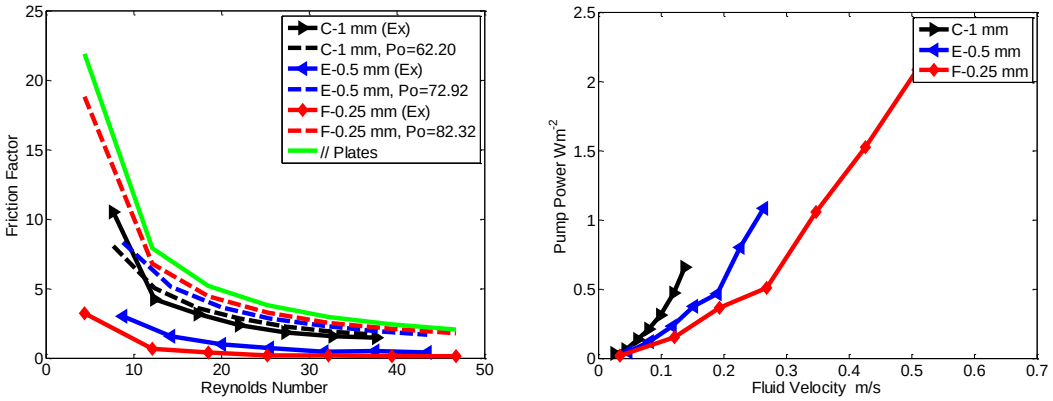

Figure 7.6: (a) Friction factor versus Reynolds number (b) Pumping power versus fluid velocity

7.2.4 Thermo-Hydraulic Performance

Figure 7.7 shows heat transfer coefficient against pump power. The curves can be seen to exhibit a profile similar to a power function whose exponent is between 0 and -1; the heat transfer coefficient flattens out at about 0.3 W/m^2; this indicates that beyond this power level, marginal improvement in thermal performance will be achieved. Plate F yielded the best heat transfer coefficient per pumping power input which might be attributed to the lower volumetric flow rate in this plate (i.e. the channels are smaller and therefore will accommodate less fluid). The curves of Plates E and F show similar heat transfer coefficient per pumping power despite the 50% difference in aspect ratio.

Lower pump power yields higher overall fluid temperatures due to lower fluid velocities. The fluid must therefore be pumped at higher velocities to achieve the solar collector's primary objective, of collecting absorbed heat with the fluid. Figure 7.7 shows that pump power per square meter of absorber plate is a minute fraction of the thermal energy typically absorbed; a solar photovoltaic system can be used to

supply this power. Thermal performance is therefore of greater importance than the pump power. It is recommended that the collector should operate in the top left quadrant of Figure 7.7 (above h= 250 W/m^2 °C) which will result in ΔT_{pf} < 4°C under an incident heat flux of 1000 W/m^2. The maximum pump power to be expended can be determined based on the minimum overall fluid temperature rise required.

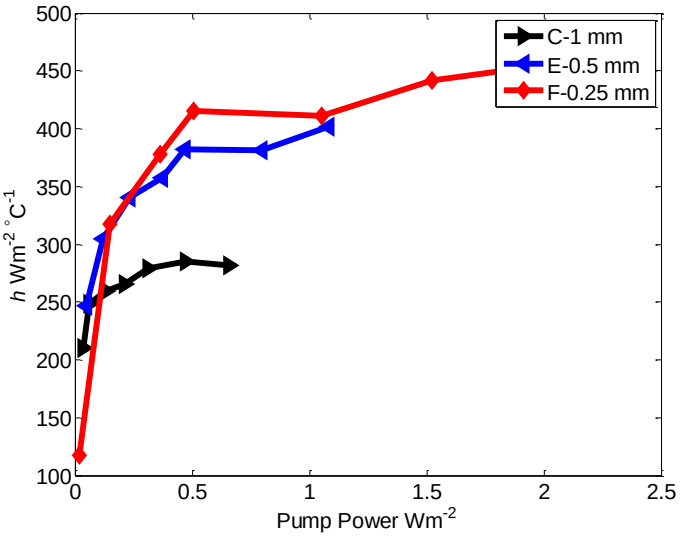

Figure 7.7 (a) Pump power vs Heat transfer coefficient

7.3 Surface Roughness

To study the significance of surface roughness, plates which had their channels manufactured by different methods were studied. Figure 7.8 shows a picture of two plates; one had the channels machined out with a circular saw while the other was photo etched. Therefore, the surface on the channel walls is likely to vary based on the manufacturing technique.

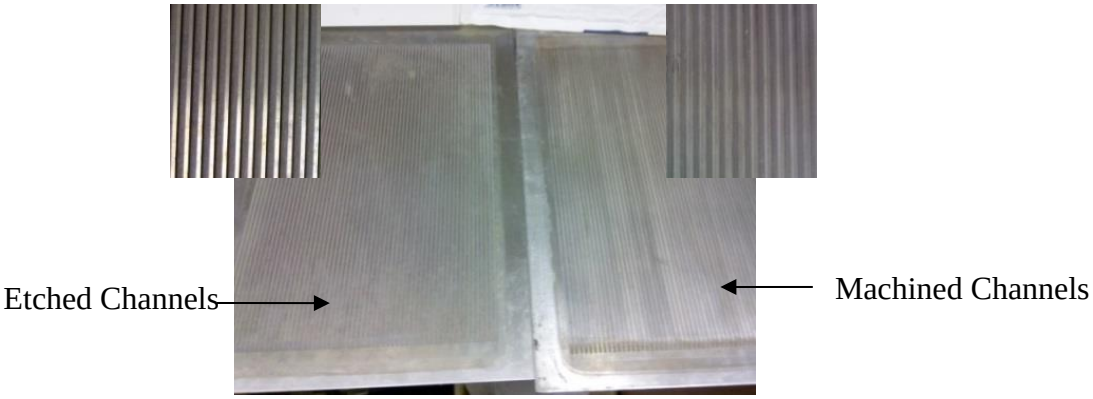

Figure 7.8: Etched and Machined channel plates

Figure 7.9 shows a 3D image of the channel surface on the top wall for an etched and a machined channel respectively. A surprising observation can be made; the etched channels which look smoother in Figure 7.8 actually have a much rougher surface finish. The machined channels are smoother but have significant variations in depth which is probably the reason for the roughness observed in Figure 7.8.

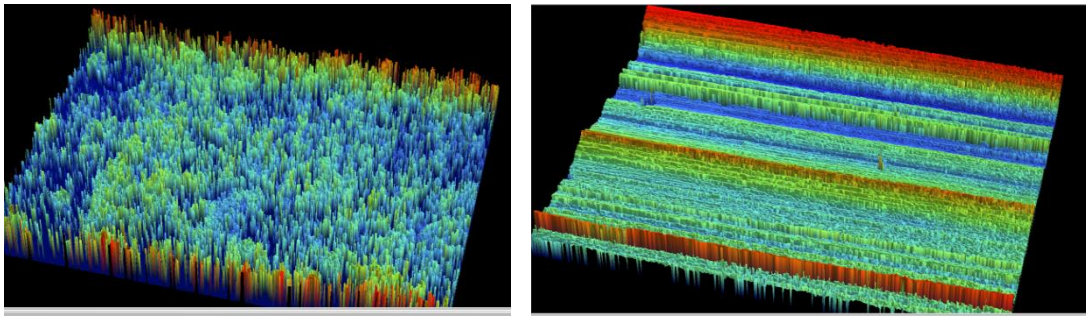

Figure 7.9: Surface finish on channel walls (a) Etched (b) Machined

Table 7.2 shows the values of some roughness parameters, defined below.

Arithmetical mean deviation $$Ra = \frac{1}{l}\int_0^l \left| z(x) \right| dx \qquad (7.5)$$

Maximum peak height $$Rp = \max z(x) \qquad (7.6)$$

Root mean squared $$Rq = \sqrt{\frac{1}{l}\int_0^l \left|z^2(x)\right| dx} \quad (7.7)$$

Maximum height of profile $$Rt = Rp - \min z(x) \quad (7.8)$$

Figure 7.10a shows a plot of the heat transfer coefficient against fluid velocity while Figure 7.10b is a dimensionless counterpart. It can be observed that the Machined channels have a slightly better performance. It would be expected that the rougher surface would have better performance but the reverse is the case here. This is not surprising as it was highlighted in the literature that surface roughness could either increase or decrease the heat transfer coefficient (Rosa et al., 2009).

Table 7.2: Roughness parameters.

S/no	Sample	*Ra* µm	*Rp* µm	*Rq* µm	*Rt* µm
1	Etched 1	3.713	19.36	4.949	36.29
2	Etched 2	3.992	21.62	5.091	35.726
3	Etched 3	3.043	19.2	4.083	32.946
4	Machined 1	2.657	22.021	3.525	32.773
5	Machined 2	3.475	11.261	4.604	22.606
6	Machined 3	2.234	10.668	3.134	19.153
7	Aluminium 1	0.543	3.946	0.676	9.432
8	Aluminum 2	0.322	1.74	0.399	8.954
9	PTFE	1.446	6.306	1.937	28.181
10	Perspex	0.029	1.804	0.0461	2.972

Figure 7.11 show the fluid flow performance, as expected, the etched channels are characterized by higher pressure drops and higher friction factors. This is what is expected in rougher channels, as surface roughness is responsible for an increase in

Poiseuille number in micro-channels as noted by Wu and Cheng (2003), Koo and Kleinstreuer (2005) and Rosa et al. (2009).

The paradoxical behaviour of increasing pressure drop and decreasing heat transfer may be attributed to wettability. A closer look at the surface of the etched channels suggests that the etching process might have compromised the wettability of channel surfaces leading to a thin layer of trapped air on the surface. This reduces the heat transfer and also reduces the channel diameter. A reduced channel diameter will increase the flow velocity as well as increase the pressure drop.

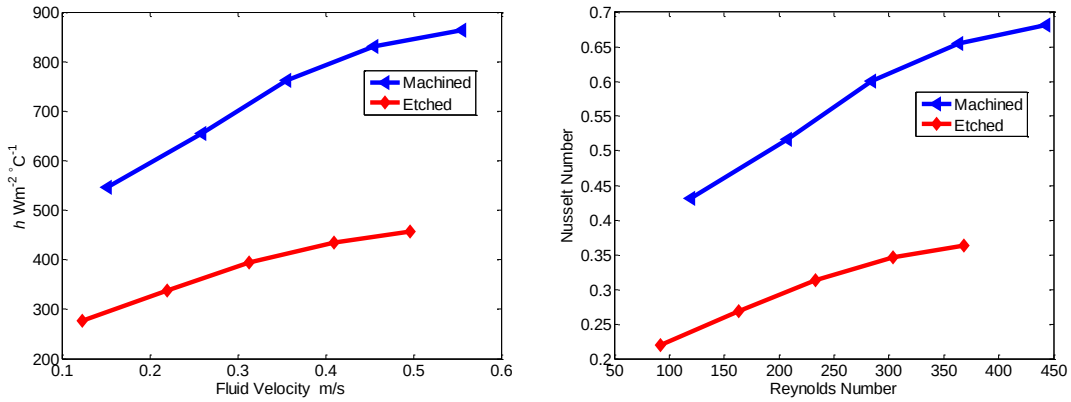

Figure 7.10: Comparing machined and etched channels

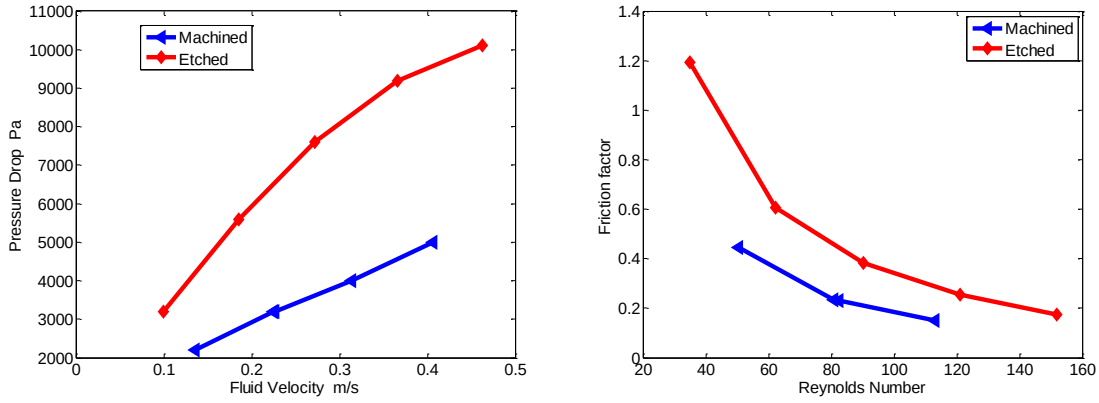

Figure 7.11: Pressure drop and friction factor

This analysis has practical importance as it illustrates that the method adopted for channel fabrication can have significant effect on the performance. It can be deduced that plates with etched channels will yield a poorer performance compared with plates with machined channels. Therefore, this technique should be avoided. However, the design of channel geometry may necessitate using this method as more versatile shapes can be produced; in this case however, the lower heat transfer and higher pressure drop should be accounted for in the design process.

7.4 Manifold

In the experimental data, the effects of manifold are neglected. However, they may play a significant role. Cabuk and Modi (1989) noted that uniform header flow is necessary to maximize heat transfer with an acceptable loss in pressure for the constraints of system geometry. The effect of the manifold may be difficult to study experimentally, however, a numerical simulation can give a good picture of the flow distribution in the plate. Figure 7.12 shows the temperature profile of the plate at 0.1mm below the fluid – solid interface. This profile is almost impossible to detect with thermocouples, it can be noted that the temperature along the width is not uniform; therefore, assuming uniform heat and mass transfer in all channels may be slightly misleading. Figure 7.13 shows the temperature distribution from left to right at different locations up stream; a ‘u’ shaped curve which becomes flatter in the flow direction can be observed.

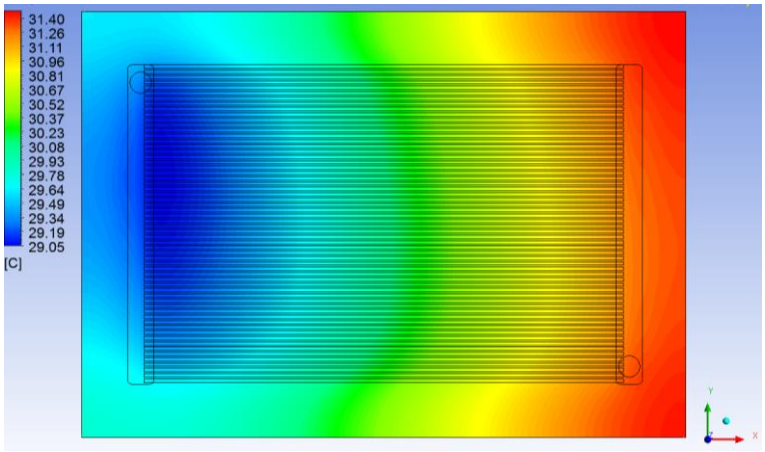

Figure 7.12: Plate temperature at the plate fluid interface

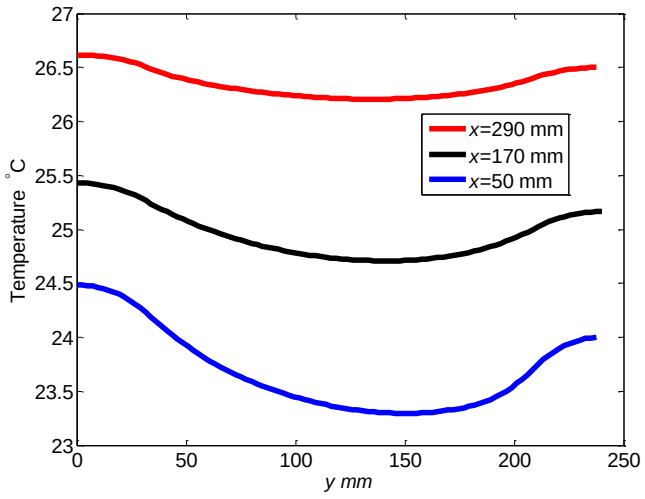

Figure 7.13: Temperature profile transversely

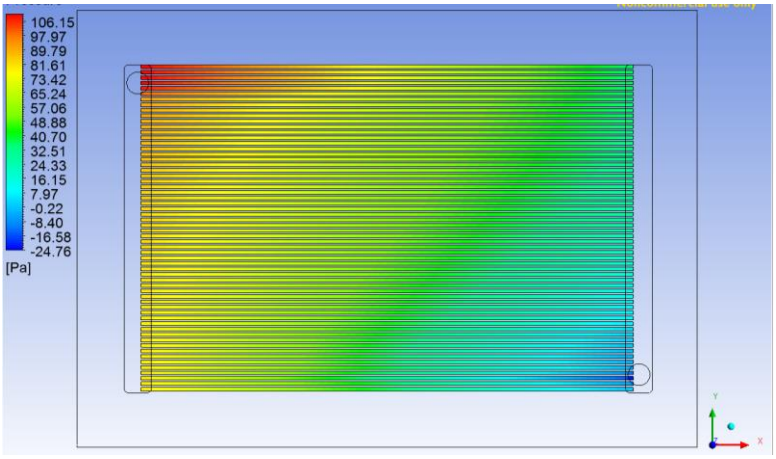

Figure 7.14: Pressure distribution in the channels

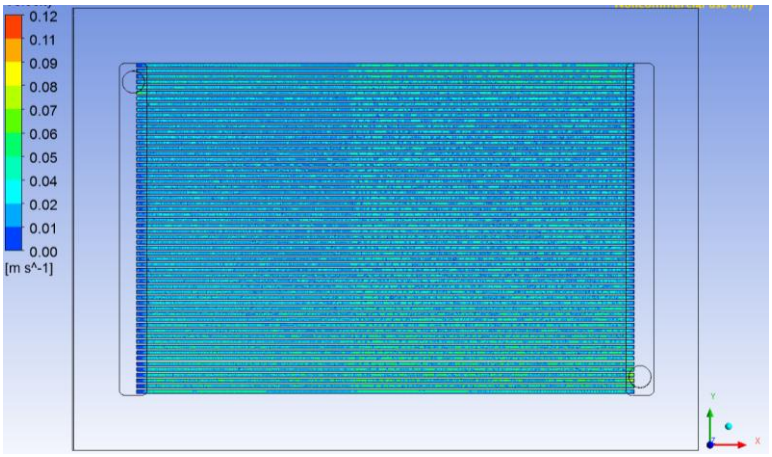

Figure 7.15: Velocity distribution in channels

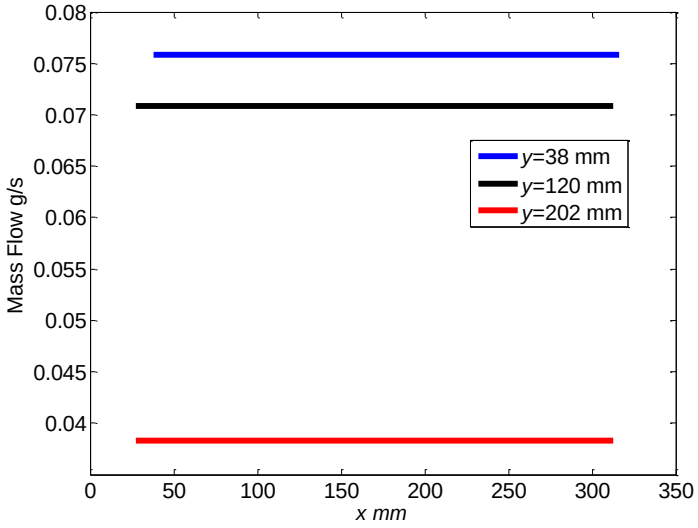

Figure 7.16: Mass flow rate in 3 channels

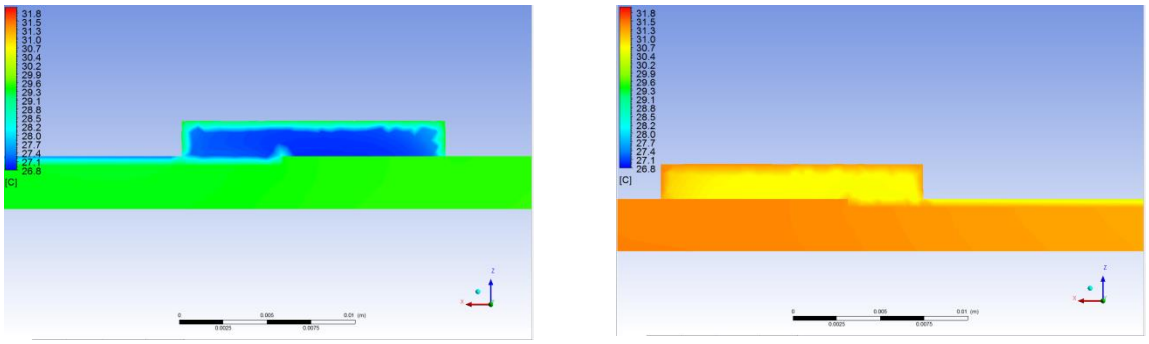

Figure 7.17: Temperature in manifold (a) inlet (b) outlet

A contour showing pressure distribution in the channels is presented in Figure 7.14, much higher pressures are recorded in the region just above the inlet port. The velocity distribution (Figure 7.15) shows that there is a proportionately large variation the profile. Figure 7.16 shows that the mass flow rate in the channels close to the inlet port are almost double the flow rate in those close to the outlet port. Figure 7.17 shows the temperature profile in the manifolds, a similar distribution can

be seen in both inlet and outlet manifolds. The distribution shows that there is heat transfer in the manifolds.

7.5 Summary

Experimental and numerical analyses have been carried out to investigate the effects of aspect ratio, surface roughness and the manifolds. Conventional correlations for rectangular channels were found to over-predict the thermal performance of the plates. The results showed a strong dependence of heat transfer coefficient on fluid velocity. Nusselt number was dependent on Reynolds number, a trend which is conventional for flat plate or turbulent flows but not laminar flow in ducts. Experimentally measured friction factors were similar in trend to published data although slightly lower than predicted values based on numerical Poiseuille numbers for rectangular channels. The heat transfer coefficient increased with pump power; this improvement becomes marginal above a pump power of 0.3 W/m^2. More power might however need to be expended beyond this level to minimise the overall fluid temperature rise.

It was observed that the method of fabricating the channels can result in significant degree of surface roughness. Similarly, the manifolds can result in significant mal-distribution.

8. Investigating Scaling Effects

8.1 Background

The literature review presented in Chapter 2, highlighted the wide scatter in results in experimental and numerical studies of heat transfer in micro-channels. Reviews by Morini (2006), Hetsroni et al. (2005b), Rosa et al. (2009) and Sobhan and Garimella (2001) confirm the very large scatter in published results and unanimously attribute this to "scaling effects". These effects arise from neglecting phenomena which are insignificant in conventional sized channels but become significant as a result of the high channel wall surface to fluid volume ratio in micro-channel flow.

The significance of these scaling effects can be influenced by the design and application; also, the overall performance can be improved or depreciated, depending on the dominant scaling effects. The extensive study on micro-channels has been largely in the context of cooling electronic components. The peculiarities of micro-channel heat transfer application in solar collectors include low Reynolds numbers as well as the low heat flux densities. This chapter numerically and experimentally studies the significance of some of these "scaling effects" on the performance of the absorber plates.

8.2 Entrance effects

One of the common scaling effects cited by researchers is entrance effects (Guo and Li, 2003, Lee et al., 2005). Constant local Nusselt numbers are expected for fully developed flow however entrance effects can yield a significant variation between predicted and measured average Nusselt number. The Graetz number, *Gz*, defined in equation (8.1), is used as the criterion for neglecting entrance effects.

$$Gz = \frac{RePrD_h}{L} \tag{8.1}$$

The entrance effects on the average Nusselt number can be neglected if the inequality in equation (8.2) is satisfied (Rosa et al., 2009, Morini, 2006)

$$Gz < 10 \tag{8.2}$$

Figure 8.1 compares ΔT_{pf}, at different Graetz numbers. This plot assumes a linear fluid temperature increase from entry to exit, because under a constant heat flux, the effects of entry length is seen mainly on the surface temperature profile (Çengel et al., 2011). The magnitude of ΔT_{pf} can be observed to increase in the flow direction. Since,

$$q = \frac{Q}{S_c} = h\Delta T_{pf} \tag{8.3}$$

This trend of increasing ΔT_{pf} in the flow direction suggests an axial variation in the heat transfer coefficient and/or the heat flux density.

Figure 8.2 compares the local Nusselt number at different Graetz numbers. This Nusselt number is estimated by using the average heat flux, the measured plate temperature axially, $T(x)$ and an axial fluid temperature profile $T_f(x)$ from the model developed in chapter 3. A progressive decay of Nusselt number axially can be observed in Figure 8.2. A flow characterised by a significant developing entry region will yield a Nusselt number profile $Nu(x)$ in the developing region and decay to a constant value in the fully developed region. The relationship between the percentage of flow in the thermally developing region and the Graetz number is shown in equation (8.4).

$$\frac{L_t}{L}(\%) = 5Gz \tag{8.4}$$

From this relationship, the percentage of thermally developing flow in Figure 8.2a should be around 14%, 22.5% and 31.5% for Gz = 2.8, 4.5 and 6.3 respectively. This will imply that the local Nusselt number should be constant after these points. Also, since equation (8.2) is satisfied and Gz<10 the effects of entry length can be neglected (Rosa et al., 2009, Morini, 2006). This signifies that the thermally developing region may not be the sole contributor to the observed profile.

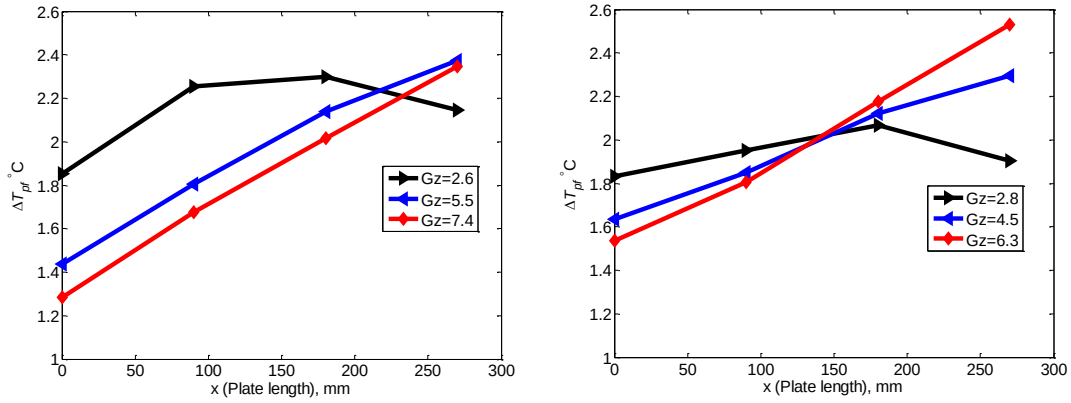

Figure 8.1: Profile of ΔT_{pf} along the plate (a)T_{in} = 5°C (b) T_{in} = 20°C

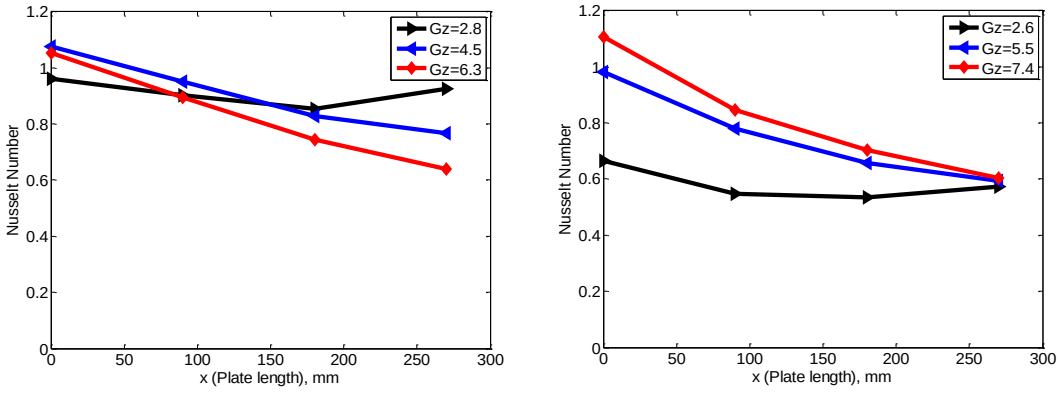

Figure 8.2: Local Nusselt number along the plate (a)T_{in} = 5°C (b) T_{in} = 20°C

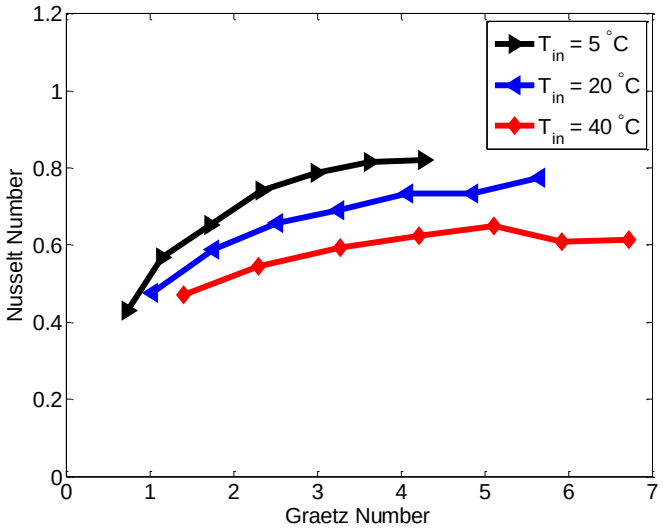

Figure 8.3: Nusselt number vs Graetz number at various fluid temperatures

Figure 8.3 shows the Nusselt numbers as a function of Graetz number. Nusselt number increases slightly and then becomes fairly constant. The heat transfer coefficient is enhanced in the thermal entry region; therefore, the Nusselt number is expected to be constant at low *Gz* numbers and then increase at high *Gz* when thermal entry length is significant. The profile observed supports the assumption that the entrance effects may not be the sole contributor to the profiles observed. If it was, a progressive increase of Nusselt number at higher *Gz* should be seen.

The hydraulic entry length is difficult to measure experimentally; however, the thermal entry length gives a good indication of the hydraulic entry length since $L_t = PrL_{hyd}$. A CFD simulation was done on plates with five channels, 500 mm long. Figure 8.4 shows the velocity profile on a transverse plane at the middle of the channel for the entry and exit sections. The flow can be observed to be fully developed when the fluid is a few millimetres upstream from the manifold. This agrees with the predicted hydraulic entry length, which is less than 10 mm (2% of

flow). A fairly similar velocity profile can also be observed at the outlet section. This indicates that the hydraulic boundary is consistent with conventional theory

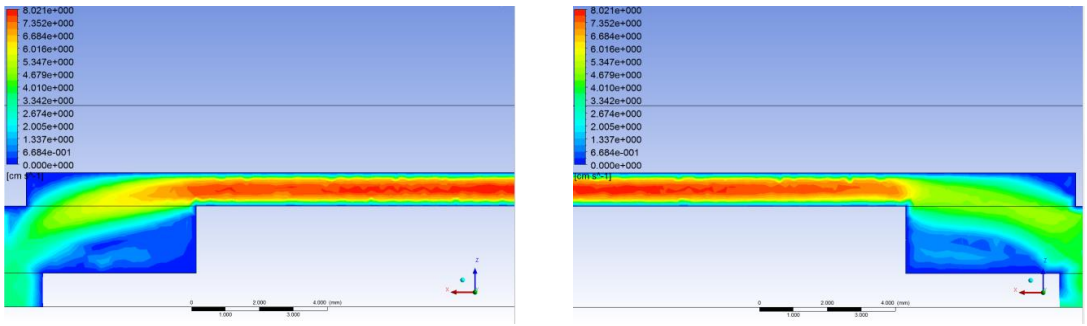

Figure 8.4: Transverse velocity profile at (a) entry (b) exit

Figure 8.5 shows contours on horizontal planes at 5 mm, 250 mm and 495 mm upstream. A similar profile can be observed in all three contours. This suggests that the fully developed flow profile is constant for most of the channel length.

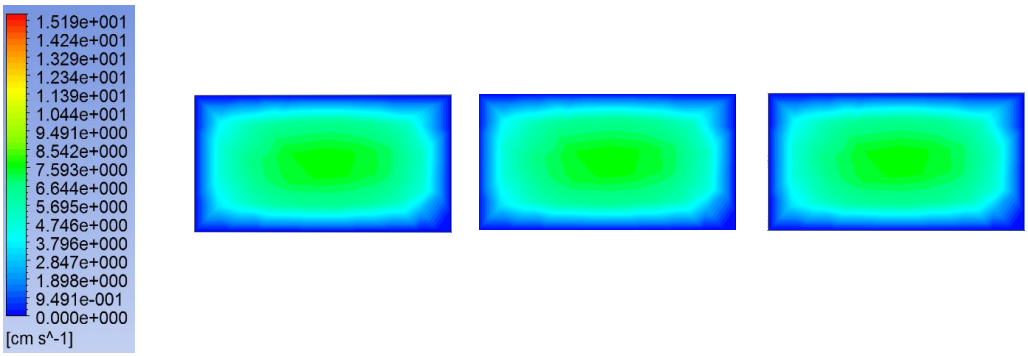

Figure 8.5: Horizontal velocity profile at different locations

8.3 Viscous dissipation

In macroscopic flows through channels, internal generation of heat is usually neglected, however, at very small hydraulic diameters, viscous forces can generate significant internal heat, which can in turn influence the heat transfer (Rosa et al., 2009). Koo and Kleinstreuer (2004) noted that viscous dissipation can be significant

in rectangular channels even for low Reynolds numbers. Others who have highlighted the significance of viscous dissipation include Tunc and Bayazitoglu (2001), Toh et al. (2002), Morini (2006), Herwig and Mahulikar (2006), Jeong and Jeong (2006) and Chen (2006).

The Brinkman number, defined in equations (8.5)&(8.6), which is the ratio between the viscous heating rate and the fluid – channel walls average heat transfer rate, is usually employed to evaluate the significance of viscous heating (Rosa et al., 2009). Equation (8.7) has been proposed as the criterion for accounting for the effects of viscous heating (Rosa et al., 2009, Morini, 2006).

For constant wall het flux,
$$Br = \frac{\mu v_m^{\,2}}{q_L} \tag{8.5}$$

For constant wall temperature,
$$Br = \frac{\mu v_m^{\,2}}{k_f \Delta T_{pf}} \tag{8.6}$$

$$Br < \frac{\xi_{\lim} D_h^{\,2}}{2(ab)\, fRe} \tag{8.7}$$

Where $\xi_{\lim}$ is the maximum allowable ratio between the temperature rise due to viscous dissipation and the temperature rise due to supplied heat flux at the wall (for example, $\xi_{\lim}$=5%) (Rosa et al., 2009).

A plot of Nusselt number against Brinkman number is shown in Figure 8.6. The curves can be seen to be almost horizontal lines with the exception of Nusselt numbers at lower Brinkman numbers (which correspond to lower flow velocities). Viscous dissipation can result in lower Nusselt numbers (Rosa et al., 2009, Morini, 2006), however this occurs at higher flow velocities. It can therefore be concluded that the lower Nusselt numbers at lower Brinkman numbers are not due to viscous

dissipation. In addition, equation (8.6) yields *Br* satisfying equation (8.7) with ξ_{lim}=10%. The effects of viscous dissipation in the proposed design will therefore be insignificant at typical FPC operating conditions.

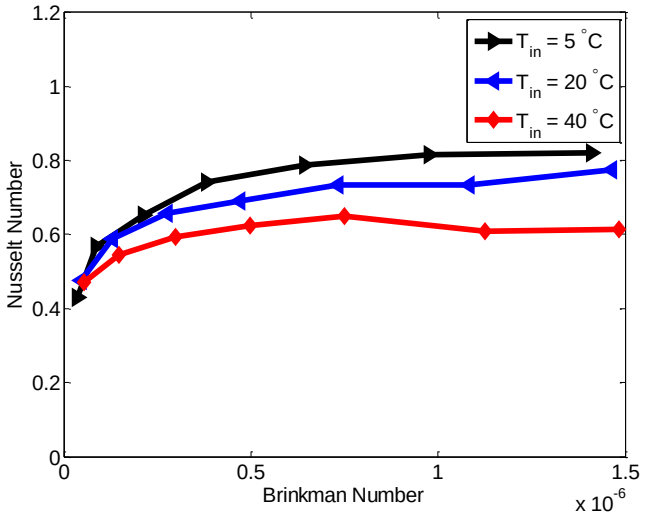

Figure 8.6: Brinkman number vs Nusselt number at various fluid temperatures

8.4 Conjugate Heat Transfer

Conjugate heat transfer is another scaling effect often cited as having significant influence on the thermal performance of micro-channels. This arises because the hydraulic diameter and the wall thickness of the channels are usually of the same order of magnitude. It therefore becomes necessary to account for the axial thermal conduction in the channel walls, in addition to the forced convective heat transfer. Some scholars who have highlighted the effects of conjugate heat transfer include Gao et al. (2002), Gamrat et al. (2005), Nonino et al. (2009), Rosa et al. (2009) and Rahimi and Mehryar (2012).

The dimensionless axial conduction number, *M*, defined in equation (8.8), which can be seen as the ratio of axial thermal conduction to convective heat transfer, can

be used to characterise effects of conjugate heat transfer in micro-channels (Maranzana et al., 2004).

$$M = \frac{k_p}{k_f}\frac{A_{cp}}{A_f}\frac{1}{RePr} \tag{8.8}$$

Where A_{cp} is the cross sectional area of the solid walls of the channel and A_f is the wetted surface area. The axial thermal conduction in the channel walls can be neglected if the inequality in equation (8.9) is satisfied (Rosa et al., 2009, Maranzana et al., 2004)

$$M < 0.01 \tag{8.9}$$

In terms of the experimental data reduction, the axial conduction number was estimated by

$$M = \frac{k_p}{k_f}\frac{D_h}{L}\left(\frac{\delta L_y}{\delta L_y - N_c ab} - 1\right)\frac{1}{RePr} \tag{8.10}$$

δ includes the top and bottom slab thickness

A plot of Nusselt number against axial conduction number is shown in Figure 8.7; an inverse relationship can be observed. This trend signifies that the axial conduction number has a negative impact on the Nusselt number which is in agreement with the proposition of Morini (2006) and Rosa et al. (2009). Since the axial conduction number was generally found to be greater than 0.01, satisfying equation(8.9), conjugate heat transfer has some impact on the experimental results.

Therefore, the negative effect of conjugate heat transfer on thermal performance can be suppressed by having micro-channel geometries with thin walls. This type of channel can be achieved by increasing channel diameter and reducing plate thickness, for example, hydroforming thin metal plates rather than machining thicker plates. Effects of conjugate heat transfer can be further suppressed by ensuring the flow rate through the collector is high enough to yield Reynolds numbers which result in the effects of conjugate heat transfer being negligible.

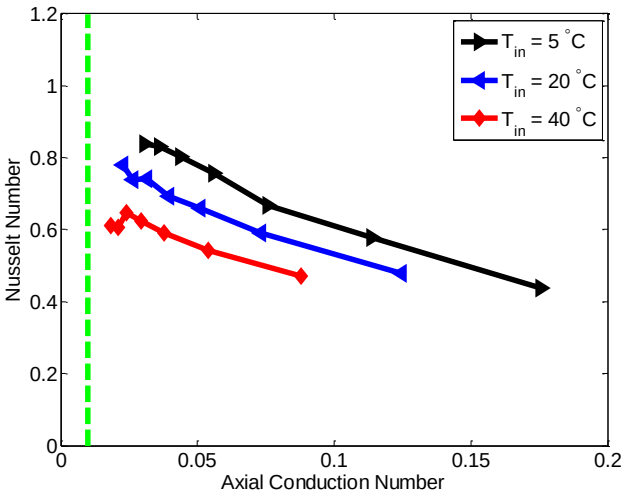

Figure 8.7: Nusselt number vs axial conduction number

The thermal boundary at the surface of ducts can usually be approximated as either a constant surface heat flux or constant surface temperature (Çengel et al., 2011). The profile of the surface and fluid temperature in the flow direction can be used to easily identify the type of thermal boundary in fully developed flow. A constant surface heat flux boundary will result in a linear increase in the surface and fluid temperature at the same rate (Çengel et al., 2011). Under an isothermal surface boundary condition, the temperature difference between the fluid and plate decays exponentially in the flow direction (Çengel et al., 2011).

However, when conjugate heat transfer is present, a deviation from the idealised boundary condition can occur; it will result in variation of the heat flux density axially. This might be responsible for the axial variation in ΔT_{pf} observed in Figure 8.1. The model presented in chapter 3, which includes, axial thermal conduction, shows that despite a uniform incident solar heat flux on the plate, axial thermal conduction can generate a plate temperature profile similar to an isothermal boundary at the entry and exit regions and a constant wall heat flux boundary in between. Figure 8.8 compares profile of ΔT_{pf} from this model at two extreme cases. It can be seen that axial thermal conduction can yield significant axial variation in the plate temperature.

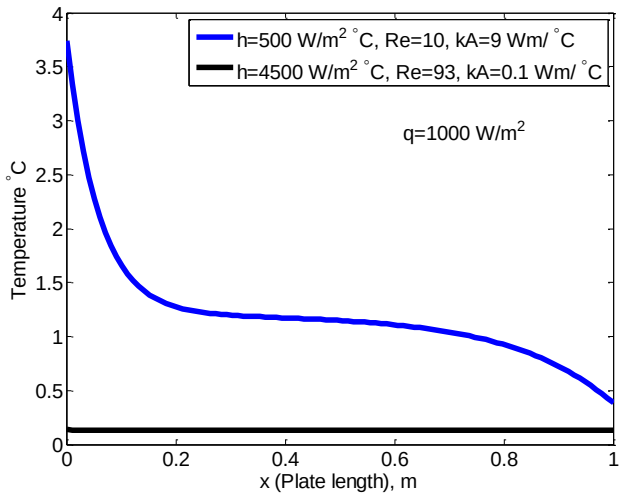

Figure 8.8: Profile of ΔT_{pf} at two extreme cases

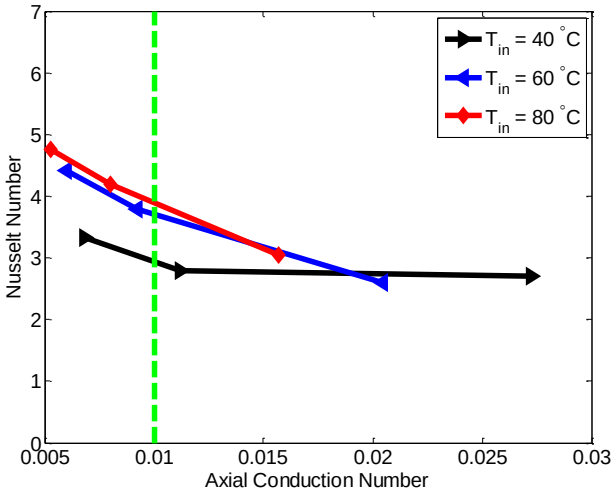

Figure 8.9: Nusselt number vs axial conduction number in Counter flow heat exchanger

Figure 8.9 shows a plot of the counter flow heat exchanger Nusselt numbers against axial conduction number. A similar relationship of Nusselt number decreasing with Axial conduction number can be observed. Conjugate heat transfer will also explain the Reynolds number dependence observed because, as the Reynolds number increases, axial conduction effects in the channel walls decrease.

To study the effects of conjugate heat transfer further, a simulation was done on the plate with 500 mm long channels. Figure 8.10 shows the simulated axial temperature profile at the top surface and the middle of the fluid. A trend consistent with a constant temperature surface boundary condition is observed at the entry, while the middle section resembles a constant wall heat flux condition. The significance of axial thermal conduction will depend on several factors including the plate material and flow velocity, for example a more conductive material and/or a lower flow velocity will yield more significant effects.

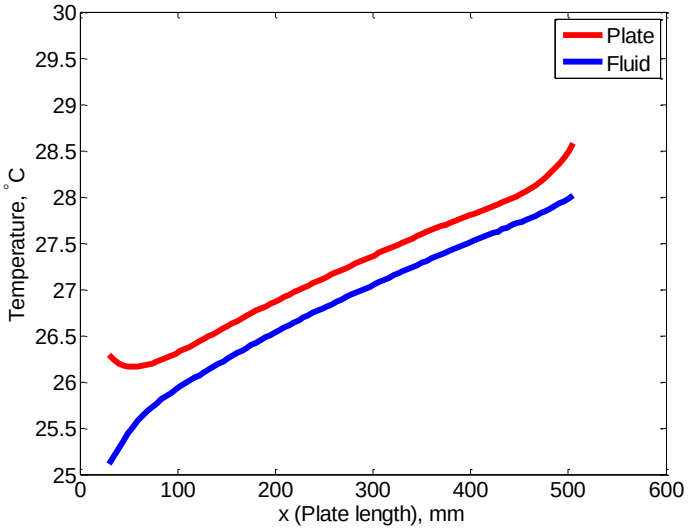

Figure 8.10: Simulated fluid and plate temperature profile

Figure 8.11 compares the axial surface temperature profile on the four walls; three walls (top and sides) can be observed to have approximately the same temperature profile while the fourth side differs by about 0.5 °C. This difference may be attributed to thermal contact resistance between the inter-passage ribs and cover plate (The channel is made by clamping a cover plate hard against inter-passage ribs of rectangular passages). This suggests that the surface boundary varies peripherally. It also indicates that the method of manufacturing the channel can significantly alter the surface boundary condition. Other methods of channel manufacture such as welding two hydro-formed sheets together (as required to prevent the plate ballooning under pressure/vacuum) should provide good thermal connection and promote a more uniform peripheral temperature.

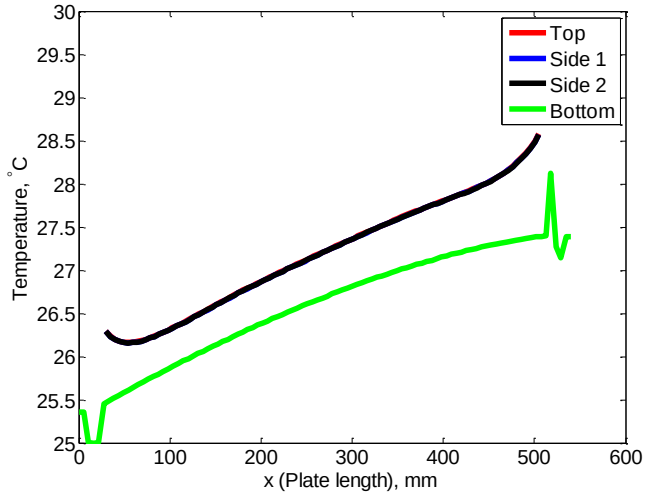

Figure 8.11: Temperature profile at channel walls

The heat flux density from the four walls is shown in Figure 8.12. The top and sides walls have a similar profile; about 300% of the average heat flux can be observed at the inlet section, this then reduces to 60-80 % (depending on which wall) in the middle section and then rises slightly at exit. This profile further confirms axial thermal conduction in the plate. A slightly higher heat flux can be observed from the top wall compared with the side walls; the side walls have a similar heat flux, while the bottom wall can be observed to be adiabatic. This indicates that thermal contact resistance between the bottom slab and the channel ribs is high; therefore heat is transferred from only three walls. It may however be possible to have heat transferred from the four walls if channels are manufactured from methods which ensure the four walls are in good thermal contact.

It can therefore be concluded that in this design of micro-channel plates, heat transfer can be expected to occur from three walls only. The heat flux is non-uniform peripherally; however a uniform peripheral temperature can be expected on the walls transferring heat. Thermal conduction in the channel walls can modify the thermal

wall boundary profile at the inlet and exit, however, the middle section of the channel can be approximated as a rectangular channel with three walls transferring heat under a H1 (constant axial wall heat flux with constant peripheral wall temperature). This is consistent with Lee and Garimella (2006) suggestion that micro-channels are best represented by H1 boundary condition. From Shah and London (1978) the expected Nusselt number for fully developed flow through a channel with three sides transferring heat under H1 boundary condition ranges from 3.146 to 8.235, depending on the aspect ratio.

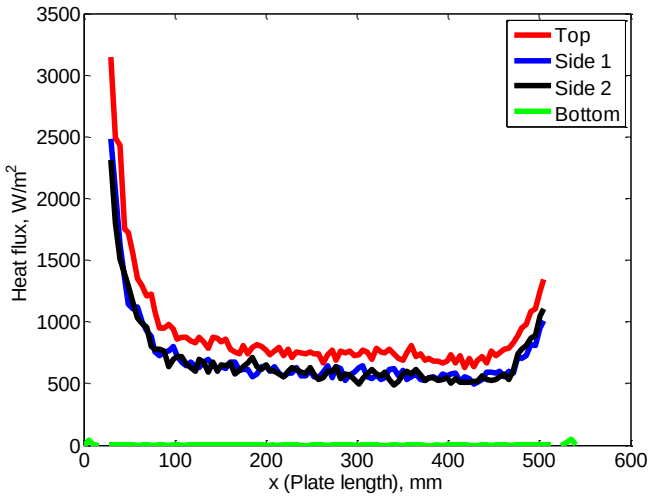

Figure 8.12: Heat flux profile at channel walls.

Figure 8.13 compares the simulated profiles to those predicted by this model. The predictions are based on the average heat flux density at the middle section as well as heat transfer coefficient from numerical H1 Nusselt number for a channel with aspect ratio of 0.5 and one adiabatic wall (Nu=3.306). The simulated and predicted profile can be observed to match closely although a slight variation can be seen at the inlet and exit. This can be attributed to the mass of fluid in the manifolds; the analytical model only considers flow in the channel.

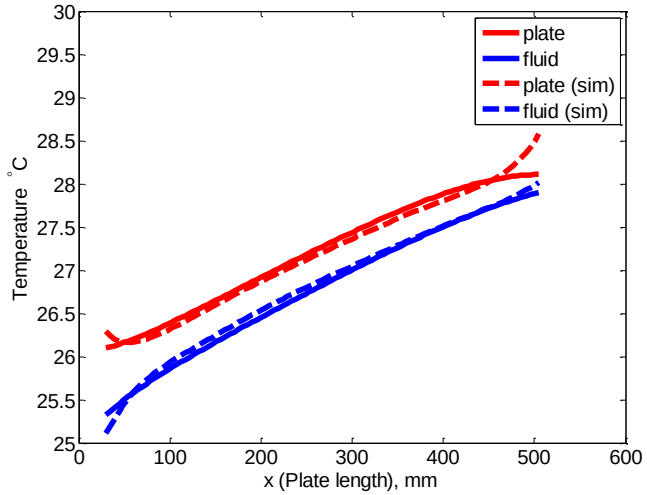

Figure 8.13: Comparing analytical and simulated results

8.5 Measurement uncertainties

Several studies have cited measurement uncertainties as another possible explanation of the discrepancies between experimental and theoretical results (Celata, 2004, Celata et al., 2006, Morini, 2004). Some of these uncertainties include channel diameter variation axially, accurately measuring fluid and channel wall temperatures and assuming similar conditions in all channels.

The thermocouples measuring plate temperature were placed at the interface between the top slab and micro-channel plate (with a fibre-glass adhesive layer between the top slab and the thermocouple tip). Thermocouples might have been reading a temperature at the interface rather than the plate temperature if there was significant thermal contact resistance between thermocouple tips and plate. Similarly, plate temperatures were read at 2 mm from the liquid/solid interface. Gamrat et al. (2005) observed that the position of the thermocouples away from the liquid/solid interface can yield as much as 40% uncertainty in the estimated Nusselt number. It should be noted that the accuracy of the measuring instruments as well as the repeatability of

the experiment were validated. Therefore a correction can be applied to the temperature measurements using Fourier's law. The interface thickness (discussed in Chapter 4) was used to estimate the temperature gradient across the interface and the plate temperature was corrected, assuming that measured temperature was in the middle of the interface.

$$T_{p,\text{corrected}} = T_p - \frac{\Delta T_{\text{int}}}{2} \tag{8.11}$$

Figure 8.14, shows a plot of the corrected Nusselt numbers against Peclet numbers. The error bars in this figure account for other uncertainties such as fluid properties, flow rate and geometry. The corrected local Nusselt numbers are shown in Figure 8.15. Figure 8.16 compares the corrected Nusselt number as a function of Axial Conduction number.

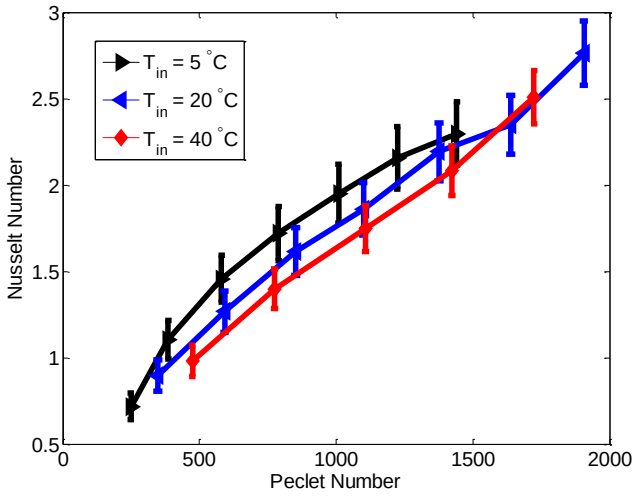

Figure 8.14: Corrected Nusselt numbers versus Peclet numbers

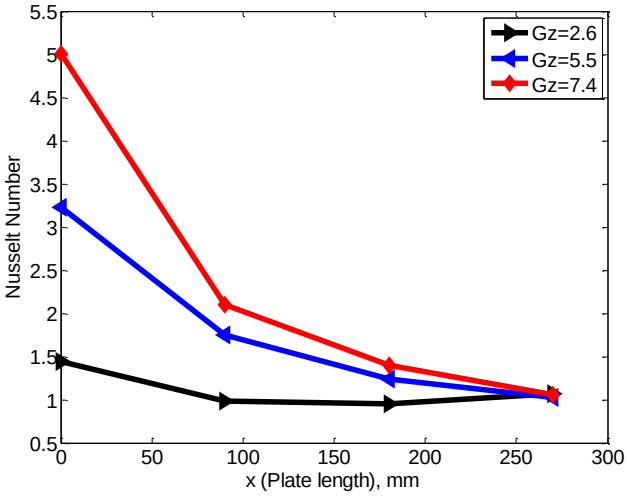

Figure 8.15: Corrected local Nusselt numbers

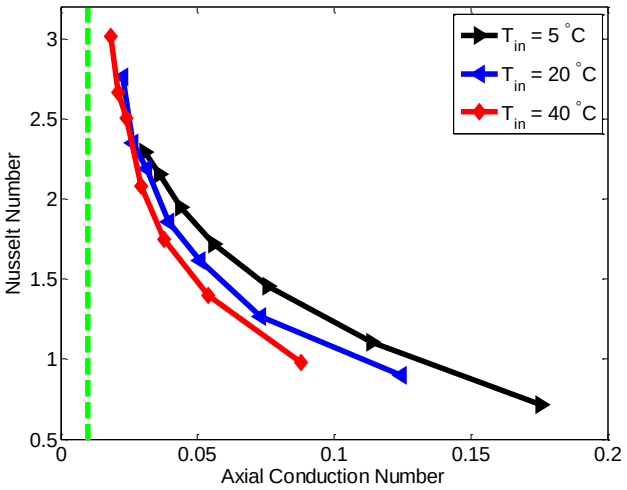

Figure 8.16: Corrected Nusselt number vs axial conduction number

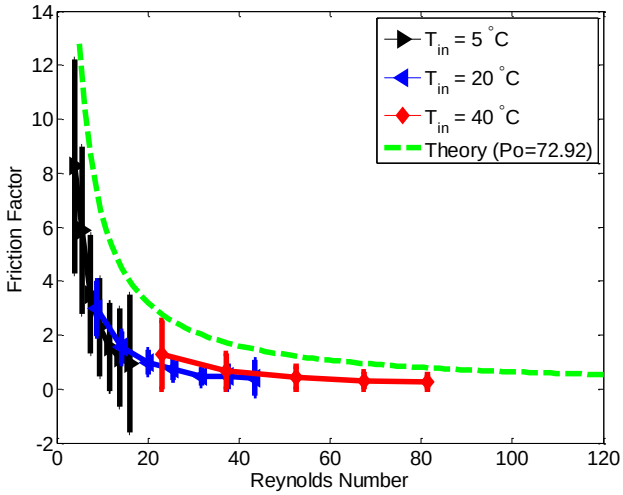

Figure 8.17: Friction factor versus Reynolds number

Figure 8.17 shows a plot of the corrected friction factor versus Reynolds number. The error bars in this figure account for uncertainties in fluid properties, geometry and measurements. It can be observed that the error bars are close to the theoretical values.

8.6 Heat Transfer Correlation

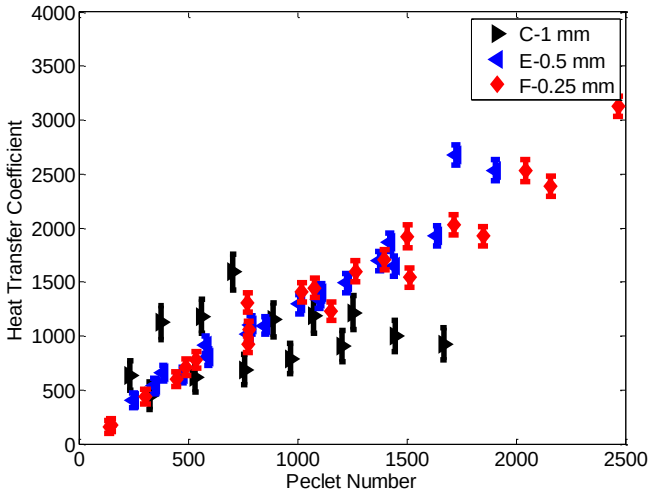

Figure 8.18: Heat transfer Coefficient versus Peclet number

Figure 8.18 shows the measured heat transfer coefficient from several experiments (various plates, various fluid temperatures and various flow rates), as a function of Peclet number. It can be observed that the data points have a trend. This trend could be approximated as

$$h_{corr} = 1.25Pe \tag{8.12}$$

By substitution, this becomes

$$h_{corr} = 2.50\frac{\dot{m}c_p}{(a+b)k_f} \tag{8.13}$$

Figure 8.19 compares the correlation in (8.12) with the measured heat transfer coefficients; it can be observed that results from plates E and F are closer to the correlation while plate C, which has larger channels, is more spread out.

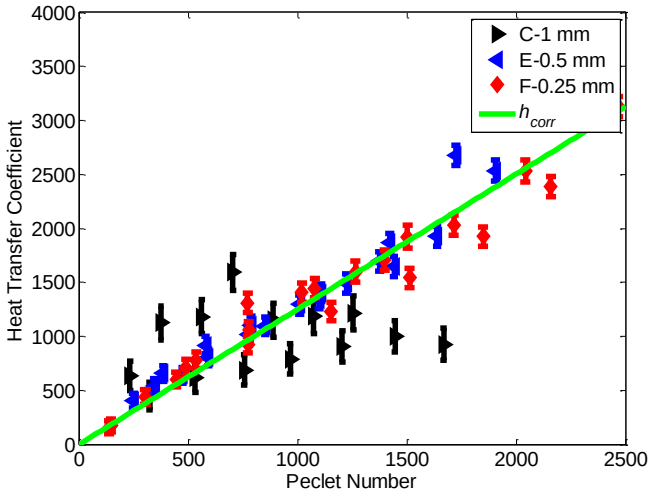

Figure 8.19: Heat transfer correlation

8.7 Summary

The significance of various scaling effects on the heat transfer in micro-channel absorber plates has been experimentally and/or numerically studied. Most of the scaling effects such as viscous dissipation and entrance effects were found to be insignificant. Nusselt number was found to reduce with the axial conduction number, signifying that conjugate heat transfer has a negative impact on the Nusselt number, which agrees with previous studies. From the CFD simulation, it was observed that only three walls were transferring heat; the walls of heat transfer had a uniform peripheral temperature while the heat flux varied peripherally. The closest simplified thermal boundary condition to these channels is the H1 with three (3) walls transferring heat. The entry and exit of the channel can however vary significantly due to thermal axial conduction and the effects of the manifolds.

In the heated sandwich test rig, thermal contact resistance between the top slab and micro-channel plate resulted in a significant thermal gradient at this interface which yielded lower calculated Nusselt numbers. Temperature measurements were corrected and the corrected Nusselt numbers increased linearly with Peclet numbers. This can be attributed to the effect of axial conduction (the axial conduction number is a function of the inverse of Peclet number). The axial thermal conduction yielded a variation of the heat flux density axially, despite having a uniform heat flux on the plate.

The velocity profile and hydraulic entry length agreed reasonably well with published numerical studies for rectangular channels however, it is recommended that when possible, numerical simulations with appropriate boundary conditions

should be undertaken to accurately understand the heat transfer processes. The results are beneficial for the design and operation of micro-channel absorber plates.

9. Conclusion and Recommendations

9.1 Conclusion

This thesis presented research focused on investigating heat transfer and fluid flow performance of micro-channel plates. These micro-channel plates are to be used as absorbers in a proposed design of compact flat plate collectors. The peculiarities of micro-channel heat transfer in solar collectors include low Reynolds number flows and low heat flux densities, compared with designs/devices being used in electronic cooling. The objectives of the research were

- To compare performance of this design to predictions of conventional theory.
- To study the significance of the various scaling effects on the absorber plate performance.
- To study the effects of channel design on performance.
- To propose optimal channel design and corresponding operating condition for this system.
- To propose accurate methods of predicting collector performance.

All these objectives were achieved and the main conclusions are outlined below.

Analytical investigation showed that, under similar conditions, the proposed design yields a much higher fin efficiency, F and collector efficiency factor, F' compared with the conventional solar collector design. The limit of significance of plate – fluid heat transfer coefficient on overall performance was observed to be 300 W/m^2.°C. The analytical model showed that axial thermal conduction can significantly alter the temperature profile of the absorber plate and therefore a few point temperature measurements may be inadequate to characterise the thermal profile. The collector flow factor, F'' and the heat removal factor, F_R can be improved by increasing the

thermal flow capacitance in the collector; this can be achieved by increasing the mass flow rate per collector area, $\dot{m}/A_c$, as well as reducing the overall heat loss, U_L. The overall heat loss of this collector design is expected to be much lower than conventional design because the absorber plate will be placed in a vacuum envelope.

A review of the literature on heat transfer and fluid flow in micro-channels, revealed that considerable discrepancies between results can be attributed to scaling effects. The effects of various scaling effects were therefore investigated experimentally and numerically. Most of the scaling effects, such as viscous dissipation and entrance effects were found to be insignificant. However, conjugate heat transfer, surface boundary condition, surface finish and measurement uncertainties were observed to be significant.

Conjugate heat transfer was observed to have a negative impact on the Nusselt number, which is in agreement with previous studies on micro-channel heat transfer. The axial thermal conduction yielded a variation of the heat flux density axially, despite having a uniform heat flux on the plate. Conjugate heat transfer resulted in a linear increase of Nusselt numbers with Peclet numbers. The effect of conjugate heat transfer can be suppressed by increasing the channel length, reducing the peripheral wall thickness and/or increasing the flow rate of the heat transfer fluid.

It was also observed that only three walls were transferring heat; the walls of heat transfer had a uniform peripheral temperature while the heat flux varied peripherally. The closest simplified thermal boundary condition to represent the heat transfer in these channels is the H1 with three (3) walls transferring heat. Therefore, theoretical predictions for this design should use this boundary condition.

The surface roughness on the channel walls was observed to differ depending on the method of fabrication. In this study, the etched channels were found to have rougher surfaces compared with the machined channels. The heat transfer and fluid flow performance of the etched channels were observed to be poorer than the machined ones. This indicates that milling out channels should be the preferred method for manufacturing these channels since the length scale of the hydraulic diameter is at the upper end of the microscale.

The experimental study was accompanied by several challenges; this highlighted the need for carefully designed experiments in micro-channel study. For example, it was observed that thermal contact resistance could result in an error of up to 50% in calculated Nusselt numbers. Therefore, using thermocouples or RTD's for measuring metal surface temperature should be adequately investigated and corrected as required. Alternatively, other methods of temperature measurements such as liquid crystal thermography, infrared camera or custom built temperature sensors embedded in the material could be employed. Also, experimental test rigs in the form of micro-channel heat exchangers can be designed for more accurate average heat transfer coefficient measurements. This is because it is much easier to get accurate measurements of the flow rate and fluid inlet and outlet temperatures. This method eliminates the uncertainty resulting from thermal contact resistance in measuring metal surface temperatures but cognisance must be taken of the modified thermal boundary condition.

A CFD Study, using the design and operating parameters of the experimental test rig produced comparable results to the experimental results. This numerical simulation also gave further insight into the heat transfer and fluid flow patterns in the micro-

channel plate. It is recommended that when possible, numerical simulations with appropriate boundary conditions should be undertaken to accurately understand the heat transfer and fluid flow processes. This will also help in designing experimental test rigs as various points of interest will be highlighted.

The significance of channel design on the overall performance was investigated experimentally and numerically. Conventional correlations for rectangular channels were found to over-predict the thermal performance of the plates. A strong dependence of heat transfer coefficient on fluid velocity was seen. A similar heat transfer coefficient at a given fluid velocity was observed for the range of hydraulic diameters studied, therefore channels with hydraulic diameters up to 1.5 mm can be used.

Nusselt number was dependent on Reynolds number, a trend which is conventional for flat plate or turbulent flows but not laminar flow in ducts; this trend has been attributed to conjugate heat transfer. The Nusselt number was observed to increase as aspect ratio approached unity. Experimentally measured friction factors were similar in trend to published data although slightly lower than predicted values based on numerical Poiseuille numbers for rectangular channels. The heat transfer coefficient increased with pump power; this improvement becomes marginal above a pump power of 0.3 W/m^2. More power might however need to be expended beyond this level to minimise the overall fluid temperature rise.

In practice, optimum micro-channel geometry in plates will need to be sized based on fluid properties and operating conditions. The micro-channels should also have thin walls to minimise the effects of conjugate heat transfer. A sustainable energy technology should be installed alongside to provide pumping power required to

minimise the overall fluid temperature rise. The results are beneficial for the design and operation of micro-channel absorber plates.

9.2 Recommendations

I. In the design and operation of micro-channel absorber plates, adequate measures must be taken to minimise the effects of conjugate heat transfer.

II. Ideally, the collector should me made of materials with thermal conductivities greater than 100W/m°C and the fin length between channels should be less than 10mm.

III. Channels should be designed to have hydraulic diameters between 0.3 mm and 2 mm. preferably; channels should have an aspect ratio close to unity.

IV. During operation, the heat transfer coefficient should be at least 300 W/m^2 °C. This will depend on the fluid velocity and type of fluid. An approximation that can be used in estimating the heat transfer coefficient is

$$h = 2.50\frac{\dot{m}c_p}{(a+b)k_f}.$$

V. Experiments should be carefully designed to eliminate uncertainty in temperature measurements.

VI. Appropriate correlations for the physical boundary conditions should be used when predicting the performance.

VII. An accurate 3D numerical simulation will be a better alternative for predicting the performance of micro-channels.

VIII. Further experimental tests should be done to determine overall heat loss coefficient by integrating the micro-channel plate in a vacuum envelope.

References

ADAMS, T. M., ABDEL-KHALIK, S. I., JETER, S. M. & QURESHI, Z. H. 1998. An experimental investigation of single-phase forced convection in microchannels. *International Journal of Heat and Mass Transfer,* 41**,** 851-857.

ALVAREZ, A., CABEZA, O., MUÑIZ, M. C. & VARELA, L. M. 2010. Experimental and numerical investigation of a flat-plate solar collector. *Energy,* 35**,** 3707-3716.

ANSYS, C. 2010a. Release 13.0. *ANSYS CFX-Solver Modeling Guide.*

ANSYS, C. 2010b. Release 13.0. *ANSYS CFX-Solver Theory Guide, ANSYS.*

ANSYS, I. 2010c. Release 13.0. *ANSYS Meshing User's Guide.*

ANSYS, I. 2014. *ANSYS CFX Product Overview* [Online]. Available: http://www.ansys.com/Products/Simulation+Technology/Fluid+Dynamics/Fluid+Dynamics+Products/ANSYS+CFX.

ASADI, M., XIE, G. & SUNDEN, B. 2014. A review of heat transfer and pressure drop characteristics of single and two-phase microchannels. *International Journal of Heat and Mass Transfer,* 79**,** 34-53.

AST, U. 2014. *Overview of Sensor Types* [Online]. Applied Sensor Technologies. Available: http://www.appliedsensortech.com/pdf/sensor_overview.pdf.

AZAD, E. 2012. Assessment of three types of heat pipe solar collectors. *Renewable and Sustainable Energy Reviews,* 16**,** 2833-2838.

BADESCU, V. 2006. Optimum fin geometry in flat plate solar collector systems. *Energy Conversion and Management,* 47**,** 2397-2413.

BAJURA, R. 1971. A model for flow distribution in manifolds. *Journal of Engineering for Gas Turbines and Power,* 93**,** 7-12.

BALAJ, M., ROOHI, E., AKHLAGHI, H. & MYONG, R. S. 2014. Investigation of convective heat transfer through constant wall heat flux micro/nano channels using DSMC. *International Journal of Heat and Mass Transfer,* 71**,** 633-638.

BAROZZI, G. & PAGLIARINI, G. 1985. A method to solve conjugate heat transfer problems: the case of fully developed laminar flow in a pipe. *Journal of heat transfer,* 107**,** 77-83.

BAROZZI, G. S. & PAGLIARINI, G. 1984. Experimental investigation of coupled conduction and laminar convection in a circular tube. *International journal of heat and mass transfer,* 27**,** 2321-2329.

BARSHILIA, H. C., JOHN, S. & MAHAJAN, V. 2012. Nanometric multi-scale rough, transparent and anti-reflective ZnO superhydrophobic coatings on high temperature solar absorber surfaces. *Solar Energy Materials and Solar Cells,* 107**,** 219-224.

BEIKIRCHER, T., BENZ, N. & SPIRKL, W. 1995. Gas heat conduction in evacuated flat-plate solar collectors: analysis and reduction. *Journal of Solar Energy Engineering, Transactions of the ASME,* 117**,** 229-235.

BELLO, M. B. & SAMBO, A. S. 1992. Simulation studies on pipe spacings for a collector and tank sizes for a solar water heater. *Energy Conversion and Management,* 33**,** 215-223.

BENZ, N. & BEIKIRCHER, T. 1999. HIGH EFFICIENCY EVACUATED FLAT-PLATE SOLAR COLLECTOR FOR PROCESS STEAM PRODUCTION. *Solar Energy,* 65**,** 111-118.

BETZ, A. R. & ATTINGER, D. 2010. Can segmented flow enhance heat transfer in microchannel heat sinks? *International Journal of Heat and Mass Transfer,* 53**,** 3683-3691.

BUCCI, A., CELATA, G. P., CUMO, M., SERRA, E. & ZUMMO, G. Water single-phase fluid flow and heat transfer in capillary tubes. ASME 2003 1st International Conference on Microchannels and Minichannels, 2003. American Society of Mechanical Engineers, 319-326.

BUDYNAS, R. G. N. J. K. S. J. E. 2011. *Shigley's Mechanical engineering design,* Singapore, McGraw-Hill.

CABUK, H. & MODI, V. 1989. On the design of optimum flow headers for heat exchangers. *American Society of Mechanical Engineers, Heat Transfer Division, HTD Published by ASME, New York, NY,* 108**,** 161-167.

CELATA, G., CUMO, M., MARCONI, V., MCPHAIL, S. & ZUMMO, G. 2006. Microtube liquid single-phase heat transfer in laminar flow. *International Journal of Heat and Mass Transfer,* 49**,** 3538-3546.

CELATA, G. P. 2004. Heat transfer and fluid flow in microchannels. *Boiling and evaporation*.

CELATA, G. P., CUMO, M., GUGLIELMI, M. & ZUMMO, G. 2002. Experimental investigation of hydraulic and single-phase heat transfer in 0.130-mm capillary tube. *Microscale Thermophysical Engineering,* 6**,** 85-97.

ÇENGEL, Y. A., GHAJAR, A. J. & KANOGLU, M. 2011. *Heat and mass transfer fundamentals and applications,* New York, McGraw Hill Higher Education.

ÇENGEL, Y. A. C. J. M. 2010. *Fluid mechanics : fundamentals and applications,* Boston, Mass. [u.a.], McGraw-Hill.

CHAI, L., XIA, G., ZHOU, M., LI, J. & QI, J. 2013. Optimum thermal design of interrupted microchannel heat sink with rectangular ribs in the transverse microchambers. *Applied Thermal Engineering,* 51**,** 880-889.

CHAURASIA, P. B. L. 2000. Solar water heaters based on concrete collectors. *Energy,* 25**,** 703-716.

CHEN, C.-H. 2006. Slip-flow heat transfer in a microchannel with viscous dissipation. *Heat and mass transfer,* 42**,** 853-860.

CHEN, C.-H. 2007. Forced convection heat transfer in microchannel heat sinks. *International Journal of Heat and Mass Transfer,* 50**,** 2182-2189.

CHEN, C.-H., LI, S.-Y., CHIANG, A. S. T., WU, A. T. & SUN, Y. S. 2011. Scratch-resistant zeolite anti-reflective coating on glass for solar applications. *Solar Energy Materials and Solar Cells,* 95**,** 1694-1700.

CHIU, H.-C., JANG, J.-H., YEH, H.-W. & WU, M.-S. 2011. The heat transfer characteristics of liquid cooling heatsink containing microchannels. *International Journal of Heat and Mass Transfer,* 54**,** 34-42.

CHO, E. S., CHOI, J. W., YOON, J. S. & KIM, M. S. 2010. Experimental study on microchannel heat sinks considering mass flow distribution with non-uniform heat flux conditions. *International Journal of Heat and Mass Transfer,* 53**,** 2159-2168.

CHOI, M. & CHO, K. 2001. Effect of the aspect ratio of rectangular channels on the heat transfer and hydrodynamics of paraffin slurry flow. *International Journal of Heat and Mass Transfer,* 44**,** 55-61.

CHOI, S. B., BARREN , R. R. & WARRINGTON, R. Q. 1991. Fluid flow and heat transfer in micro-tubes. *ASME DSC* 89-93.

CHUN, W., KO, Y. J., LEE, H. J., HAN, H., KIM, J. T. & CHEN, K. 2009. Effects of working fluids on the performance of a bi-directional thermodiode for solar energy utilization in buildings. *Solar Energy,* 83**,** 409-419.

CORREA, F., GONZÁLEZ, M., SERVÍN, H., MÁRQUEZ, F., RUTIAGA, J. G., LEMUS, A. A., REGUERA, E. & ALONSO, V. 2014. Development of a Selective

Low Cost Absorbing Surface based on Soot for Solar Thermal Applications. *Energy Procedia,* 57**,** 1565-1572.

CROCE, G. & D'AGARO, P. 2005. Numerical simulation of roughness effect on microchannel heat transfer and pressure drop in laminar flow. *Journal of Physics D: Applied Physics,* 38**,** 1518.

CROCE, G. & D'AGARO, P. 2004. Numerical analysis of roughness effect on microtube heat transfer. *Superlattices and Microstructures,* 35**,** 601-616.

DAVOINE, F., GALIONE, P. A., RAMOS-BARRADO, J. R., LEINEN, D., MARTÍN, F., DALCHIELE, E. A. & MAROTTI, R. E. 2013. Modeling of gradient index solar selective surfaces for solar thermal applications. *Solar Energy,* 91**,** 316-326.

DEL COL, D., PADOVAN, A., BORTOLATO, M., DAI PRÈ, M. & ZAMBOLIN, E. 2013. Thermal performance of flat plate solar collectors with sheet-and-tube and roll-bond absorbers. *Energy,* 58**,** 258-269.

DENG, Y., ZHAO, Y., WANG, W., QUAN, Z., WANG, L. & YU, D. 2013. Experimental investigation of performance for the novel flat plate solar collector with micro-channel heat pipe array (MHPA-FPC). *Applied Thermal Engineering,* 54**,** 440-449.

DHARAIYA, V. V. & KANDLIKAR, S. G. 2011. Numerical Investigation of Heat Transfer in Rectangular Microchannels Under H2 Boundary Condition During Developing and Fully Developed Laminar Flow. *Journal of Heat Transfer,* 134**,** 020911-020911.

DIRKER, J., MEYER, J. P. & GARACH, D. V. 2014. Inlet flow effects in micro-channels in the laminar and transitional regimes on single-phase heat transfer

coefficients and friction factors. *International Journal of Heat and Mass Transfer,* 77**,** 612-626.

DIXIT, T. & GHOSH, I. 2013. Low Reynolds number thermo-hydraulic characterization of offset and diamond minichannel metal heat sinks. *Experimental Thermal and Fluid Science,* 51**,** 227-238.

DIXIT, T. & GHOSH, I. 2015. Review of micro- and mini-channel heat sinks and heat exchangers for single phase fluids. *Renewable and Sustainable Energy Reviews,* 41**,** 1298-1311.

DOGRUOZ, M. B., ARIK, M. & PAUTSCH, A. Heat transfer in microchannels: substrate effects and cooling efficiency for rectangular and circular ducts. Thermal and Thermomechanical Phenomena in Electronic Systems (ITherm), 2010 12th IEEE Intersociety Conference on, 2-5 June 2010 2010. 1-7.

DOVIĆ, D. & ANDRASSY, M. 2012. Numerically assisted analysis of flat and corrugated plate solar collectors thermal performances. *Solar Energy,* 86**,** 2416-2431.

DOWSON, M., PEGG, I., HARRISON, D. & DEHOUCHE, Z. 2012. Predicted and in situ performance of a solar air collector incorporating a translucent granular aerogel cover. *Energy and Buildings,* 49**,** 173-187.

DUFFIE, J. A. & BECKMAN, W. A. 2006. *Solar engineering of thermal processes,* Hoboken, N.J., Wiley.

EATON, C. B. & BLUM, H. A. 1975. The use of moderate vacuum environments as a means of increasing the collection efficiencies and operating temperatures of flat-plate solar collectors. *Solar Energy,* 17**,** 151-158.

EICKER, U. 2003. Solar technologies for buildings. Chichester; Hoboken, NJ: Wiley.

ESCHER, W., BRUNSCHWILER, T., SHALKEVICH, N., SHALKEVICH, A., BURGI, T., MICHEL, B. & POULIKAKOS, D. 2011. On the cooling of electronics with nanofluids. *Journal of heat transfer,* 133**,** 051401.

FAGHRI, M. & SPARROW, E. 1980. Simultaneous wall and fluid axial conduction in laminar pipe-flow heat transfer. *Journal of Heat Transfer,* 102**,** 58-63.

FARAHAT, S., SARHADDI, F. & AJAM, H. 2009. Exergetic optimization of flat plate solar collectors. *Renewable Energy,* 34**,** 1169-1174.

FEDOROV, A. G. & VISKANTA, R. 2000. Three-dimensional conjugate heat transfer in the microchannel heat sink for electronic packaging. *International Journal of Heat and Mass Transfer,* 43**,** 399-415.

FRANK, T., LIFANTE, C., PRASSER, H.-M. & MENTER, F. 2010. Simulation of turbulent and thermal mixing in T-junctions using URANS and scale-resolving turbulence models in ANSYS CFX. *Nuclear Engineering and Design,* 240**,** 2313-2328.

GAMRAT, G., FAVRE-MARINET, M. & ASENDRYCH, D. 2005. Conduction and entrance effects on laminar liquid flow and heat transfer in rectangular microchannels. *International Journal of Heat and Mass Transfer,* 48**,** 2943-2954.

GAO, P., LE PERSON, S. & FAVRE-MARINET, M. 2002. Scale effects on hydrodynamics and heat transfer in two-dimensional mini and microchannels. *International Journal of Thermal Sciences,* 41**,** 1017-1027.

GHAMARI, D. M. & WORTH, R. A. 1992. The effect of tube spacing on the cost-effectiveness of a flat-plate solar collector. *Renewable Energy,* 2**,** 603-606.

GUNNASEGARAN, P., MOHAMMED, H. A., SHUAIB, N. H. & SAIDUR, R. 2010. The effect of geometrical parameters on heat transfer characteristics of

microchannels heat sink with different shapes. *International Communications in Heat and Mass Transfer,* 37**,** 1078-1086.

GUO, Z.-Y. & LI, Z.-X. 2003. Size effect on microscale single-phase flow and heat transfer. *International Journal of Heat and Mass Transfer,* 46**,** 149-159.

HARLEY, J. C., HUANG, Y., BAU, H. H. & ZEMEL, J. N. 1995. Gas flow in micro-channels. *Journal of Fluid Mechanics,* 284**,** 257-274.

HARMS, T. M., KAZMIERCZAK, M. J. & GERNER, F. M. 1999. Developing convective heat transfer in deep rectangular microchannels. *International Journal of Heat and Fluid Flow,* 20**,** 149-157.

HEGAB, H. E., BARI, A. & AMEEL, T. 2002. FRICTION AND CONVECTION STUDIES OF R-134a IN MICROCHANNELS WITHIN THE TRANSITION AND TURBULENT FLOW REGIMES. *Experimental Heat Transfer,* 15**,** 245-259.

HERWIG, H. & MAHULIKAR, S. P. 2006. Variable property effects in single-phase incompressible flows through microchannels. *International journal of thermal sciences,* 45**,** 977-981.

HESTNES, A. G. 1999. Building Integration Of Solar Energy Systems. *Solar Energy,* 67**,** 181-187.

HETSRONI, G., GUREVICH, M., MOSYAK, A. & ROZENBLIT, R. 2004. Drag reduction and heat transfer of surfactants flowing in a capillary tube. *International Journal of Heat and Mass Transfer,* 47**,** 3797-3809.

HETSRONI, G., MOSYAK, A., POGREBNYAK, E. & YARIN, L. P. 2005a. Fluid flow in micro-channels. *International Journal of Heat and Mass Transfer,* 48**,** 1982-1998.

HETSRONI, G., MOSYAK, A., POGREBNYAK, E. & YARIN, L. P. 2005b. Heat transfer in micro-channels: Comparison of experiments with theory and numerical results. *International Journal of Heat and Mass Transfer,* 48**,** 5580-5601.

HO, C. J., CHEN, W.-C. & YAN, W.-M. 2014. Correlations of heat transfer effectiveness in a minichannel heat sink with water-based suspensions of Al2O3 nanoparticles and/or MEPCM particles. *International Journal of Heat and Mass Transfer,* 69**,** 293-299.

HO, C. J. & CHEN, W. C. 2013. An experimental study on thermal performance of Al2O3/water nanofluid in a minichannel heat sink. *Applied Thermal Engineering,* 50**,** 516-522.

HOLMAN, J. P. 2010. *Heat transfer,* Boston, [Mass.], McGraw Hill Higher Education.

HOLMAN, J. P. 2012. *Experimental methods for engineers,* Boston, McGraw-Hill/Connect Learn Succeed.

HUSAIN, A. & KIM, K.-Y. 2008. Optimization of a microchannel heat sink with temperature dependent fluid properties. *Applied Thermal Engineering,* 28**,** 1101-1107.

HUSSEIN, H. M. S., EL-GHETANY, H. H. & NADA, S. A. 2006. Performance of wickless heat pipe flat plate solar collectors having different pipes cross sections geometries and filling ratios. *Energy Conversion and Management,* 47**,** 1539-1549.

IJAM, A., SAIDUR, R. & GANESAN, P. 2012. Cooling of minichannel heat sink using nanofluids. *International Communications in Heat and Mass Transfer,* 39**,** 1188-1194.

JEONG, H.-E. & JEONG, J.-T. 2006. Extended Graetz problem including streamwise conduction and viscous dissipation in microchannel. *International Journal of Heat and Mass Transfer,* 49**,** 2151-2157.

JUANICÓ, L. 2008. A new design of roof-integrated water solar collector for domestic heating and cooling. *Solar Energy,* 82**,** 481-492.

JUDY, J., MAYNES, D. & WEBB, B. Liquid flow pressure drop in microtubes. International Conference on Heat Transfer and Transport Phenomena in Microscale, Banff, Canada, 2000. 149-154.

KALOGIROU, S. 2003. The potential of solar industrial process heat applications. *Applied Energy,* 76**,** 337-361.

KANDLIKAR, S. G. & GRANDE, W. J. 2003. Evolution of Microchannel Flow Passages--Thermohydraulic Performance and Fabrication Technology. *Heat Transfer Engineering,* 24**,** 3-17.

KHAMIS MANSOUR, M. 2013. Thermal analysis of novel minichannel-based solar flat-plate collector. *Energy,* 60**,** 333-343.

KIM, S., CHOI, E. & CHO, Y. I. 1995. The effect of header shapes on the flow distribution in a manifold for electronic packaging applications. *International communications in heat and mass transfer,* 22**,** 329-341.

KIM, S. J. 2004. Methods for Thermal Optimization of Microchannel Heat Sinks. *Heat Transfer Engineering,* 25**,** 37-49.

KIM, S. J. & KIM, D. 1999. Forced Convection in Microstructures for Electronic Equipment Cooling. *Journal of Heat Transfer,* 121**,** 639-645.

KOO, J. & KLEINSTREUER, C. 2004. Viscous dissipation effects in microtubes and microchannels. *International Journal of Heat and Mass Transfer,* 47**,** 3159-3169.

KOO, J. & KLEINSTREUER, C. 2005. Analysis of surface roughness effects on heat transfer in micro-conduits. *International Journal of Heat and Mass Transfer,* 48**,** 2625-2634.

KOŞAR, A. 2010. Effect of substrate thickness and material on heat transfer in microchannel heat sinks. *International Journal of Thermal Sciences,* 49**,** 635-642.

KOU, H.-S., LEE, J.-J. & CHEN, C.-W. 2008. Optimum thermal performance of microchannel heat sink by adjusting channel width and height. *International Communications in Heat and Mass Transfer,* 35**,** 577-582.

KROEKER, C., SOLIMAN, H. & ORMISTON, S. 2004. Three-dimensional thermal analysis of heat sinks with circular cooling micro-channels. *International Journal of Heat and Mass Transfer,* 47**,** 4733-4744.

KUMAR, A., SAINI, R. P. & SAINI, J. S. 2012. Heat and fluid flow characteristics of roughened solar air heater ducts – A review. *Renewable Energy,* 47**,** 77-94.

KUNDU, B. 2002. Performance analysis and optimization of absorber plates of different geometry for a flat-plate solar collector: a comparative study. *Applied Thermal Engineering,* 22**,** 999-1012.

LEE, P.-S. & GARIMELLA, S. V. 2006. Thermally developing flow and heat transfer in rectangular microchannels of different aspect ratios. *international journal of heat and mass transfer,* 49**,** 3060-3067.

LEE, P.-S., GARIMELLA, S. V. & LIU, D. 2005. Investigation of heat transfer in rectangular microchannels. *International Journal of Heat and Mass Transfer,* 48**,** 1688-1704.

LELEA, D. 2011. The performance evaluation of Al2O3/water nanofluid flow and heat transfer in microchannel heat sink. *International Journal of Heat and Mass Transfer,* 54**,** 3891-3899.

LELEA, D., NISHIO, S. & TAKANO, K. 2004. The experimental research on microtube heat transfer and fluid flow of distilled water. *International Journal of Heat and Mass Transfer,* 47**,** 2817-2830.

LI, J. & PETERSON, G. P. 2007. 3-Dimensional numerical optimization of silicon-based high performance parallel microchannel heat sink with liquid flow. *International Journal of Heat and Mass Transfer,* 50**,** 2895-2904.

MALA, M. & LI, D. 1999. Flow characteristics of water in microtubes. *International Journal of Heat and Fluid Flow,* 20**,** 142-148.

MALA, M. G., LI, D. & DALE, J. D. 1997. Heat transfer and fluid flow in microchannels. *International Journal of Heat and Mass Transfer,* 40**,** 3079-3088.

MARANZANA, G., PERRY, I. & MAILLET, D. 2004. Mini-and micro-channels: influence of axial conduction in the walls. *International Journal of Heat and Mass Transfer,* 47**,** 3993-4004.

MATHIOULAKIS, E. & BELESSIOTIS, V. 2002. A new heat-pipe type solar domestic hot water system. *Solar Energy,* 72**,** 13-20.

MATRAWY, K. K. & FARKAS, I. 1997. Comparison study for three types of solar collectors for water heating. *Energy Conversion and Management,* 38**,** 861-869.

MATUSKA, T. & SOUREK, B. 2006. Façade solar collectors. *Solar Energy,* 80**,** 1443-1452.

MCHALE, J. P. & GARIMELLA, S. V. 2010. Heat transfer in trapezoidal microchannels of various aspect ratios. *International Journal of Heat and Mass Transfer,* 53**,** 365-375.

MISSAGGIA, L., WALPOLE, J., LIAU, Z. & PHILLIPS, R. 1989. Microchannel heat sinks for two-dimensional high-power-density diode laser arrays. *Quantum Electronics, IEEE Journal of,* 25**,** 1988-1992.

MOHAMMED, H., GUNNASEGARAN, P. & SHUAIB, N. 2011. Numerical simulation of heat transfer enhancement in wavy microchannel heat sink. *International Communications in Heat and Mass Transfer,* 38**,** 63-68.

MOHARANA, M. K., AGARWAL, G. & KHANDEKAR, S. 2011. Axial conduction in single-phase simultaneously developing flow in a rectangular mini-channel array. *International Journal of Thermal Sciences,* 50**,** 1001-1012.

MOKRANI, O., BOUROUGA, B., CASTELAIN, C. & PEERHOSSAINI, H. 2009. Fluid flow and convective heat transfer in flat microchannels. *International Journal of Heat and Mass Transfer,* 52**,** 1337-1352.

MOODY, L. 1944. Friction factors for pipe flow. Trun.~. *ASME C&, 671,* 684.

MORINI, G. L. 2004. Single-phase convective heat transfer in microchannels: a review of experimental results. *International Journal of Thermal Sciences,* 43**,** 631-651.

MORINI, G. L. Viscous Dissipation as Scaling Effect for Liquid Flows in Microchannels (Keynote). ASME 3rd International Conference on Microchannels and Minichannels, 2005. American Society of Mechanical Engineers, 93-102.

MORINI, G. L. 2006. Scaling effects for liquid flows in microchannels. *Heat Transfer Engineering,* 27**,** 64-73.

MOSS, R. & SHIRE, S. 2015. Design and Performance of Evacuated Solar Collector Microchannel Plates. EuroSun 2014 Conference, 2014 Aix-les-Baines, France. International Solar Energy Society.

MUWANGA, R. & HASSAN, I. 2006. Local heat transfer measurements in microchannels using liquid crystal thermography: methodology development and validation. *Journal of heat transfer,* 128**,** 617-626.

NAPHON, P. & KHONSEUR, O. 2009. Study on the convective heat transfer and pressure drop in the micro-channel heat sink. *International Communications in Heat and Mass Transfer,* 36**,** 39-44.

NAPHON, P. & NAKHARINTR, L. 2013. Heat transfer of nanofluids in the mini-rectangular fin heat sinks. *International Communications in Heat and Mass Transfer,* 40**,** 25-31.

NG, E. & TAN, S. 2004. Computation of three-dimensional developing pressure-driven liquid flow in a microchannel with EDL effect. *Numerical Heat Transfer, Part A,* 45**,** 1013-1027.

NI. 2014. *NI SCXI Voltage and Thermocouple Input Modules Data Sheet* [Online]. National Instrument. Available: http://www.ni.com/datasheet/pdf/en/ds-206.

NIELSEN, K. H., ORZOL, D. K., KOYNOV, S., CARNEY, S., HULTSTEIN, E. & WONDRACZEK, L. 2014. Large area, low cost anti-reflective coating for solar glasses. *Solar Energy Materials and Solar Cells,* 128**,** 283-288.

NONINO, C., SAVINO, S., DEL GIUDICE, S. & MANSUTTI, L. 2009. Conjugate forced convection and heat conduction in circular microchannels. *International Journal of Heat and Fluid Flow,* 30**,** 823-830.

NORDGAARD, A. & BECKMAN, W. A. 1992. Modelling of flat-plate collectors based on monolithic silica aerogel. *Solar Energy,* 49**,** 387-402.

OBOT, N. 2002. Toward a Better Understanding of Friction and Heat/Mass Transfer in Microchannels--a Literature Review. *Microscale Thermophysical Engineering,* 6**,** 155-173.

ORDAZ-FLORES, A., GARCÍA-VALLADARES, O. & GÓMEZ, V. H. 2012. Findings to improve the performance of a two-phase flat plate solar system, using acetone and methanol as working fluids. *Solar Energy,* 86**,** 1089-1098.

OWHAIB, W. & PALM, B. 2004. Experimental investigation of single-phase convective heat transfer in circular microchannels. *Experimental Thermal and Fluid Science,* 28**,** 105-110.

PALM, B. 2001. Heat transfer in microchannels. *Microscale Thermophysical Engineering,* 5**,** 155-175.

PENG, X., PETERSON, G. & WANG, B. 1994. Heat transfer characteristics of water flowing through microchannels. *Experimental Heat Transfer An International Journal,* 7**,** 265-283.

PENG, X. F. & PETERSON, G. P. 1996. Convective heat transfer and flow friction for water flow in microchannel structures. *International Journal of Heat and Mass Transfer,* 39**,** 2599-2608.

PETERSON, R. B. 1999. Numerical modeling of conduction effects in microscale counterflow heat exchangers. *Microscale Thermophysical Engineering,* 3**,** 17-30.

QI, R., NG, D., CORMIER, B. R. & MANNAN, M. S. 2010. Numerical simulations of LNG vapor dispersion in Brayton Fire Training Field tests with ANSYS CFX. *Journal of Hazardous Materials,* 183**,** 51-61.

QU, W., MALA, G. M. & LI, D. 2000. Heat transfer for water flow in trapezoidal silicon microchannels. *International Journal of Heat and Mass Transfer,* 43**,** 3925-3936.

QU, W. & MUDAWAR, I. 2002. Experimental and numerical study of pressure drop and heat transfer in a single-phase micro-channel heat sink. *International Journal of Heat and Mass Transfer,* 45**,** 2549-2565.

RAHIMI, M. & MEHRYAR, R. 2012. Numerical study of axial heat conduction effects on the local Nusselt number at the entrance and ending regions of a circular microchannel. *International Journal of Thermal Sciences,* 59**,** 87-94.

RAHMAN, M. M. 2000. Measurements of heat transfer in microchannel heat sinks. *International Communications in Heat and Mass Transfer,* 27**,** 495-506.

RAVIGURURAJAN, T. S. & DROST, M. K. 1999. Single-phase Flow Thermal Performance Characteristics of a Parallel MicroChannel Heat Exchanger. *Journal of Enhanced Heat Transfer,* 6**,** 383-393.

RAYEGAN, R. & TAO, Y. X. 2011. A procedure to select working fluids for Solar Organic Rankine Cycles (ORCs). *Renewable Energy,* 36**,** 659-670.

REYNAUD, S., DEBRAY, F., FRANC, J.-P. & MAITRE, T. 2005. Hydrodynamics and heat transfer in two-dimensional minichannels. *International Journal of Heat and Mass Transfer,* 48**,** 3197-3211.

ROMMEL, M. & MOOCK, W. 1997. Collector efficiency factor F' for absorbers with rectangular fluid ducts contacting the entire surface. *Solar Energy,* 60**,** 199-207.

ROSA, P., KARAYIANNIS, T. & COLLINS, M. 2009. Single-phase heat transfer in microchannels: the importance of scaling effects. *Applied Thermal Engineering,* 29**,** 3447-3468.

RYU, J. H., CHOI, D. H. & KIM, S. J. 2002. Numerical optimization of the thermal performance of a microchannel heat sink. *International Journal of Heat and Mass Transfer,* 45**,** 2823-2827.

SAENEN, T. & BAELMANS, M. 2012. Numerical model of a two-phase microchannel heat sink electronics cooling system. *International Journal of Thermal Sciences,* 59**,** 214-223.

SAID, Z., SAIDUR, R., RAHIM, N. A. & ALIM, M. A. 2014. Analyses of exergy efficiency and pumping power for a conventional flat plate solar collector using SWCNTs based nanofluid. *Energy and Buildings,* 78**,** 1-9.

SCHUBERT, K., BRANDNER, J., FICHTNER, M., LINDER, G., SCHYGULLA, U. & WENKA, A. 2001. Microstructure devices for applications in thermal and chemical process engineering. *Microscale Thermophysical Engineering,* 5**,** 17-39.

SHAH, R. K. & LONDON, A. L. 1978. *Laminar flow forced convection in ducts : a source book for compact heat exchanger analytical data*, New York, Academic Press.

SHARIAH, A. M., ROUSAN, A., ROUSAN, K. K. & AHMAD, A. A. 1999. Effect of thermal conductivity of absorber plate on the performance of a solar water heater. *Applied Thermal Engineering,* 19**,** 733-741.

SHARMA, C. S., TIWARI, M. K., MICHEL, B. & POULIKAKOS, D. 2013. Thermofluidics and energetics of a manifold microchannel heat sink for electronics with recovered hot water as working fluid. *International Journal of Heat and Mass Transfer,* 58**,** 135-151.

SHARMA, N. & DIAZ, G. 2011. Performance model of a novel evacuated-tube solar collector based on minichannels. *Solar Energy,* 85**,** 881-890.

SHEN, S., XU, J., ZHOU, J. & CHEN, Y. 2006. Flow and heat transfer in microchannels with rough wall surface. *Energy Conversion and Management,* 47**,** 1311-1325.

SKLAVOUNOS, S. & RIGAS, F. 2004. Validation of turbulence models in heavy gas dispersion over obstacles. *Journal of Hazardous Materials*, 108**,** 9-20.

SOBHAN, C. B. & GARIMELLA, S. V. 2001. A comparative analysis of studies on heat transfer and fluid flow in microchannels. *Microscale Thermophysical Engineering*, 5**,** 293-311.

STROUD, K. A. & BOOTH, D. J. 2013. *Engineering mathematics*, Palgrave Macmillan.

SVENDSEN, S. 1992. Solar collector with monolithic silica aerogel. *Journal of Non-Crystalline Solids,* 145**,** 240-243.

TANAK, H., NAKATAKE, Y. & WATANABE, K. 2005. Parametric study on a vertical multiple-effect diffusion-typesolar still coupled with a heat-pipe solar collector. *Desalination,* 171**,** 243-255.

TCHANCHE, B. F., PAPADAKIS, G., LAMBRINOS, G. & FRANGOUDAKIS, A. 2009. Fluid selection for a low-temperature solar organic Rankine cycle. *Applied Thermal Engineering,* 29**,** 2468-2476.

THARAMANI, C. N. & MAYANNA, S. M. 2007. Low-cost black Cu–Ni alloy coatings for solar selective applications. *Solar Energy Materials and Solar Cells,* 91**,** 664-669.

TIRIS, Ç., TIRIS, M. & TÜRE, I. E. 1995. Effects of fin design on collector efficiency. *Energy,* 20**,** 1021-1026.

TISELJ, I., HETSRONI, G., MAVKO, B., MOSYAK, A., POGREBNYAK, E. & SEGAL, Z. 2004. Effect of axial conduction on the heat transfer in micro-channels. *International Journal of Heat and Mass Transfer,* 47**,** 2551-2565.

TOH, K. C., CHEN, X. Y. & CHAI, J. C. 2002. Numerical computation of fluid flow and heat transfer in microchannels. *International Journal of Heat and Mass Transfer,* 45**,** 5133-5141.

TOMPKINS, D., YOO, T., HRNJAK, P., NEWELL, T. & CHO, K. 2002. Flow distribution and pressure drop in micro-channel manifolds.

TRIPANAGNOSTOPOULOS, Y., SOULIOTIS, M. & NOUSIA, T. 2000. Solar collectors with colored absorbers. *Solar Energy,* 68**,** 343-356.

TSAI, T.-H. & CHEIN, R. 2007. Performance analysis of nanofluid-cooled microchannel heat sinks. *International Journal of Heat and Fluid Flow,* 28**,** 1013-1026.

TSO, C. P. & MAHULIKAR, S. P. 1998. The use of the Brinkman number for single phase forced convective heat transfer in microchannels. *International Journal of Heat and Mass Transfer,* 41**,** 1759-1769.

TUCKERMAN, D. B. 1984. *Heat-transfer microstructures for integrated circuits.* PhD, Stanford University.

TUCKERMAN, D. B. & PEASE, R. F. W. 1981. High-performance heat sinking for VLSI. *IEEE Electron Device Lett. IEEE Electron Device Letters,* 2**,** 126-129.

TUNC, G. & BAYAZITOGLU, Y. 2001. Heat transfer in microtubes with viscous dissipation. *International Journal of Heat and Mass Transfer,* 44**,** 2395-2403.

TUNC, G. & BAYAZITOGLU, Y. 2002. Heat transfer in rectangular microchannels. *International Journal of Heat and Mass Transfer,* 45**,** 765-773.

UNEP. 2014. *.:: United Nations Environment Programme (UNEP) - SBCI* [Online]. Available: http://www.unep.org/sbci/AboutSBCI/Background.asp.

VESTLUND, J., DALENBÄCK, J.-O. & RÖNNELID, M. 2012. Movement and mechanical stresses in sealed, flat plate solar collectors. *Solar Energy,* 86**,** 339-350.

VESTLUND, J., RÖNNELID, M. & DALENBÄCK, J.-O. 2009. Thermal performance of gas-filled flat plate solar collectors. *Solar Energy,* 83**,** 896-904.

WANG, G., HAO, L. & CHENG, P. 2009. An experimental and numerical study of forced convection in a microchannel with negligible axial heat conduction. *International Journal of Heat and Mass Transfer,* 52**,** 1070-1074.

WEISBERG, A., BAU, H. H. & ZEMEL, J. 1992. Analysis of microchannels for integrated cooling. *International Journal of Heat and Mass Transfer,* 35**,** 2465-2474.

WIBULSWAS, P. 1966. *Laminar-flow heat-transfer in non-circular ducts.* PhD, University of London.

WU, H. & CHENG, P. 2003. An experimental study of convective heat transfer in silicon microchannels with different surface conditions. *International Journal of Heat and Mass Transfer,* 46**,** 2547-2556.

WU, P. & LITTLE, W. A. 1984. Measurement of the heat transfer characteristics of gas flow in fine channel heat exchangers used for microminiature refrigerators. *Cryogenics,* 24**,** 415-420.

XIA, G., CHAI, L., WANG, H., ZHOU, M. & CUI, Z. 2011. Optimum thermal design of microchannel heat sink with triangular reentrant cavities. *Applied Thermal Engineering,* 31**,** 1208-1219.

XIE, X. L., LIU, Z. J., HE, Y. L. & TAO, W. Q. 2009. Numerical study of laminar heat transfer and pressure drop characteristics in a water-cooled minichannel heat sink. *Applied Thermal Engineering,* 29**,** 64-74.

XU, B., OOI, K., WONG, N., LIU, C. & CHOI, W. Liquid flow in microchannels. Proceedings of the 5th ASME/JSME Joint Thermal Engineering Conference, 1999. 1-7.

YEH, H. M., HO, C. D. & YEH, C. W. 2003. Effect of aspect ratio on the collector efficiency of sheet-and-tube solar water heaters with the consideration of hydraulic dissipated energy. *Renewable Energy,* 28**,** 1575-1586.

YOUSEFI, T., VEISY, F., SHOJAEIZADEH, E. & ZINADINI, S. 2012. An experimental investigation on the effect of MWCNT-H2O nanofluid on the efficiency of flat-plate solar collectors. *Experimental Thermal and Fluid Science,* 39**,** 207-212.

YU, D., WARRINGTON, R., BARRON, R. & AMEEL, T. An experimental and theoretical investigation of fluid flow and heat transfer in microtubes. ASME/JSME Thermal Engineering Conference, 1995. Pergamon, 523-530.

ZHAO, C. Y. & LU, T. J. 2002. Analysis of microchannel heat sinks for electronics cooling. *International Journal of Heat and Mass Transfer,* 45**,** 4857-4869.

ZHAO, X., WANG, Z. & TANG, Q. 2010. Theoretical investigation of the performance of a novel loop heat pipe solar water heating system for use in Beijing, China. *Applied Thermal Engineering,* 30**,** 2526-2536.

ZHUAN, R. & WANG, W. 2013. Boiling heat transfer characteristics in a microchannel array heat sink with low mass flow rate. *Applied Thermal Engineering,* 51**,** 65-74.